

This is to certify that the
dissertation entitled

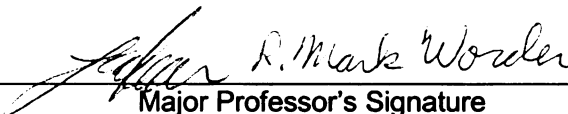
POLYELECTROLYTES BASED BIOMIMETIC INTERFACES FOR
BIOELECTRONIC APPLICATIONS

presented by

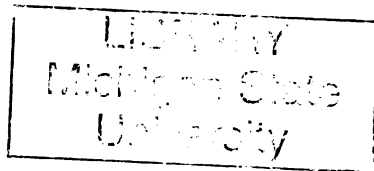
NEERAJ KOHLI

has been accepted towards fulfillment
of the requirements for the

PhD degree in Chemical Engineering


Major Professor's Signature

1/17/07
Date



PLACE IN RETURN BOX to remove this checkout from your record.
TO AVOID FINES return on or before date due.
MAY BE RECALLED with earlier due date if requested.

DATE DUE	DATE DUE	DATE DUE

**POLYELECTROLYTES BASED BIOMIMETIC INTERFACES FOR
BIOELECTRONIC APPLICATIONS**

By

Neeraj Kohli

A DISSERTATION

**Submitted to
Michigan State University
in partial fulfillment of the requirements
for the degree of**

DOCTOR OF PHILOSOPHY

Department of Chemical Engineering and Materials Science

2007

ABSTRACT

POLYELECTROLYTES BASED BIOMIMETIC INTERFACES FOR BIOELECTRONIC APPLICATIONS

By

Neeraj Kohli

Biomimetic interfaces consisting of polyelectrolyte multilayers, lipid bilayers, proteins and other nanostructured components have been fabricated and characterized in this study. While each chapter addresses a unique architecture or issue, the underlying theme of the study is the development of nanostructured biomimetic architectures that express protein activities and can be used to produce high-value devices and processes. Neuropathy target esterase (NTE) is a membrane protein found in human neurons. Binding of certain organophosphorus (OP) compounds to NTE is believed to cause OP-induced delayed neuropathy (OPIDN), a type of paralysis for which there is no effective treatment. Mutations in NTE have also been linked with serious neurological diseases, such as Lou Gehrig's disease. *In the first part* of this dissertation, a nanostructured biosensor to rapidly and sensitively measure the esterase activity of a fragment of NTE known as NEST is presented. The biosensor was fabricated by co-immobilizing two enzymes tyrosinase and NEST. The biosensor gives dose-dependent decrease in sensor output in response to known NEST (or NTE) inhibitors. *The second part* of this dissertation presents a theoretical model for bi-enzyme electrode biosensors that use substrate recycling to increase sensitivity. The model was validated using a rotating disk electrode on which tyrosinase and NEST were co-immobilized. The model's predictions were then used to quantify the effects of mass transport, partition coefficients, and

enzyme kinetics on the biosensor's metrological properties. This approach can be used to optimize the performance of bi-enzyme electrodes that involve substrate recycling. *The third part* of this study presents novel methods to produce arrays of bilayer lipid membranes (BLMs) on patterned polyelectrolyte multilayers. Liposomes composed of 1, 2-dioleoyl-sn-glycero-3-phosphocholine (DOPC) and 1, 2-dioleoyl-sn-glycero-3-phosphate (DOPA) were found to adsorb preferentially on poly(dimethyldiallylammonium chloride) (PDAC) and poly(allylamine hydrochloride) (PAH) surfaces, and in much smaller amounts onto sulfonated poly(styrene) (SPS) surfaces. Poly(ethylene glycol) (m-dPEG acid) coated surfaces were found to resist liposome adsorption. These results allowed the fabrication of BLM microarrays by exposing substrates patterned with PDAC, PAH and m-dPEG to DOPA/DOPC vesicles. *The fourth part* of this study presents a novel biomimetic interface consisting of an electrolessly deposited gold film overlaid with a tethered BLM (tBLM). Two model membrane biomolecules, the ionophore valinomycin and NEST, were incorporated into the tBLM, and the activity of the resulting biomimetic interfaces was measured. Microcontact printing (μ CP) of electrolessly deposited gold patterns on glass slides was also used to generate arrays of tBLMs. Such arrays may be useful for high-throughput screening of drugs and chemicals that interact with cell membranes. *The fifth part* of this study presents an approach to fabricate high-quality, 3D patterned bionanocomposite layered films on substrates whose surface properties are incompatible with existing self-assembly methods. *The last part* of this study presents an approach that can be used to create stable, nanostructured, amphiphilic and cross-linkable PAMAMOS-DMOMS dendrimer patterns.

Dedicated to my parents

ACKNOWLEDGEMENTS

I would like to thank my advisors, Dr. Ilsoon Lee and Dr. Mark Worden, for their invaluable mentorship, constant support and encouragement. It has been a pleasure working with them. I am also grateful to them for recruiting me and giving me the opportunity to advance my studies at Michigan State. I would also like to thank them for being patient with me while reviewing my Ph.D. thesis and encouraging me all along the way.

I would like to thank my committee members for agreeing to mentor me and for their advice and support during the course of my dissertation. I would like to thank Dr. Robert Ofoli for his inputs and for his careful critique of this dissertation, Dr. Merlin Bruening for his assistance, and for providing me with the generous use of his laboratory facilities.

During my years at MSU, I developed friendships that I will never forget and it remains one of the most valuable possessions that I carry forward. Ram, Vaibhav and Abhyuday are my earliest friends here, right from the Shaw Hall days and although everyone has gone their separate ways, we share the best of memories. I would like to thank the A-20 gang, Parmeet, Anish, Nimisha, Smita, Rajneesh, Monojit, Gayatri for being the best friends and roommates. I would also like to thank Devesh, Sachin Vaidya, Sachin Jadhav, Deep, Karuna and Lavanya for being great friends. I would especially like to thank Devesh and Sachin for all the good times that we had.

I have been most influenced in my life, by my parents and sister who have sacrificed a lot, and constantly encouraged me to seek higher goals and have never

doubted me. This dissertation would not have been possible if not for their love and support. Finally I would like to thank my girl friend Vandana for her support especially during the final years of this dissertation. She has always been there for me, especially at the worst times when the end seemed just as far away as the beginning. Her constant love and encouragement has been the beacon that has guided me to the end.

TABLE OF CONTENTS

1	INTRODUCTION	1
1.1	Overview	1
1.2	Nanostructured biosensor for neuropathy target esterase activity	4
1.3	Highly sensitive phenol sensor based on layer by layer assembly	5
1.4	Theoretical and experimental study of bi-enzyme electrodes with substrate recycling	6
1.5	Arrays of lipid bilayers and liposomes on polyelectrolyte multilayer templates	8
1.6	Tethered lipid bilayers on electrolessly deposited gold for bio-electronic applications	9
1.7	Intact transfer of layered bio-nanocomposite films on polyelectrolyte templates	11
2	NANOSTRUCTURED BIOSENSOR FOR MEASURING NEUROPATHY TARGET ESTERASE ACTIVITY	14
2.1	ABSTRACT	14
2.2	INTRODUCTION	15
2.3	EXPERIMENTAL SECTION	18
2.3.1	Materials	18
2.3.2	NEST expression and purification	18
2.3.3	Preparation of phenyl valerate solution	19
2.3.4	Preparation of gold electrode for NEST biosensor	19
2.3.5	Preparation of gold electrode for measuring the activity of AChE and BChE	21
2.3.6	Ellipsometry	21
2.3.7	Potential step amperometry and other measurements	21

2.4	RESULTS AND DISCUSSION	22
2.4.1	Ellipsometry	22
2.4.2	Amperometric response	23
2.4.2.1	<i>Dependence of current response on working potential and pH</i>	23
2.4.2.2	<i>Measurement of esterase activity using NEST biosensor</i>	23
2.4.3	<i>Amperometric response to catechol and phenol</i>	24
2.4.4	Inhibition of esterase activity	25
2.4.5	Storage stability	25
2.4.6	Immobilization of AChE and BChE	26
2.4.7	Significance of NEST biosensor	27
2.5	CONCLUSIONS.....	28
2.6	RECOMMENDATIONS FOR FUTURE WORK	28
3	HIGHLY SENSITIVE PHENOL SENSOR BASED ON LAYER-BY-LAYER ASSEMBLY	43
3.1	ABSTRACT.....	43
3.2	INTRODUCTION	44
3.3	EXPERIMENTAL SECTION	46
3.3.1	Preparation of poly-L-lysine (PLL), and tyrosinase (Tyr) multilayer assemblies	46
3.3.2	Ellipsometry.....	46
3.3.3	Reflectance Fourier transform infrared spectroscopy.....	47
3.3.4	Potential step amperometry.....	47
3.4	RESULTS AND DISCUSSIONS.....	47
3.4.1	Ellipsometry and FTIR	47
3.4.2	Dependence of current response on working potential and pH	48

3.4.3	Amperometric response to catechol and phenol	48
3.4.4	Effect of number of PLL-Tyr bilayers	49
3.4.5	Cyclic voltammetry.....	49
3.4.6	Discussions	50
3.5	CONCLUSIONS.....	51
3.6	RECOMMENDATIONS FOR FUTURE WORK	51
4	THEORETICAL AND EXPERIMENTAL STUDY OF BI-ENZYME ELECTRODES WITH SUBSTRATE RECYCLING.....	58
4.1	ABSTRACT.....	58
4.2	INTRODUCTION	58
4.3	EXPERIMENTAL SECTION.....	61
4.3.1	Materials	61
4.3.2	Preparation of gold electrode.....	61
4.3.3	Chronoamperometry and other measurements	62
4.4	THEORETICAL MODEL.....	62
4.4.1	Enzyme kinetics	62
4.4.2	Assumptions.....	64
4.4.3	Model equations.....	66
4.4.4	Boundary conditions	67
4.4.5	Validation of the model	73
4.4.6	Simulations and Discussions.....	75
4.5	CONCLUSIONS.....	78
5	ARRAYS OF LIPID BILAYERS AND LIPOSOMES ON PATTERNED POLYELECTROLYTE TEMPLATES.....	89

5.1	ABSTRACT.....	89
5.2	INTRODUCTION	90
5.3	EXPERIMENTAL SECTION	93
5.3.1	Materials	93
5.3.2	Preparation of stamps.....	94
5.3.3	Preparation of liposomes.....	94
5.3.4	Preparation of Polyelectrolyte Multilayers (PEMs).....	95
5.3.5	Preparation of arrays:.....	95
5.3.6	Total internal reflection microscopy:.....	96
5.3.7	Fluorescence recovery after pattern photobleaching (FRAPP):	98
5.3.8	Theory and Data Analyses for Fluorescence recovery after pattern photobleaching.....	99
5.3.9	Theory	100
5.3.10	Data Analysis and curve fitting.....	102
5.3.11	Microgravimetric experiments:.....	103
5.4	RESULTS AND DISCUSSIONS.....	103
5.4.1	Characterization of liposome adsorption by TIRFM.....	103
5.4.2	Formation of arrays of lipid bilayers	106
5.4.3	Assessment of liposome adsorption and rupture to form bilayers.....	107
5.4.4	Characterization of liposome adsorption and rupture by QCM.....	109
5.5	CONCLUSIONS.....	111
5.6	RECOMMENDATIONS FOR FUTURE WORK	112
6	TETHERED LIPID BILAYERS ON ELECTROLESSLY DEPOSITED GOLD FOR BIOELECTRONIC APPLICATIONS.....	126
6.1	ABSTRACT.....	126

6.2	INTRODUCTION	127
6.3	EXPERIMENTAL SECTION	129
6.3.1	Materials	129
6.3.2	Preparation of stamps.....	130
6.3.3	Synthesis of colloidal gold particles	130
6.3.4	Formation of gold film and patterns by electroless deposition.....	130
6.3.5	Preparation of liposomes for fluorescence and electrochemical measurements.....	131
6.3.6	Formation of tBLMs containing valinomycin	132
6.3.7	Formation of NEST-containing liposomes (NEST-DOPC liposomes) ..	132
6.3.8	Preparation of phenyl valerate micellar suspension.....	133
6.3.9	Formation and characterization of NEST-containing tBLMs.....	133
6.3.10	Arrays of lipid bilayers	134
6.3.11	Electrochemical impedance spectroscopy (EIS) measurements.....	134
6.3.12	Fluorescence recovery after pattern photobleaching (FRAPP)	135
6.3.13	Other measurements.....	135
6.4	RESULTS AND DISCUSSIONS.....	136
6.4.1	Formation of gold films	136
6.4.2	Functional tBLMs containing valinomycin	137
6.4.3	Functional BLM containing NEST protein.....	138
6.4.4	BLM fluidity measurement using FRAPP	139
6.4.5	Fabrication and characterization of gold patterns.....	139
6.4.6	Fabrication of tBLM arrays	140
6.4.7	Significance of results and potential applications.....	141
6.5	CONCLUSIONS.....	142
6.6	RECOMMENDATIONS FOR FUTURE WORK	143

7	INTACT TRANSFER OF LAYERED BIONANOCOMPOSITE ARRAYS	154
7.1	ABSTRACT.....	154
7.2	INTRODUCTION	154
7.3	EXPERIMENTAL SECTION	157
7.3.1	Materials	157
7.3.2	Preparation of polyelectrolyte multilayers (PEMs)	158
7.3.3	Fluorescent labeling of PAMAM dendrimers, sADH and sDH	158
7.3.4	Fabrication of 3-D structures or architectures	159
7.3.5	Other measurements.....	160
7.4	RESULTS AND DISCUSSIONS.....	160
7.5	CONCLUSIONS.....	165
8	NANOSTRUCTURED CROSS-LINKABLE MICROPATTERNS VIA AMPHIPHILIC DENDRIMER STAMPING.....	177
8.1	ABSTRACT.....	177
8.2	INTRODUCTION	178
8.3	EXPERIMENTAL SECTION	181
8.4	RESULTS AND DISCUSSIONS.....	183
8.5	CONCLUSIONS.....	188
9	REFERENCES	195

LIST OF FIGURES

- Figure 2.1: Molecular architecture of the NEST biosensor. 30
- Figure 2.2: Ellipsometric thicknesses after the successive addition of following layers: thioctic acid (point a), PLL-Tyr first bilayer (point b), PLL-Tyr second bilayer (point c), PLL-Tyr third bilayer (point d), and PLL and NEST final bilayer (point e). 31
- Figure 2.3: Effect of working potential on the response current of the enzyme electrode in 0.1 M phosphate buffer (pH 7.0) with (i) and without (ii) 12 μM phenyl valerate solution, in 0.1 M phosphate buffer at an applied potential of -0.1 V (vs Ag/AgCl). 32
- Figure 2.4: Effect of pH on the response current of the electrode, in the presence of 12 μM phenyl valerate solution, in 0.1 M phosphate buffer at an applied potential of -0.1 V (vs Ag/AgCl). 33
- Figure 2.5: (a) Current time response of the NEST biosensor to the addition of aliquots of 4 μM phenyl valerate, in 0.1 M phosphate buffer, pH 7.0, at an applied potential of -0.1 V (vs Ag/AgCl). (b) Calibration plot. 34
- Figure 2.6: Control experiment: Current time response on an electrode containing only tyrosinase. The electrode was assembled in exactly the same way as NEST biosensor, except that the final NEST layer was not deposited. 35
- Figure 2.7: (a) Current time response of the NEST biosensor to the addition of aliquots of 4 μM phenol in 0.1 M phosphate buffer, pH 7.0 at an applied potential of -0.1 V (vs Ag/AgCl). (b) Calibration plot. 36
- Figure 2.8: (a) Current time response of the NEST biosensor to the addition of aliquots of 8 μM catechol in 0.1 M phosphate buffer, pH 7.0 at an applied potential of -0.1 V (vs Ag/AgCl). (b) Calibration plot. 37
- Figure 2.9: Current time response of NEST biosensor to the addition of 8 μM phenyl valerate followed by the addition of 10 μM of NEST inhibitor PMSF, in 0.1 M phosphate buffer, pH 7.0. 38
- Figure 2.10: Current time response of NEST biosensor to the addition of 8 μM phenyl valerate followed by the addition of 100 μM of NEST inhibitor PMSF, in 0.1 M phosphate buffer, pH 7.0. 39
- Figure 2.11: Current time response of NEST biosensor to the addition of 8 μM phenyl valerate followed by the addition of 100 μM of NEST inhibitor PMSF, in 0.1 M phosphate buffer, pH 7.0. 40
- Figure 2.12: Current time response of a bi-enzyme electrode consisting of tyrosinase and AChE to the addition of aliquots of phenyl acetate to obtain final phenyl acetate

concentrations as increments of 8 μM , in 0.1 M phosphate buffer, pH 7.0, at an applied potential of -0.1 V (vs Ag/AgCl).....	41
Figure 3.1: Ellipsometric thickness and FTIR absorbances at 1665 cm^{-1} for PLL-Tyr multilayered films.	53
Figure 3.2: FTIR spectra of PLL-Tyr films composed of up to 6 bilayers.	54
Figure 3.3 (a) Current time response of the gold electrode containing 6 PLL-Tyr bilayers to the addition of aliquots of 8 μM catechol in 0.1 M phosphate buffer, pH 7.0 at an applied potential of -0.1 V (vs Ag/AgCl). (b) Calibration plot.	55
Figure 3.4: Effect of number of PLL-Tyr bilayers on the current sensitivity of the enzyme electrode to catechol.	56
Figure 3.5: (a) Cyclic voltammograms of the enzyme electrode containing 2 PLL-Tyr bilayers, in the presence of different concentrations of catechol: (i) 3.5 μM , (ii) 7 μM , and (iii) 10.5 μM . (b) Representative example of a calibration plot. All the measurements were performed in 0.1 M phosphate buffer, pH 7.0, and scan rate of 100 mVs^{-1}	57
Figure 4.1: Molecular architecture of bi-enzyme electrode.....	79
Figure 4.2: Schematic representation of a rotating disk bi-enzyme electrode and principle of its functioning in the presence of phenyl valerate substrate. S_1 , S_2 , S_3 and Q_4 denote the substrate phenyl valerate, phenol, catechol and <i>o</i> -quinone, respectively. E_1 denotes NEST esterase activity. E_2 and E_3 denote tyrosinase's phenolase and catecholase activity, respectively. L denotes the thickness of the enzyme.....	80
Figure 4.3: Reciprocal plots of S_{ct}^a and $\frac{S_{ct}^c}{S_{ct}^a}$ versus the square root of rotation rate for electrode A.....	81
Figure 4.4: Cathodic sensitivity, S_{ph}^c , in the presence of phenol as a function of rotation rate.....	82
Figure 4.5: Cathodic sensitivity, S_{pv}^c , in the presence of phenyl valerate as a function of rotation rate.....	83

Figure 4.6: Concentration profiles of (a) phenyl valerate (b) phenol, catechol and <i>o</i> -quinone normalized to phenyl valerate bulk concentration ($S_1(\infty)$) as a function of relative position (x/L) within the bi-enzyme interface.....	84
Figure 4.7: Concentration profile of <i>o</i> -quinone normalized to phenyl valerate bulk concentration ($S_1(\infty)$) at various rotation rates.....	85
Figure 4.8: Current sensitivity, S_{pv}^C , as a function of amount of NEST esterase activity (θ_1) and tyrosinase's catecholase activity (θ_3).....	86
Figure 4.9: Signal amplification in bi-enzyme electrode due to the recycling of catechol. For simulation, the following values of different parameters were used: $P_m = 0.0091\text{cm/s}$, $D_e = 2.2 \times 10^{-5} \text{ cm}^2/\text{s}$, $\omega = 500 \text{ rpm}$	87
Figure 5.1: Structure of (a) DOPC, (b) DOPA, (c) NBD-PC	114
Figure 5.2: Structures of (a) PDAC, (b) SPS, (c) PAH, and (d) m-dPEG acid.	115
Figure 5.3: Schematic representation of the process for the fabrication of arrays of BLMs on PDAC and PAH patterned substrates.	116
Figure 5.4: Schematic representation of the process for the fabrication of arrays of BLMs on m-dPEG acid patterned substrates.	117
Figure 5.5: Experimental set-up for fluorescence recovery after pattern photobleaching using EPI-illumination.	118
Figure 5.6: Adsorption curves of (A) liposomes (10% DOPA, 90% DOPC) on PDAC. (B) liposomes (10% DOPA, 90% DOPC) on SPS. (C) liposomes (20% DOPA, 80% DOPC) on PDAC. (D) liposomes (20% DOPA, 80% DOPC) on SPS.....	119
Figure 5.7: a) Adsorption of liposomes (10% DOPA, 90% DOPC) on a glass slide coated with PEMs with m-dPEG acid being the topmost layer. b) Buffer-wash experiments to study liposome desorption from PEMs. The top and bottom curves depict desorption of liposomes from PEMs with PDAC and m-dPEG as the top layer, respectively. At $t=0$, adsorption of liposomes (which have adsorbed for at least 45 min) is halted by introducing liposome-free buffer. In each curve, the fluorescence intensity has been normalized by the corresponding fluorescence value obtained prior to initiation of the buffer wash.	120
Figure 5.8: Fluorescence images showing (a) line patterns on a PDAC patterned substrate (b) circular patterns on a PDAC patterned substrate (c) line patterns on a PAH patterned substrate.	121

Figure 5.9: Fluorescence microscopy images showing (a) line patterns on m-dPEG acid patterned substrate (b) circular patterns on m-dPEG patterned substrate.....	122
Figure 5.10: Fluorescence recovery after pattern photobleaching (FRAPP) profiles on PEMs with (a) PDAC and (b) PAH as topmost layer. Only post bleach fluorescence intensity normalized against the corresponding pre bleach fluorescence value is shown. The solid lines in the figures represent fits to the recovery data set with models (Wright, Palmer et al. 1988) describing populations with a single mobile fraction and an immobile fraction. Plots of residuals vs. time are also indicated below each figure. Average values obtained with these models are summarized in Table 1	123
Figure 5.11: Changes in QCM resonant frequency (Curves i and iii) and dissipation (Curves ii and iv) versus time for the adsorption of liposomes on (a) PEMs having a top layer of PDAC (b) PEMs having a top layer of PAH.....	124
Figure 6.1: Structure of various lipid molecules: (a) DGP (reservoir lipid); (b) DPGP (mobile lipid); (c) NBD-PE.	144
Figure 6.2: Schematic representation of the process for the deposition of Au films: (a) plasma-treated glass slide; (b) slide after silanization with MPS; (c) modified slide after dipping in Au particle solution; (d) formation of conductive Au films after seeding step.....	145
Figure 6.3: Schematic representation of the process for the fabrication of Au patterns: (a) stamping of MPS on a glass slide; (b) MPS patterns on a glass slide; (c) MPS-patterned modified glass slide after heating; (d) MPS-patterned slide after dipping in Au colloid solution; (e) formation of Au patterns after seeding step.	146
Figure 6.4: FE-SEM images showing the growth of gold on glass slides: (a) after dipping in colloidal solution; (b) seeding once; (c) seeding twice; (d) seeding three times.	147
Figure 6.5: a) Representation of a tethered bilayer membrane containing an ionophore (valinomycin). (b) Electrochemical spectra in a 50 mM KCl / 50 mM NaCl aqueous solution of a tethered lipid bilayer (curve i), and a valinomycin-containing lipid bilayer (curve ii). (c) Equivalent circuit of a bilayer.	148
Figure 6.6: Fluorescence recovery after pattern photobleaching (FRAPP) profile of lipid bilayers on electrolessly deposited gold films. The dots represent post-bleach fluorescence intensity normalized against the corresponding pre-bleach fluorescence value. The solid line in the figure represents the fit of the recovery data.....	149
Figure 6.7: Optical microscopy images of gold: (a) circular patterns on a glass slide; (b) line patterns on a glass slide.....	150

- Figure 6.8: EDS image showing (a) X-rays collected from Region 1 of a SEM image; (b) X-rays collected from Region 2 of a SEM image. There is a peak corresponding to Au in X-rays collected from Region 1 but not in X-rays from Region 2, confirming the selective deposition of Au on the patterned surface. 151
- Figure 6.9: (a) Topographical AFM image of gold patterns; (b) 3-D image of the patterns; (c) pattern height on glass slide. All these images were obtained in air using tapping mode..... 152
- Figure 6.10: Fluorescence image showing line patterns of a lipid bilayer consisting of NBD-PE as the fluorophores. The image was obtained using a filter cube (Ex: 465-495/DM: 505/Em: 515-555). 153
- Figure 7.1: Schematic representation of the procedure used for printing: (a) stamp coated with sequential layers of proteins (sADH or sDH) and PEMs (PDAC/SPS bilayers) (Case 1); alternating layers of sADH and G4 PAMAM dendrimers on PEMs (case 2); and PDAC/SPS bilayer sandwiched between sADH layers (case 3). (b) Glass slide coated with PEMs (10.5 bilayers). (c) Patterned substrate..... 167
- Figure 7.2: (a) Two-dimensional AFM image of sADH patterns, on a PEM (10.5 PDAC/SPS bilayers) coated glass substrate. (b) Cross-sectional AFM image of sADH patterns, on a PEM (10.5 PDAC/SPS bilayers) coated glass substrate. 168
- Figure 7.3: Two-dimensional and cross-sectional AFM images: (a-b) when a (sADH)₁(PDAC/SPS)₂₀ multilayer film was transferred to a PEM (10.5 PDAC/SPS bilayers) coated glass substrate; (c-d) when a (sADH)₁(PDAC/SPS)₄₀ multilayer film was transferred to a PEM (10.5 PDAC/SPS bilayer) coated glass substrate. 169
- Figure 7.4: Fluorescence images of: (a) the circular patterns obtained on the transfer of a multilayer film consisting of a layer of fluorescently labeled sADH and 20 PDAC/SPS bilayers, on a PEM (10.5 PDAC/SPS bilayers) coated glass substrate; (b) the PDMS stamp surface after printing. 170
- Figure 7.5: Schematic representation of the process used for multilevel and multicomponent stamping..... 171
- Figure 7.6: (a) Red fluorescence from vertically printed (Alexa fluor labeled-sDH)₁(PDAC/SPS)₂₀ lines on a PEM (10.5 PDAC/SPS bilayers) coated glass substrate; (b) Green fluorescence from horizontally printed (FITC labeled-sADH)₁(PDAC/SPS)₂₀ lines, on a PEM (10.5 PDAC/SPS bilayers) coated glass substrate;(c) Digitally combined fluorescence image showing both red and green fluorescence 172
- Figure 7.7: (a) Fluorescence image of the patterned films of sADH, G4 PAMAM dendrimers and PEMs (30 PDAC/SPS bilayers) with fluorescently labeled sADH as the topmost layer, on a PEM (10.5 PDAC/SPS bilayers) coated glass substrate. (b) Fluorescence image of the line patterns of fluorescently labeled dendrimers

sandwiched between patterned sADH layer and PEMs (30 PDAC/SPS), on a PEM (10.5 PDAC/SPS bilayers) coated glass substrate.	173
Figure 7.8: (a-b) Two-dimensional and cross-sectional AFM images of a patterned film containing sequential layers of sADH, PAMAM dendrimers and PEMs (30 PDAC/SPS bilayers), with sADH as the topmost layer, on a PEM (10.5 PDAC/SPS bilayers) coated glass substrate. (c-d) Two-dimensional and cross-sectional AFM images of a patterned film containing sequential layers of sADH and PAMAM dendrimers with sADH as the topmost layer, on a PEM (10.5 PDAC/SPS bilayers) coated glass substrate.	174
Figure 7.9: (a-b) Fluorescence images of the patterned films of a PDAC/SPS bilayer sandwiched between FITC labeled sADH base layer and Alexa fluor labeled sADH topmost layer, on a PEM (10.5 PDAC/SPS bilayers) coated glass substrate, (a) Green fluorescence emanating from FITC labeled sADH base layer, obtained using the following filter set, Ex: 465-495/DM: 505/Em: 515-555; (b) Red fluorescence emanating from Alexa fluor labeled sADH topmost layer, obtained using the following filter set, Ex: 510-560/DM: 565/Em: 590-690. (c) Cross-sectional topographical image of a patterned film containing sequential layers of sADH and 1 PDAC/SPS bilayer, on a PEM (10.5 PDAC/SPS bilayers) coated glass substrate. (d) Topographical AFM image of a patterned film consisting of a PDAC/SPS bilayer sandwiched between two sADH layers, on a PEM (10.5 PDAC/SPS bilayers) coated glass substrate.	175
Figure 7.10: Arrays of amphiphilic proteins obtained on patterned substrate using directed self-assembly.....	176
Figure 8.1: Schematic representation of PAMAMOS-DMOMS dendrimer.....	185
Figure 8.2: (a) An example of an AFM image showing unstable circular patterns on a glass slide obtained from a 0.5% PAMAMOS dendrimer solution. (b-d) Visualization of PAMAMOS dendrimer patterns on various substrates. (b) Optical micrograph of the circular patterns on a glass substrate (c) Fluorescence image of the circular pattern on a glass substrate; (d) Fluorescence image of the line pattern on a SPS surface.....	186
Figure 8.3: AFM images of cross-linked PAMAMOS dendrimer patterns. (a) Patterned glass substrate stamped by 1wt.-% dendrimer solution in methanol for a contact time of 5 min; (b) Patterned silicon wafer stamped by a 1wt.-% dendrimer solution in methanol for a contact time of 25 min; (c) Pattern height on glass substrate; (d) Pattern height on silicon wafer; (e) 3-D image of the patterned glass substrate; (f) 3-D image of the patterned silicon wafer.....	187
Figure 8.4: Crosslinking of PAMAMOS-DMOMS dendrimers into a covalently bonded network structure.....	188

Figure 8.5: Covalent bonding of PAMAMOS-DMOMS dendrimers to glass surfaces having silanol surface groups.....189

LIST OF TABLES

Table 2-1: Performance of bi-enzyme electrodes containing tyrosinase and different esterases. Phenyl valerate gave the highest current sensitivity for bi-enzyme electrodes containing tyrosinase and NEST, and also for bi-enzyme electrodes containing tyrosinase and BChE. Phenyl acetate gave the highest sensitivity for bi-enzyme electrodes containing tyrosinase and AChE.....	42
Table 4.1: Kinetic characteristics of tyrosinase immobilized in bi-enzyme electrode. Values of k and K were obtained from the literature (Coche-Guerente, Labbe et al. 2001). However, enzyme concentration was calculated using Equations 4.40 and 4.41.....	85
Table 5-1: Average lipid diffusion coefficients (D), and average mobile fractions (m) for BLMs formed on PEMs with PDAC and PAH as the topmost layer. The estimates were obtained by averaging parameters fit from all recovery curves.....	125
Table 8-1: Effects of concentration and contact time on the stability and uniformity of patterns on different substrates.....	194

NOMENCLATURE

C_{dl}	Double layer capacitance
D_e	Diffusion coefficient of catechol, phenol or phenyl valerate in bulk solution
D_f	Diffusion coefficient of catechol, phenol or phenyl valerate inside the enzyme layer
E_1	Concentration of active sites of NEST inside the bi-enzyme electrode
E_2	Concentration of mono-phenolase active sites inside the bi-enzyme electrode
E_3	Concentration of mono-phenolase active sites inside the bi-enzyme electrode
F	Faraday constant
n	Number of electrons transferred
J	Current density
k_p	Partition coefficient
k_{cat}	Catalytic turnover number
K_m	Michaelis-menten constant
m_e	Rate of mass transfer in the bulk
P_m	Permeability inside the enzyme layer
θ_i	Dimensionless parameter that compares the enzymatic rate of species i with its diffusion inside the bi-enzyme layer

R_{ct}	Charge transfer resistance
R_s	Resistance of solution
S_1	Phenyl valerate concentration inside the enzyme layer
S_2	Phenol concentration inside the enzyme layer
S_3	Catechol concentration inside the enzyme layer
Q_4	Quinone concentration inside the enzyme layer
λ_1	Reaction length related to phenyl valerate
λ_2	Reaction length related to phenol
λ_3	Reaction length related to catechol
Z_w	Warburg-diffusion impedance

ABBREVIATIONS

AFM	Atomic force microscopy
AChE	Acetylcholinesterase
ALS	Amyotrophic lateral sclerosis
BChE	Butyrylcholinesterase
BLM	Bilayer lipid membrane
CHAPS	[(3-cholamidopropyl) dimethylammonio]-1-propanesulfonate

CVD	Chemical vapor deposition
DGP	1,2-dipalmitoyl- <i>sn</i> -glycero-3-phosphoethanolamine- <i>N</i> -[3-(2-pyridyldithio)propionate
DPGP	1,2-di- <i>O</i> -phytanyl- <i>sn</i> -glycero-3-phosphoethanolamine
DOPA	1,2-dioleoyl- <i>sn</i> -Glycero-3-Phosphate (Monosodium Salt)
DOPC	1,2-dioleoyl- <i>sn</i> -Glycero-3-Phosphocholine
DTT	Dithiothreitol
EIS	Electrochemical impedance spectroscopy
EDS	Energy dispersive spectroscopy
EDTA	Ethylenediaminetetraacetic acid
FITC	Fluorescein isothiocyanate
FRAP	Fluorescence recovery after photobleaching
FRAPP	Fluorescence recovery after pattern photobleaching
FRET	Fluorescence resonance energy transfer
FTIR	Fourier transform infrared spectroscopy
HEPES	4-(2-hydroxyethyl)piperazine-1-ethanesulfonic acid
ITP	Intact transfer printing
LBL	Layer by layer assembly
μ CP	Microcontact printing
MPS	3-mercaptopropyltrimethoxy silane

NBD PC 1-palmitoyl-2-[6-[(7-nitro-2-1,3-benzoxadiazol-4-yl)amino]hexanoyl]-*sn*-glycero-3-phosphocholine

NTE Neuropathy target esterase

OP Organophosphorus

OPIDN Organophosphorus compounds induced delayed neuropathy

PEG Polyethylene glycol

PEO Polyethylene oxide

PEM Polyelectrolyte multilayer

PMSF Phenylmethylsulfonyl fluoride

PAH Poly(allylamine hydrochloride)

PDAC Poly(diallyldimethyl ammonium chloride)

PDMS Poly(dimethylsiloxane)

PLL Poly-L-lysine

PMT Photomultiplier tube

POPS Polymer-on-polymer stamping

PVD Physical vapor deposition

QCM Quartz crystal microbalance

SAM Self-assembled monolayer

SEM Scanning electron microscopy

SPS Sulfonated polystyrene

sADH Secondary alcohol dehydrogenase
sDH Sorbitol dehydrogenase
tBLM Tethered bilayer lipid membrane
TEM Transmission electron microscopy
TIRFM Total internal reflection fluorescence microscopy
TYR Tyrosinase

1 INTRODUCTION

1.1 Overview

Proteins are a class of bio-macromolecules, alongside carbohydrates, lipids, and nucleic acids, which make up the primary constituents of biological organisms. Proteins are polymers made up of a specific sequence of amino acids joined together by peptide bonds (Glass 1966; Alzagtat and Alli 2002; Vinson 2006). Proteins perform a wide variety of biological functions inside all the living cells. Some proteins are enzymes, which catalyze chemical reactions. Other proteins play structural or mechanical roles. Some other essential functions performed by proteins include immune response, and the storage and transport of various molecules.

Recent progress in proteomics allow proteins having desired functionalities to be identified, produced in recombinant hosts, purified, and optimized for particular applications. However, widespread scientific and commercial exploitation of proteins requires development of improved biomimetic interfaces with which to measure their activities. The development of interfaces could be especially challenging for membrane proteins (Sanders and Oxenoid 2000; Marsh, Horvath et al. 2002) because they also require an artificial cell membrane, called bilayer lipid membrane (BLM), to express their activities. Ideally, biomimetic interfaces should have the following performance properties: (1) versatile, for use with multiple classes of proteins, (2) customizable, for use in diverse applications, (3) robust, for long lifetimes and use in harsh conditions, and (4) mass-producible, for inexpensive fabrication.

This dissertation describes the fabrication and characterization of functional, three dimensional biomimetic interfaces consisting of proteins, lipid bilayers, polyelectrolytes

and other nanostructured components. These interfaces have some of the above mentioned desired characteristics, and were assembled using self assembly tools such as layer by layer assembly (LBL) introduced by Decher, microcontact printing (μ CP) developed by Whitesides and polymer on polymer stamping (POPS) developed by Hammond and co-workers. LBL assembly can be used to deposit polyelectrolyte multilayers (PEMs) on most substrates. PEMs are thin films (Decher and Hong 1991) formed by electrostatic interactions between oppositely charged polyelectrolyte species to create alternating layers of sequentially adsorbed ions. PEMs are economical to produce, and have been extended to functional polymers (Fou and Rubner 1995), colloids (Lee, Zheng et al. 2002; Zheng, Lee et al. 2002), biomaterials (Lvov, Ariga et al. 1995), separations (Bruening, Harris et al. 2001; Dai, Jensen et al. 2001; Balachandra, Dai et al. 2002; Dai, Balachandra et al. 2002; Stanton, Harris et al. 2003; Miller and Bruening 2004), and templates for selective electroless metal deposition (Lee, Hammond et al. 2003). μ CP (Kumar and Whitesides 1993) is a soft lithographic technique used in physics, chemistry, materials science and biology to transfer patterned thin organic films to surfaces, with sub-micron resolution. Unlike other fabrication methods that merely provide topographic contrast between the feature and the background, μ CP also allows chemical contrast to be achieved via selection of an appropriate ink. Microcontact printing offers several advantages over conventional photolithographic techniques because it is simple to perform and is not diffraction-limited. This technique has been used to make patterns of various small and large molecules on metals and silicon substrates (St. John and Craighead 1996; Xia, Kim et al. 1996; Kohli, Dvornic et al. 2004); as well as to deposit proteins (Kohli, Worden et al. 2005) and polyelectrolyte

aggregates (Lee, Ahn et al. 2004). POPS is an approach that combines LBL assembly and μ CP to generate alternating regions of different chemical functionalities on a surface by using graft, diblock copolymers or polyelectrolytes as ink (Jiang and Hammond 2000; Jiang, Zheng et al. 2002).

While each chapter in this thesis addresses a unique architecture or issue, the underlying theme of the study is the development of improved biomimetic architectures that express protein activities. These interfaces have outstanding potential for conducting fundamental studies of nanoscale biological processes and for developing new protein-based technologies, including high-throughput drug screening systems and novel biosensors.

Chapter 2 of this dissertation presents a nanostructured biosensor interface for measuring the activity and inhibition of NEST. In Chapter 3, an approach to generate highly sensitive phenol sensors is presented. In Chapter 4, a theoretical and experimental study of bi-enzyme electrodes where substrate recycling takes place is presented. In Chapter 5, an efficient approach for the fabrication of arrays of lipid bilayers on patterned PEMs is presented. In Chapter 6, a novel biomimetic interface consisting of an electrolessly deposited gold film overlaid with a tethered BLM (tBLM) is presented. In Chapter 7, an approach is presented that allows high-quality, 3D patterned bionanocomposite layered films to be constructed on substrates whose surface properties are incompatible with existing self-assembly methods. Chapter 8 presents an approach that can be used to create stable, nanostructured, amphiphilic and cross-linkable PAMAMOS-DMOMS dendrimer patterns.

1.2 Nanostructured biosensor for neuropathy target esterase activity

Organophosphorous compounds (OP) can cause at least two kinds of neurotoxic syndromes in humans and animals (Glynn 1999; Sigolaeva, Makower et al. 2001; Sokolovskaya, Sigolaeva et al. 2005). The first is the acute and sometimes fatal neurotoxicity that results from covalent inhibition of acetylcholinesterase (AChE) at cholinergic synapses. The second, OP-induced delayed neuropathy (OPIDN) is characterized by flaccid paralysis of the lower limbs 1-3 weeks after exposure to certain neuropathic OPs. These compounds covalently modify the neuronal membrane protein known as neuropathy target esterase (NTE). Recovery from this disease is usually poor, and there is no known effective treatment.

In addition to its role in chemically induced disease processes, NTE has recently been implicated in well-known motor-neuron diseases that occur spontaneously, without exposure to OP compounds. One of our collaborators, Dr. Rudy J. Richardson (Toxicology Program, Department of Environmental Health Sciences, University of Michigan) recently co-authored a groundbreaking conference paper that links a mutation in the gene encoding NTE to amyotrophic lateral sclerosis (ALS) (VandenDriessche 2005), also known as Lou Gehrig's disease. This paper, entitled, "Neuropathy target esterase gene mutations cause motor neuron disease," was presented at the 2005 American Society of Human Genetics meeting, Oct. 25-29, 2005, in Salt Lake City, UT.

Because NTE plays a central role in both chemically induced and spontaneously occurring neurological diseases, approaches that can help measure its esterase activity and inhibition are of tremendous scientific and commercial importance. In this part of the

dissertation, the first continuous, electrochemical biosensor for measuring the esterase activity of a fragment of NTE, known as NEST is presented. The biosensor also gives dose-dependent drop in sensor output to known NEST inhibitors. The interface was formed using LBL assembly of a polyelectrolyte poly-L-lysine and two proteins NEST and tyrosinase. Note that this is the first time that NEST has been immobilized in an active conformation on a surface.

While the development of NEST biosensor was the primary purpose of this study, we found that the same NEST biosensor approach can also be extended to measure the activity and inhibition of other medically relevant esterases such as acetylcholinesterase (AChE) and butyrylcholinesterase (BChE). AChE is found primarily in the blood and neural synapses (Herz and Kaplan 1973; Millard and Broomfield 1995; Davis, Britten et al. 1997; Lejus, Blanloeil et al. 1998; Hsieh, Deng et al. 2001). Pseudocholinesterase, also known as BChE, is found primarily in the liver (Darvesh, Hopkins et al. 2003). Both of these enzymes are esterases and catalyze the hydrolysis of the neurotransmitter acetylcholine into choline and acetic acid, a reaction necessary to allow a cholinergic neuron to return to its resting state after activation.

1.3 Highly sensitive phenol sensor based on layer by layer assembly

Phenols are present in waste-waters and exhaust gases of many industries, including oil refineries, coke plants, resins and plastics, dyes and chemicals, and textiles (Stanca, Popescu et al. 2003; Solna, Sapelnikova et al. 2005; Solna and Skladal 2005). Phenols, even in low concentrations, can cause serious problems because of their toxicity. The sensing of phenolic compounds is therefore essential to evaluate the risk of

environmental samples on our health. Chapter 3 presents an approach that can be used to develop highly sensitive phenol sensors by making alternative layers of PLL and tyrosinase on a gold electrode using LBL assembly. The sensitivities obtained using poly-L-lysine and tyrosinase multilayer films are about 2 orders of magnitude greater than those reported using other polyelectrolytes and tyrosinase multilayer systems, suggesting that the composition of polyelectrolytes may influence important factors such as enzyme loading and turnover number. The work described in Chapter 2 and Chapter 3 of this dissertation was done in collaboration with Devesh Srivastava (Advisor: Ilsoon Lee) in the Department of Chemical Engineering and Materials Science. The work consists of equal contribution from Devesh Srivastava and the author of this dissertation.

1.4 Theoretical and experimental study of bi-enzyme electrodes with substrate recycling

During the past decade, biosensors, because of their high selectivity, specificity and low cost for mass production, have become very popular in areas such as food technology, environmental monitoring and biomedical devices (Allen 1997; Vo-Dinh and Cullum 2000; Prodromidis and Karayannis 2002). Biosensors use a variety of methods for detecting the analyte of interest, including electrochemical (potentiometric, amperometric, conductometric) (Dzyadevych, Soldatkin et al. 2002; Gerard, Chaubey et al. 2002) optical (absorbance, fluorescence, luminescence, light scattering, refractive index) (DiazGarcia and ValenciaGonzalez 1995; Barak, Ferguson et al. 1997; Karlsson and Falt 1997), thermal (Abel, Weller et al. 1996; Ramanathan and Danielsson 2001), piezoelectric (Muramatsu, Dicks et al. 1987; Saini, Hall et al. 1991; Davis, Britten et al.

1997), and magnetic (Baselt, Lee et al. 1998). The electrochemical mode is generally the preferred mode of transduction for enzyme based biosensors.

The sensitivity of the biosensors can be increased dramatically (or amplified) by incorporating a substrate recycling scheme. In these devices the shuttle analyte is not only measured once, but is reconverted to be measured again. The shuttle analyte can either be the analyte of interest (the enzyme substrate) or can be produced by an additional enzyme reaction.

The range of analytes for which reporting interfaces (biosensors) can be developed can be increased substantially by coupling multiple protein activities into reaction pathways. For example, NEST biosensor (described earlier), couples NEST esterase activity with two tyrosinase oxidation activities.

In view of numerous applications of such multi-enzyme interfaces with amplified responses, for low concentrations of substrate, a theoretical model for a bi-enzyme rotating disk electrode having substrate recycling is presented in Chapter 4 of this dissertation. The bi-enzyme electrode was fabricated by co-immobilizing two enzymes: tyrosinase and NEST. The model was validated by studying the response of the bi-enzyme rotating disk electrode to phenyl valerate under varying rotating speeds. This model can help quantify the influence of mass transfer in bulk and enzyme layer, enzyme kinetics and electron transfer kinetics on the performance of biosensors. This information can be helpful in optimizing the performance characteristics of biosensors.

1.5 Arrays of lipid bilayers and liposomes on polyelectrolyte multilayer templates

Cell membranes represent one of the major structural components of biological cells. Cell membranes consist of lipids, membrane proteins and other major biomacromolecules interposed between them. These membrane proteins perform many vital sensing, signaling, catalytic, transport, and bioelectronic processes at the molecular scale. Widespread scientific and commercial exploitation of membrane proteins requires development of improved biomimetic interfaces that can express and /or to measure their activities.

Biosensors or biomimetic interfaces that rely on membrane bound proteins or enzymes, often incorporate artificial bilayers (BLMs) in their design. The BLMs are necessary in order to preserve the functional characteristics of the proteins that are bound to them. BLMs may be deposited on the biosensor interface using Langmuir-Blodgett deposition methods or liposome adsorption. The choice of lipids used to construct BLMs is important, as the characteristics of the resulting BLM have a very strong influence on the activity of the membrane protein. Properties such as membrane fluidity, which is an indicator of the ability of lipid molecules to diffuse freely through the bilayer, play important roles in maintaining the correct conformation of the embedded biomolecules. For certain membrane proteins such as ion channels, it is also important to have BLMs that are highly insulating, since the presence of large defects will render such sensors ineffective (Raguse, Braach-Maksvytis et al. 1998).

In recent years, considerable developments have been made in the area of polymeric cushions upon which BLMs can be deposited (Sackmann and Tanaka 2000).

In addition to being able to provide ionic reservoirs, polymeric cushions allow extra-membrane portions of membrane proteins to attain their necessary conformation and to retain biological activity. Without the cushions, interactions between the substrate surface and protein might impede proper function. The use of PEMs has been proposed as one such viable method for a polymeric cushion.

Chapter 5 presents a novel approach to fabricate arrays of BLMs on patterned PEMs. The patterned PEMs were deposited using microcontact printing and alternating deposition of positively charged and negatively charged polyelectrolytes. Arrays of BLMs were fabricated using exposure of patterned PEMs to liposomes of various compositions. The deposition of liposomes on the PEMs was monitored using total internal reflection fluorescence microscopy, fluorescence microscopy and gravimetry. The resulting BLMs were characterized using fluorescence recovery after pattern photobleaching (FRAPP). Bilayer formation on two different kinds of PEM substrates was studied. Such arrays can be used in applications such as high throughput screening, and for conducting fundamental studies of nanoscale biological processes. This work was done in collaboration with Sachin Vaidya (Advisor: Robert Ofoli) in the Department of Chemical Engineering and Materials Science. The work consists of equal contributions from Sachin Vaidya and the author of this dissertation.

1.6 Tethered lipid bilayers on electrolessly deposited gold for bio-electronic applications

Biomimetic interfaces, consisting of tBLMs with membrane proteins incorporated into them or bound to them, have primarily been used for sensing applications. New

approaches that can increase the range of tBLMs applications to include areas such as biocatalysis and biofuel cells are of scientific and commercial interest. One of the major challenges in the commercialization of such biomimetic interfaces is the cost of gold electrodes on which the tBLM are deposited. Although methods such as chemical vapor deposition (CVD) and physical vapor deposition (PVD) are generally used to deposit gold, these methods are very expensive and also suffer from some limitations such as: i) they cannot uniformly coat the pores of porous substrates, ii) they generally require an adhesion layer. Therefore, there is a need to reduce the fabrication cost and overcome some of the limitations associated with CVD and PVD.

Electroless deposition is an inexpensive metal-plating technique that, unlike CVD and PVD, can easily be performed on a laboratory bench top and in aqueous solutions. It can be used to tune the properties of arrays or films of metals with nanometer-scale precision on virtually any surface, including glass, silicon wafers, and mechanically flexible plastics. Porous substrates are generally used as electrodes in biocatalytic reactors and biofuel cells. CVD and PVD are expensive and poorly suited to uniformly coating the internal pore surfaces of porous substrates. However, electroless deposition allows the metal plating solution to be drawn in to pores because of capillary action, thus offering the potential for both coating of internal pores and low processing costs.

Chapter 6 presents an economical and versatile approach that can easily be extended to fabricate functional and nanostructured biomimetic interfaces on a wide variety of surfaces including electrodes of biocatalytic reactors, thus increasing the repertoire of tBLM based applications. The approach entails combining electroless metal deposition and molecular self assembly to sequentially deposit a conductive gold layer

and tBLM on a substrate. To confirm the activity of tBLMs, two biomolecules were also incorporate into them: the ionophore valinomycin and NEST. Electrochemical impedance spectroscopy (EIS), UV/Visible spectroscopy and fluorescence recovery after pattern photobleaching (FRAPP) were used to characterize the resulting biomimetic interfaces and confirm membrane biomolecule activity. Microcontact printing was used to deposit arrays of tBLMs on electrolessly deposited gold patterns. The resulting arrays were characterized using atomic force microscopy (AFM), field-emission scanning electron microscopy and energy dispersive spectroscopy (EDS).

1.7 Intact transfer of layered bio-nanocomposite films on polyelectrolyte templates

Functional, 3-D nano and microarrays composed of molecules such as proteins, lipids, polyelectrolytes and dendrimers have potential applications in drug screening devices, novel biosensors, biocatalysis, optoelectronics, and other devices (Blawas and Reichert 1998; Lee, Zheng et al. 2002; Kidambi, Chan et al. 2004). Chapter 7 of this dissertation presents an approach that can be used to deposit high-quality microarrays of layered, bionanocomposite films on a wide variety of substrates. As examples of this approach, the fabrication and characterization of some 3-D nanostructured architectures (or structures) consisting of dehydrogenase enzymes, polyamidoamine (PAMAM) dendrimers and PEMs, is presented.

The approach presented in this chapter overcomes a problem encountered when using microcontact printing to establish a pattern on the target surface and then building sequential layers on the pattern via LBL self-assembly. Amphiphilic molecules tend to

adsorb both to the patterned features as well as the underlying substrate, resulting in low-quality patterns. By circumventing this problem, this research is expected to significantly extend the range of surfaces and layering constituents that can be used to fabricate 3D, patterned, bionanocomposite structures. Fluorescence microscopy and AFM were the primary characterization techniques used to demonstrate the feasibility of this approach for making these 3D bionanocomposite arrays.

1.8 Nanostructured cross-linkable micropatterns via amphiphilic dendrimer stamping

Dendrimers are radially symmetrical polymeric molecules that are grown by sequential addition of branched monomers to the outer shell.⁷ With each new addition (generation), the molecular weight of the dendrimer and the density of its terminal functional groups increase substantially. Radially layered poly-(amidoamine-organosilicon) (PAMAMOS) dendrimers represent a unique, highly diverse class of amphiphilic and cross-linkable globular-shaped dendrimers.

In this Chapter, we report the first application of microcontact printing of the amphiphilic and cross-linkable PAMAMOS-DMOMS dendrimers on glass slides, silicon wafers and polyelectrolyte multilayers (PEMs) in which the pattern average thickness was controlled by spin-self assembly (i.e., spin-inking). The resulting 3-D micro-patterned amphiphilic networks were characterized by optical microscopy and atomic force microscopy (AFM). Also, the effects of dendrimer ink concentration, inking method and contact time on the thickness, uniformity and stability of the deposited patterns are presented. The results provide a framework for controlling the geometry of the deposited patterns. The lateral

footprint of the pattern can be controlled by the shape of the elastomeric stamp, and the thickness of the patterns can be controlled by adjusting the spin coating method, the surface properties of the stamp, and the substrate used. The results also confirmed the well-known influences of spin speed, concentration, and solvent on the thickness of spin coated films. These versatile dendrimer arrays have potential applications in the development of high throughput drug screening systems and could serve as templates for nanoparticles growth or electroless metallization in development of nano metal reactors on micropatterned films.

2 NANOSTRUCTURED BIOSENSOR FOR MEASURING NEUROPATHY TARGET ESTERASE ACTIVITY

2.1 ABSTRACT

Neuropathy target esterase (NTE) is a membrane protein found in human neurons, and other cells, including lymphocytes. Binding of certain organophosphorus (OP) compounds to NTE is believed to cause OP-induced delayed neuropathy (OPIDN), a type of paralysis for which there is no effective treatment. Mutations in NTE have also been linked with serious neurological diseases, such as Lou Gehrig's disease. In this paper, for the first time, a nanostructured biosensor containing a domain of NTE known as NEST has been developed. The biosensor was fabricated, using layer by layer assembly approach, by immobilizing a layer of NEST on top of multilayers consisting of a polyelectrolyte (poly-L-lysine) and a protein (tyrosinase). The biosensor has a response time on the order of seconds and gives dose-dependent decrease in sensor output in response to known NEST (or NTE) inhibitors. Potential applications of the biosensor include studying the fundamental reaction kinetics of NTE mutants, screening OP compounds for NTE inhibition, and investigating the effect of NTE mutations on NTE esterase activity. While the development of a NEST biosensor was the primary purpose of this study, we found that the approach developed for NEST can also easily be extended to immobilize and measure the activity of other medically relevant esterases such as acetylcholinesterase (AChE) and butyrylcholinesterase (BChE). Based on the measured sensitivities, phenyl valerate was found to be the best substrate for NEST and BChE. On the other hand, phenyl acetate gave the highest sensitivity with AChE. Potential step

amperometry and ellipsometry were the primary characterization techniques used in this study.

2.2 INTRODUCTION

Neuropathy target esterase (NTE), a membrane-bound esterase found in neurons of vertebrates (Glynn 1999; Atkins and Glynn 2000; van Tienhoven, Atkins et al. 2002; Li, Dinsdale et al. 2003; Makhaeva, Sigolaeva et al. 2003; Kropp, Glynn et al. 2004), has been shown to be necessary for embryonic development in mice, and is believed to be involved in cell-signaling pathways and lipid trafficking (Glynn 1999). NTE has serine esterase activity and can hydrolyze ester, peptide, and amide bonds. The nucleophilic serine residue (active site) of NTE attacks the carbonyl carbon atom of the substrate, forming a covalent acyl-enzyme intermediate, which is subsequently hydrolyzed. A consequence of this reaction mechanism is that the esterase activity of NTE is susceptible to covalent inhibition by organophosphorus esters (OPs) with which it forms an analogous phosphyl-enzyme intermediate. Irreversible binding of some OP compounds to the active serine site results in a debilitating neural disease known as (OP)-induced delayed neuropathy (OPIDN) (Glynn 1999). Symptoms of OIPDN include flaccid paralysis of the lower limbs, which becomes evident two to three weeks after exposure to neuropathic OPs. Recovery from this disease is usually poor, and there is no specific treatment. Because NTE is difficult to produce for research purposes, research to study its esterase activity is typically done using a fragment of the NTE protein that contains the esterase activity and can be more easily produced. One such fragment known as NEST (NTE esterase domain) (Atkins and Glynn 2000; Forshaw, Atkins et al. 2001; Kropp, Glynn et al. 2004) reacts with esters and inhibitors in a manner very similar to NTE.

Widespread and long-term use of OP compounds in industry and agriculture has made these hazardous compounds a part of environment, posing a health risk. Also, neuropathic compounds could potentially be used as chemical weapons. In addition to its role in chemically induced disease processes, NTE has been implicated in well-known motor-neuron diseases that don't require exposure to OP compounds. Recently, a conference paper linked a mutation in the gene encoding NTE to amyotrophic lateral sclerosis (ALS), also known as Lou Gehrig's disease (Rainier, Bui et al.).

Because NTE plays a central role in both chemically induced and spontaneously occurring neurological diseases, approaches that can help measure its esterase activity and inhibition are of tremendous scientific and commercial importance. Conventionally, the esterase activity of NTE (or NEST) is measured using two distinct steps. In the first step, a solution containing phenyl valerate is brought into contact with NEST or NTE protein solution, whose esterase activity reacts with a portion of the artificial substrate phenyl valerate to form phenol. In the second step, the concentration of phenol in the solution is determined either colorimetrically, in the presence of 4-amino antipyrine (Kayyali, Moore et al. 1991), or electrochemically, in the presence of tyrosinase enzyme (Sigolaeva, Makower et al. 2001; Sokolovskaya, Sigolaeva et al. 2005). Tyrosinase converts phenol first to catechol and then to *o*-quinone, which can be measured electrochemically at an electrode (Makhaeva, Sigolaeva et al. 2003). The current generated by the electrode increases with the amount of *o*-quinone present, thus giving an indirect measurement of the amount of NTE esterase activity present during the first step. To test for esterase inhibition, this procedure is repeated both in the absence and presence of a putative inhibitor (e.g. an OP compound). A reduced signal indicates inhibition of

the esterase activity. This method has the disadvantages of being slow, and requiring two steps, making it unsuitable for some important applications, such as high-throughput screening of compounds for NTE inhibition and continuous, on-line, environmental monitoring to detect chemical warfare agents that target NTE.

This paper presents the first continuous, electrochemical biosensor for real-time, rapid measurement of NEST (or NTE) esterase activity. The biosensor was fabricated by co-immobilizing NEST protein and tyrosinase enzyme on an electrode using layer by layer assembly approach (Decher 1997). To our knowledge, this is the first time NEST has been immobilized in an active conformation on an electrode. Potential applications of this sensor include detecting the presence of chemical weapons that target NTE, screening industrial and agricultural OP compounds for NTE inhibition, studying the fundamental reaction kinetics of NTE, and investigating the effect of NTE mutations found in ALS patients on NTE's enzymatic properties.

While the primary purpose of this paper was the development of NEST biosensor, we found that the approach can also easily be extended to measure the activity of other medically relevant esterases such as AChE and BChE. AChE, also known as true cholinesterase is found primarily in neural synapses (Herz and Kaplan 1973; Davis, Britten et al. 1997; Lejus, Blanloeil et al. 1998; Hsieh, Deng et al. 2001). BChE, also known as pseudocholinesterase is found primarily in the blood plasma (Lejus, Blanloeil et al. 1998; Darvesh, Hopkins et al. 2003). Although both of these enzymes are capable of hydrolyzing the neurotransmitter acetylcholine into choline and acetic acid, a reaction necessary to allow a cholinergic neuron to return to its resting state after activation, they differ in their respective reactivities toward substrates. AChE prefers acetylcholine,

whereas BChE prefers butyrylcholine. Inhibition of neural AChE can produce cholinergic toxicity and death. BChE inhibition is not known to have direct toxic effects, but it can serve as a biomarker of exposure to OP compounds (Thompson and Richardson 2004).

2.3 EXPERIMENTAL SECTION

2.3.1 Materials

Thioctic acid, poly-L-lysine (PLL) (molecular weight ~ 15,000), tyrosinase (Tyr), sodium phosphate (monobasic and dibasic), ethylenediaminetetraacetic acid (EDTA), sodium chloride, 3-[(3-cholamidopropyl) dimethylammonio]-1-propanesulfonate (CHAPS) and isopropyl thiogalactoside (IPTG), AChE, and BChE were obtained from Sigma (St. Louis, MO). All the chemicals were of the highest purity available. Ultrapure water was supplied by a Nanopure-UV four-stage purifier (Barnstead International, Dubuque, IA); the purifier was equipped with a UV source and a final 0.2 μm filter.

2.3.2 NEST expression and purification

NEST was expressed and purified according to published procedures (Atkins and Glynn 2000). Briefly, DNA fragment encoding NEST was cloned into pET-21b vector, and the resulting expression vector was transformed into *E. coli* BL21(DE3). An overnight culture of transformed *E. coli* was inoculated with M9 media containing ampicillin and grown in a fermentor. IPTG was added to the resulting cell culture after a day to induce the expression of NEST. The resulting cells were collected 4 h after induction by centrifugation and subjected to protein expression techniques. Briefly, 5 g of cell paste was suspended in 30 ml of PEN buffer (50mM potassium phosphate/0.3 M NaCl/0.5 mM EDTA, pH 7.8) containing 2% CHAPS and tip sonicated four times. The

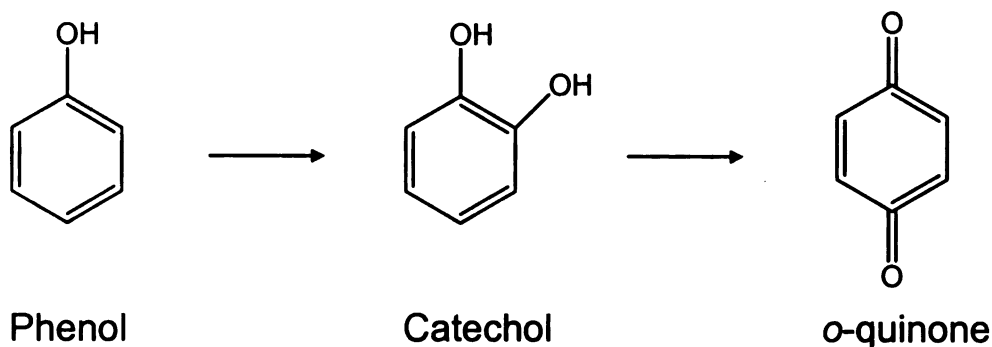
cell lysate was centrifuged at 2000 g for 30 min at 4°C, the supernatant was collected, and about 7 mL of supernatant was added to a mini column (volume 10 mL) containing 3 mL of Ni-NTA resin. The mini column was rotated at room temperature for 20 min, centrifuged at 2000 g for 20 sec and then the top solution was drawn off. The histidine tagged NEST was eluted from the Ni-NTA resin using 10 mL of PEN buffer containing 0.3% CHAPS and 0.3 M imidazole. The protein purity was determined using SDS PAGE and protein concentration was determined using BioRad Dc protein assay kit using albumin as the standard. For long term storage, 25% glycerol was added to the protein solution, which was then stored at -20 °C. The cloning and fermentation part of this procedure was done by Dr. Jun Sun (Manager, Protein Expression Laboratory, MSU) and the purification part was done by the author of this dissertation.

2.3.3 Preparation of phenyl valerate solution

To prepare phenyl valerate solution, 15 mg of phenyl valerate was dissolved in 1 mL of dimethylformamide (DMF), and 15 mL of water containing 0.03% Triton was added slowly under vigorous stirring. For potential step voltammetry experiments, small aliquots of the resulting phenyl valerate micellar solution (5.286 mM) were added to the phosphate buffer to obtain the desired concentrations.

2.3.4 Preparation of gold electrode for NEST biosensor

Tyrosinase is a copper-containing oxidase (Forzani, Solis et al. 2000; Coche-Guerente, Labbe et al. 2001), which possesses two different activities, as illustrated in reaction 2.1.



(2.1)

The first step is referred to as the enzyme's hydroxylase activity (also known as cresolase activity) where phenol is hydroxylated by the aid of molecular oxygen to produce catechol. In the second step, known as the catecholase activity, the enzyme oxidizes catechol to *o*-quinone and is simultaneously oxidized by oxygen to its original form, with the production of water. The reaction product, *o*-quinone, is electrochemically active and can be reduced back to the catechol form at low applied potentials, as illustrated in reaction 2.2.



These characteristics of tyrosinase were exploited by us to fabricate a NEST biosensor, capable of measuring the NEST's esterase activity and its inhibition, by co-immobilizing NEST and tyrosinase on a gold electrode using LBL assembly approach.

The molecular architecture of the biosensor interface is shown schematically in Figure 2.1. Gold electrodes cleaned in Piranha solution, were dipped in 5 mM solution of thioctic acid in ethanol for 1 hr. The electrodes were washed with ethanol, dried under nitrogen and dipped in PLL solution for 45 min. The PLL solution was prepared by

adding 12 mg of PLL in 50 mL of 20 mM phosphate buffer (pH 8.5). The electrodes were then rinsed with water and dipped in a solution of tyrosinase (0.2 mg/ml) for 1 h. The last two steps were repeated 3.5 times to create 3.5 PLL-Tyr bilayers with PLL being the topmost layer. The electrodes were washed with water and dipped in a solution of NEST protein (0.1 mg/mL) in 0.1 M phosphate buffer, pH (7.0) for 1 h. The electrodes were then washed with water, dried under nitrogen and dipped in phosphate buffer (0.1 M, pH 7.0) for testing.

2.3.5 Preparation of gold electrode for measuring the activity of AChE and BChE

To immobilize AChE or BChE, we used the same procedure as for the NEST biosensor, except that instead of the NEST solution, the final dipping was done in 0.1 mg/mL phosphate buffer solution (pH 7.0) of AChE or BChE.

2.3.6 Ellipsometry

Ellipsometric measurements were obtained with rotating analyzer ellipsometer (model M-44; J.A. Woollan Co. Inc., Lincoln, NE) using WVASE32 software. The thickness values for dried films were determined using 44 wavelengths between 414.0 and 736.1 nm. The angle of incidence was 75° for all experiments. Refractive indices of films containing PLL and proteins were assumed to be $n = 1.5$, $k = 0$. These optical constants compare well with those determined for 4 bilayer films consisting of poly-L-lysine and tyrosinase using ellipsometry.

2.3.7 Potential step amperometry and other measurements

The electrodes (sensors) were maintained at a potential of -100 mV (vs Ag/AgCl reference electrode) using a BAS CV-50W electrochemical analyzer. The esterase

activity of NEST biosensor was monitored by measuring the output current for a variety of phenyl valerate concentrations, under stirred conditions. The NEST protein converts phenyl valerate to phenol, which gets converted to *o*-quinone by tyrosinase. The *o*-quinone gets reduced at the electrode's surface, resulting in the generation of current. The electroreduction of *o*-quinone produces catechol which again gets converted to *o*-quinone by tyrosinase, thus amplifying the signal.

To measure inhibition of the esterase activity, a known quantity of phenyl valerate was added to the phosphate buffer (pH 7.0), under stirred conditions. After the stabilization of current, a known amount of NEST inhibitor was added, and the resulting drop in current was measured. Unless otherwise specified, all the errors reported in this chapter are σ (where σ is the standard deviation obtained using 10 electrodes).

2.4 RESULTS AND DISCUSSION

2.4.1 Ellipsometry

Ellipsometry was used to confirm the deposition of different layers that make up the NEST biosensor. As shown in Figure 2.2, the thickness increase following the addition of first PLL and Tyr bilayer was approximately 9.3 ± 0.4 nm. The thickness increase for the next two PLL-Tyr bilayers was the same and approximately equal to 7.2 ± 0.3 nm. The thickness increase following the addition of final PLL-NEST bilayer was approximately 6.6 ± 0.3 nm.

2.4.2 Amperometric response

2.4.2.1 Dependence of current response on working potential and pH

The various experimental parameters (such as pH and applied potential), which can affect the amperometric determination of phenyl valerate, were optimized. The effect of applied potential on the amperometric response of the sensor was tested in the range between 0.05 and -0.20 V. Figure 2.3 shows the steady state response of the biosensor both in the presence and absence (background current) of phenyl valerate. The background current is thought to result largely from the direct reduction of dissolved oxygen. The highest signal-to background ratio, was obtained at -0.1 V. At working potential more negative than -0.1 V, higher signals were obtained, but the background current also increased distinctly. Therefore, a working potential of -0.1 V was used for further studies.

The effect of pH was also studied in the pH range 5.5 to 8.0 in 0.1 M phosphate buffer at working potential of -0.1 V. As shown in Figure 2.4, the response current attained a maximum value at pH 7.0. This pH was used for further studies.

2.4.2.2 Measurement of esterase activity using NEST biosensor

Figure 2.5a displays a typical current-time response under the optimal experimental conditions after the successive addition of aliquots of phenyl valerate in the buffer to obtain final concentrations as increments of 4 μM . A well defined reduction current, proportional to the amount of phenyl valerate, was observed. The response time of the electrode was less than 20 s, due to the nano-scale thickness of the interface. The response to phenyl valerate was linear ($R^2 = 0.981$) in the range 0.5 μM to 12 μM , and it

reached saturation at approximately 30 μM (Figure 2.5b). The limit of detection was 0.5 μM at a signal-to-noise ratio of 3. The reproducibility of the sensor was investigated at a phenyl valerate concentration of 4 μM ; the mean current was approximately 350 nAcm^{-2} , with a standard deviation of approximately 10%. Figure 2.6 shows a control experiment which was done on an electrode containing only PLL-Tyr bilayers. As expected, a relatively very small rise in steady state current was observed on the addition of phenyl valerate. The small rise can be attributed to the presence of small amount of phenol produced due to auto hydrolysis of phenyl valerate solution.

It may be noted that the primary purpose of this study was the development of an approach that can be used to measure NEST esterase activity and inhibition; 3 PLL-tyr layers and one NEST layer gave us sufficient current sensitivity to check for the feasibility of the proposed approach. However, if some application requires higher sensitivities, then our preliminary results (data not shown) suggest that it can be achieved by further increasing the number of tyrosinase or NEST layers.

2.4.3 *Amperometric response to catechol and phenol*

Since tyrosinase can convert both catechol and phenol to quinone, the amperometric response of the NEST biosensor to these compounds was also studied. Figures 2.7a and 2.8a show the current-time response curve after the successive addition of aliquots of phenol and catechol, respectively. Figure 2.7b and 2.8b show the corresponding phenol and catechol calibration plots. The response to phenol was linear ($R^2 = 0.980$) in the range 1 to 25 μM , with an average sensitivity of approximately 410 (± 30) $\text{nA}\mu\text{M}^{-1}\text{cm}^{-2}$, and it reached saturation at approximately 65 μM . On the other hand,

the response to catechol was linear ($R^2 = 0.982$) in the range 1 to 40 μM , with a sensitivity of $2.5 (\pm 0.1) \mu\text{A}\mu\text{M}^{-1} \text{cm}^{-2}$, and it reached saturation at approximately 80 μM .

2.4.4 Inhibition of esterase activity

To measure inhibition of the esterase activity, an aliquot of phenyl valerate was added to the phosphate buffer. After a steady biosensor signal was obtained, a known quantity of phenylmethylsulfonyl fluoride (PMSF), a non-neuropathic compound previously shown to inhibit NEST (or NTE) esterase activity, was added to the phosphate buffer solution, and the resulting drop in current was measured. As shown in Figures 2.9, 2.10 and 2.11 there was no decrease on the addition of 10 μM PMSF, a 20% ($\pm 3\%$) decrease in response on the addition of 100 μM PMSF and a 70% ($\pm 4\%$) decrease on the addition of 1000 μM PMSF. PMSF inhibition of NEST esterase activity reduces the amount of phenol and subsequently *o*-quinone produced. Therefore, less of *o*-quinone gets reduced at the electrode surface, leading to a drop in current. A similar dose-dependent drop in current was observed when a neuropathic OP compound, MIPAFOX (data not shown), was added to the phosphate buffer. These results suggest that the NEST biosensor can be used for dose dependent detection of NEST inhibitors.

2.4.5 Storage stability

The sensors storage stability was tested by storing it at 4°C in phosphate buffer, pH 7.0, over one month, while intermittently measuring the current response to phenyl valerate standard solution every other day. The results showed that the activity of sensor remained stable for a week and then reduced gradually, with a half life of 15 days.

2.4.6 Immobilization of AChE and BChE

While the development of NEST biosensor was the primary purpose of this study, we found that the same PLL-Tyr multilayer interface could also be used to immobilize and measure the activity of other esterases such as AChE and BChE. Figure 2.12 displays a typical current-time response, for a bi-enzyme electrode containing tyrosinase and AChE, after the successive addition of aliquots of phenyl acetate to the phosphate buffer. A reduction current proportional to the amount of phenyl acetate was observed. The response to phenyl acetate was also found to be linear ($R^2 = 0.989$) in the range 0.5 μM to 16 μM and it reached saturation at approximately 40 μM . No significant rise in current was observed, when phenyl valerate instead of phenyl acetate was used as a substrate on this interface. This result suggests that phenyl acetate is a much better substrate for acetylcholinesterase than phenyl valerate. Current time response curves similar to Figures 2.5 and 2.12 were also obtained with bi-enzyme electrodes consisting of tyrosinase and BChE, with the highest current sensitivity being obtained when phenyl valerate was used as a substrate. Table 2.1 summarizes the current sensitivities obtained with three different bi-enzyme interfaces. Control experiments were also done in which each of the substrate was delivered to a gold electrode containing only PLL-Tyr bilayers. The current sensitivities obtained in these control experiments were always less than 0.5 $\text{nA}\mu\text{M}^{-1}\text{cm}^{-2}$. Collectively, these interfaces can be used for simultaneously detecting the presence of a variety of compounds which inhibit cholinesterases and also for studying cholinesterase reaction kinetics.

2.4.7 Significance of NEST biosensor

This new biosensor approach to measuring NEST esterase activity and its inhibition can in principle easily be extended to full length NTE. The approach offers several advantages over the old two step method. First, it requires only a single step to measure NEST (or NTE) esterase activity. Because the NEST esterase activity is co-immobilized with tyrosinase on the sensor interface, the presence of phenyl valerate triggers sequential reactions that result in an electrical signal. Second, the nanometer-scale thickness of layers in the sensing interface provides a very short diffusion path giving a rapid response time (less than 10 seconds). Third, the biosensor is suitable for continuous, real-time measurements of esterase activity. Fourth, the biosensor is designed to achieve signal amplification via recycle of o-quinone to catechol, thus increasing the sensitivity of the sensor. Fifth, the biosensor interface is generated by flexible, layer-by-layer, molecular self-assembly methods that would allow it to be assembled on electrodes inside microfluidic channels, thus enabling the production of high-density biosensor arrays consisting of various esterases for high-throughput applications.

This combination of desirable properties makes this interface well suited for important applications, including studying the kinetic properties of esterases such as NEST protein, high-throughput screening of compounds for NEST (or NTE) inhibition and continuous, on-line, environmental monitoring to detect chemical warfare agents that target NEST (or NTE) and other esterases.

2.5 CONCLUSIONS

A biosensor has been developed that allows the activity of NEST to be measured continuously. The biosensor was fabricated by layer-by-layer assembly approach to co-immobilize NEST and tyrosinase on a gold electrode. Ellipsometry provided evidence for the sequential assembly of the multiple layers that make up the interface. Constant potential amperometry allowed NEST enzyme activity to be measured with a rapid response time (< 10 s). The biosensor gave dose-dependent response to known non-neuropathic (PMSF) and neuropathic (Mipaflox) NEST inhibitors. The same interface can also be used to immobilize and measure the activity of other medically relevant esterases such as AChE and BChE.

2.6 RECOMMENDATIONS FOR FUTURE WORK

It will also be interesting to work on approaches that can help us improve the long-term stability of the bi-enzyme electrodes. One of the approaches could be dipping the bi-enzyme electrode in some stabilizing solution such as sucrose or trehalose solution. Another approach could be using some kind of cross-linking agent such as glutaric dialdehyde which can cross-link proteins and poly-L-lysine. It will also be equally interesting to try this approach on other medically relevant esterases such as alkaline phosphatase. In this case phenyl phosphate may be tried as one of the substrate.

Another recommendation will be to integrate micro-fluidics and semi-conductor fabrication methods to generate bi-enzyme biosensor electrode arrays. Semi-conductor fabrication methods can be used to generate gold arrays on a silicon chip. Because all the interfaces presented in this paper can be fabricated using layer-by-layer assembly from

different solutions, microfluidics can be used to fabricate different interfaces on different electrodes. Micro-fluidics in conjunction with potential step voltammetry can then be used to measure the response of different bi-enzyme electrodes to different analytes. These electrode arrays may have outstanding potential for food-safety and homeland security applications.

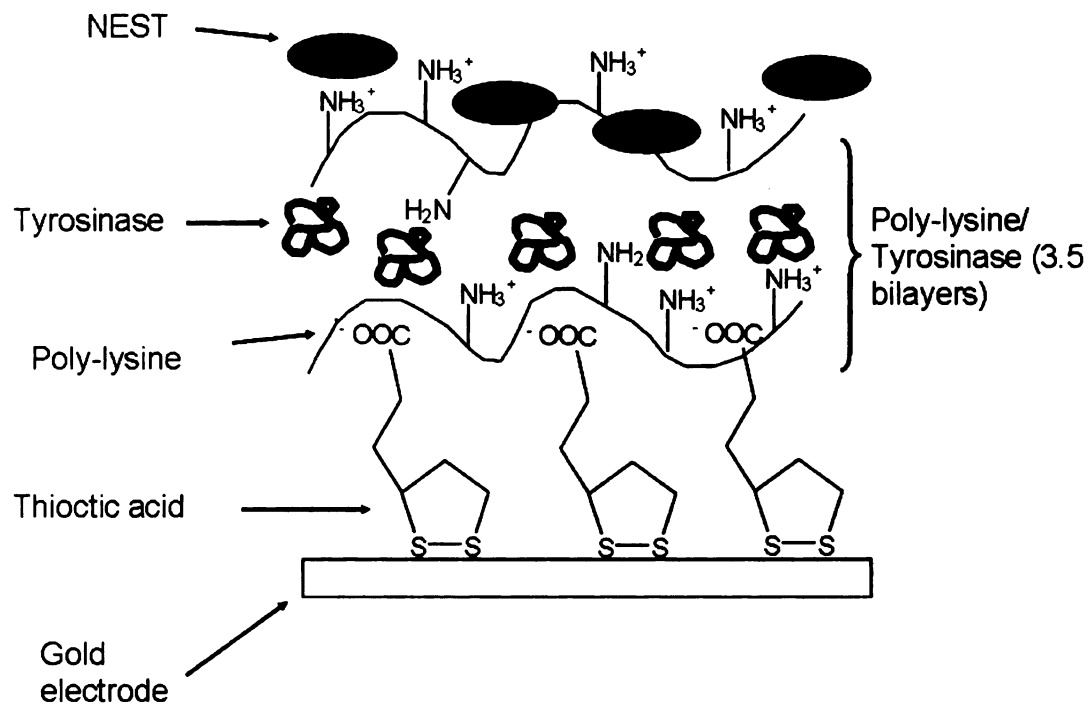


Figure 2.1: Molecular architecture of the NEST biosensor.

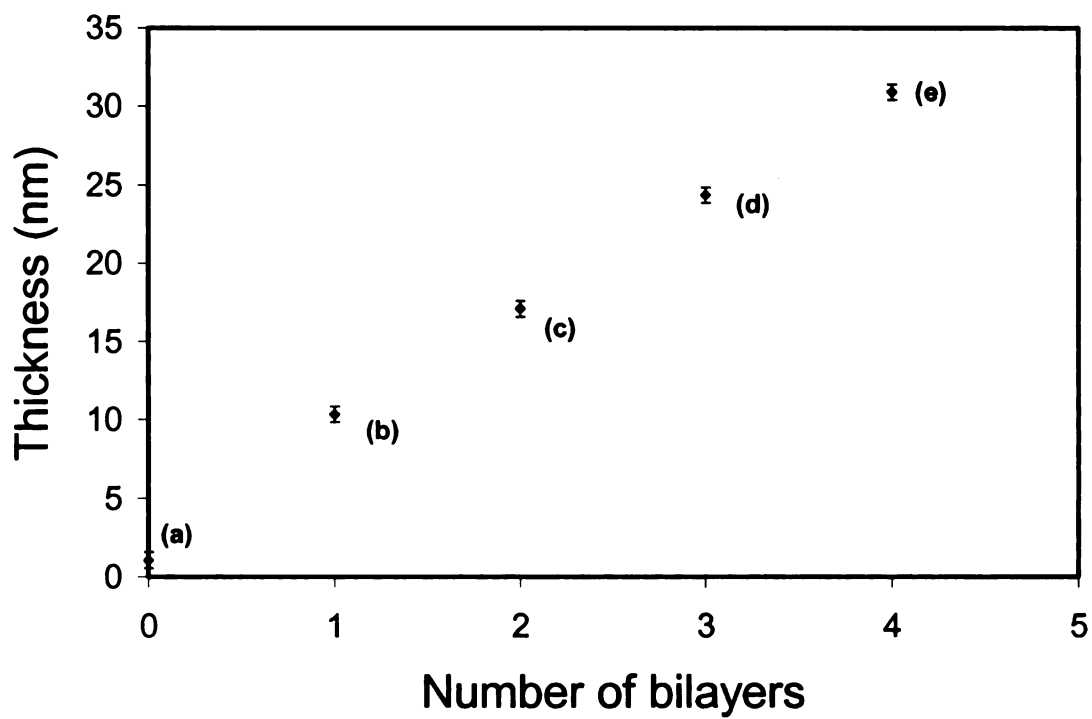


Figure 2.2: Ellipsometric thicknesses after the successive addition of following layers: thioctic acid (point a), PLL-Tyr first bilayer (point b), PLL-Tyr second bilayer (point c), PLL-Tyr third bilayer (point d), and PLL and NEST final bilayer (point e).

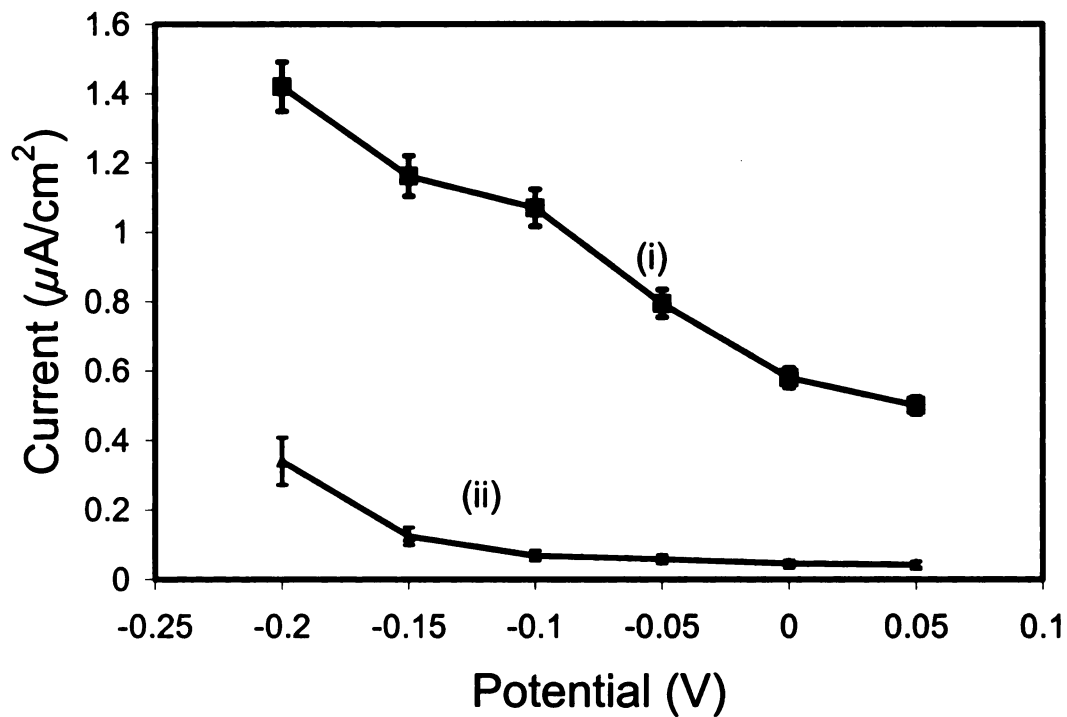


Figure 2.3: Effect of working potential on the response current of the enzyme electrode in 0.1 M phosphate buffer (pH 7.0) with (i) and without (ii) 12 μM phenyl valerate solution, in 0.1 M phosphate buffer at an applied potential of -0.1 V (vs Ag/AgCl).

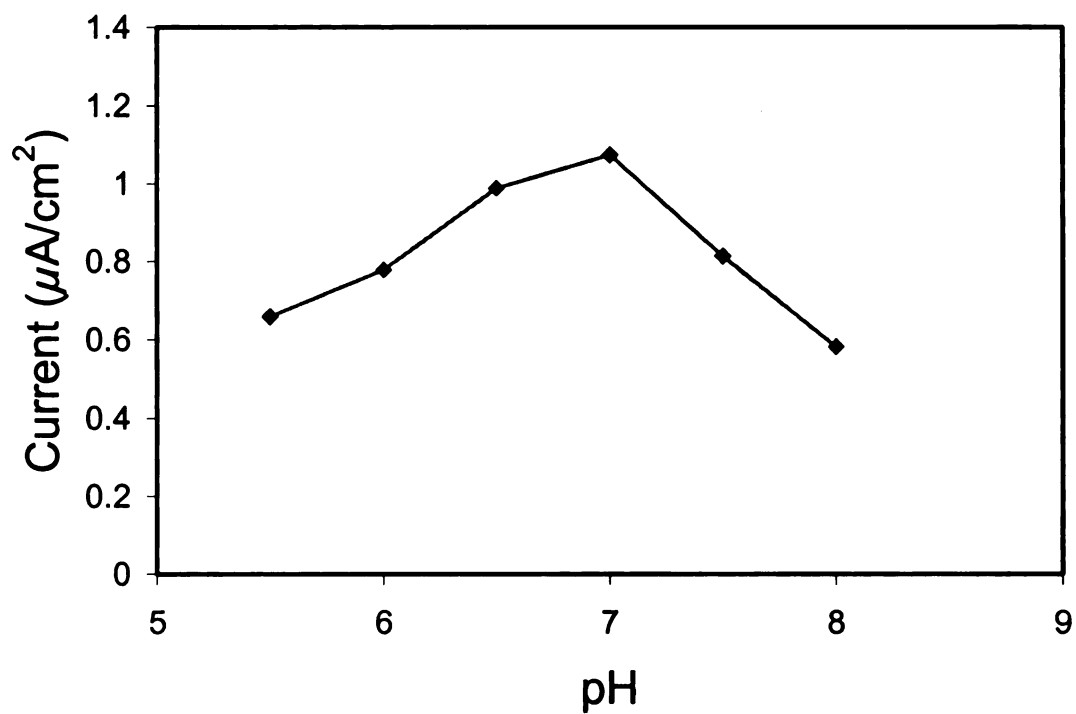
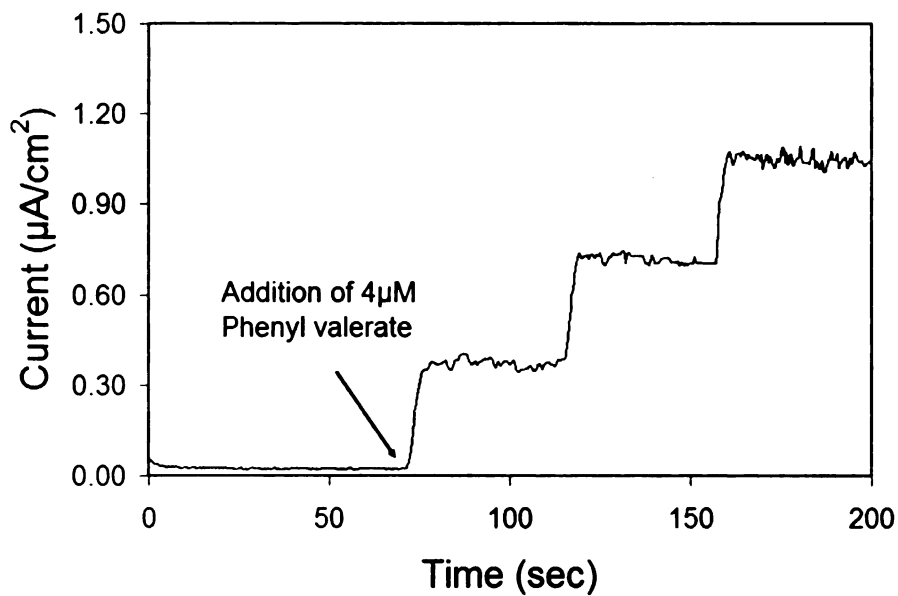
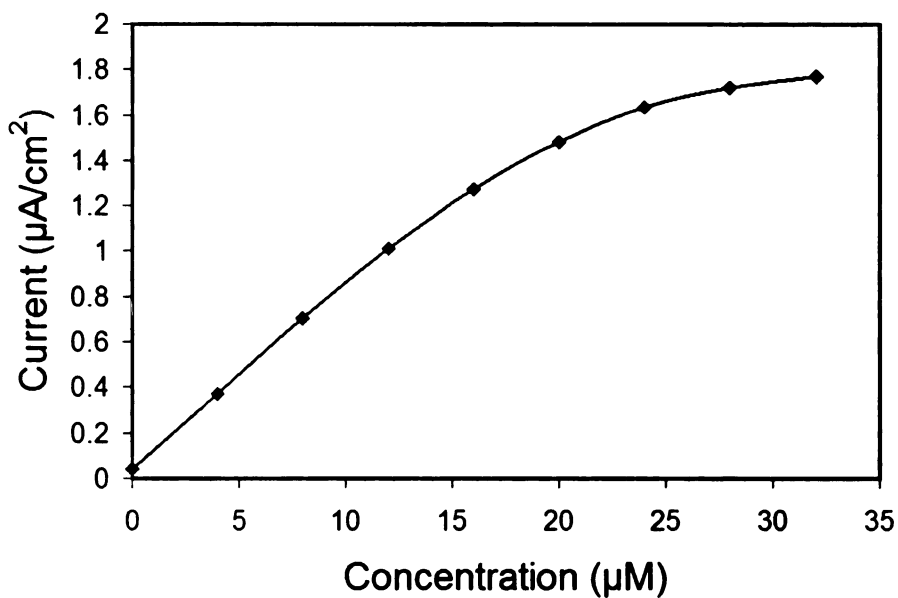


Figure 2.4: Effect of pH on the response current of the electrode, in the presence of 12 μM phenyl valerate solution, in 0.1 M phosphate buffer at an applied potential of -0.1V (vs Ag/AgCl).



(a)



(b)

Figure 2.5: (a) Current time response of the NEST biosensor to the addition of aliquots of phenyl valerate to obtain final phenyl valerate concentrations as increments of 4 μM , in 0.1 M phosphate buffer, pH 7.0, at an applied potential of -0.1V (vs Ag/AgCl). (b) Representative example of a calibration plot.

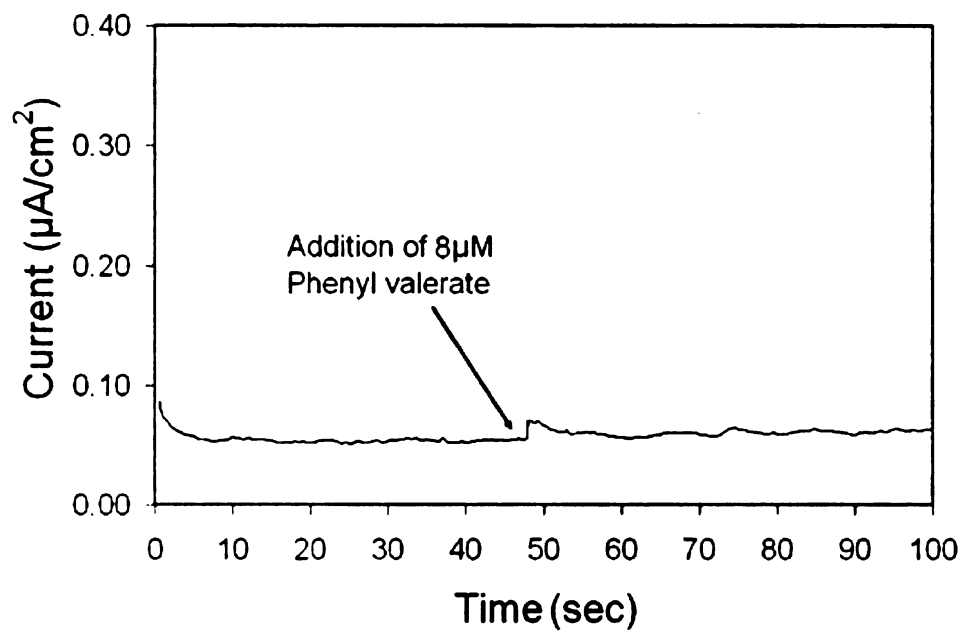
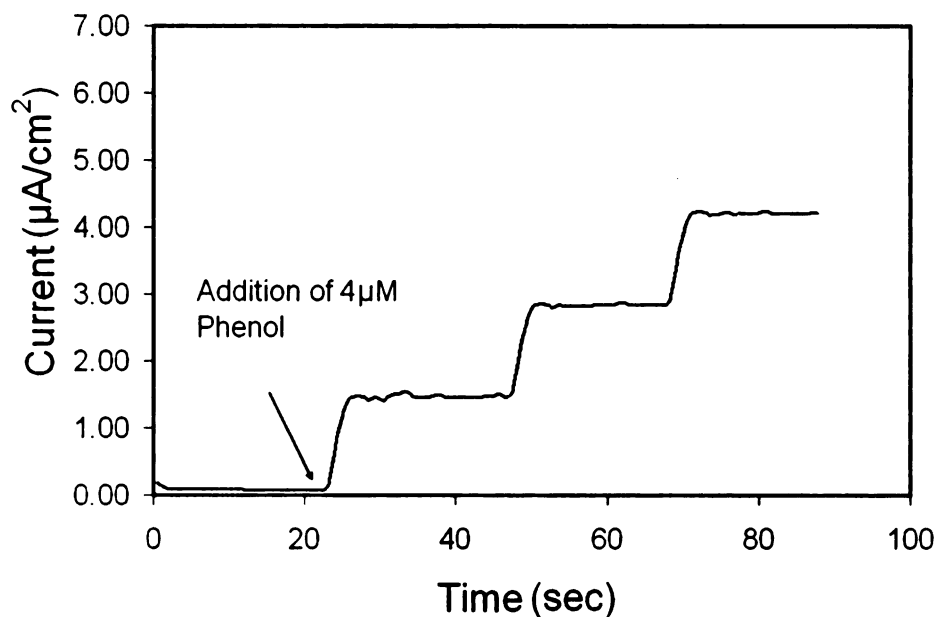
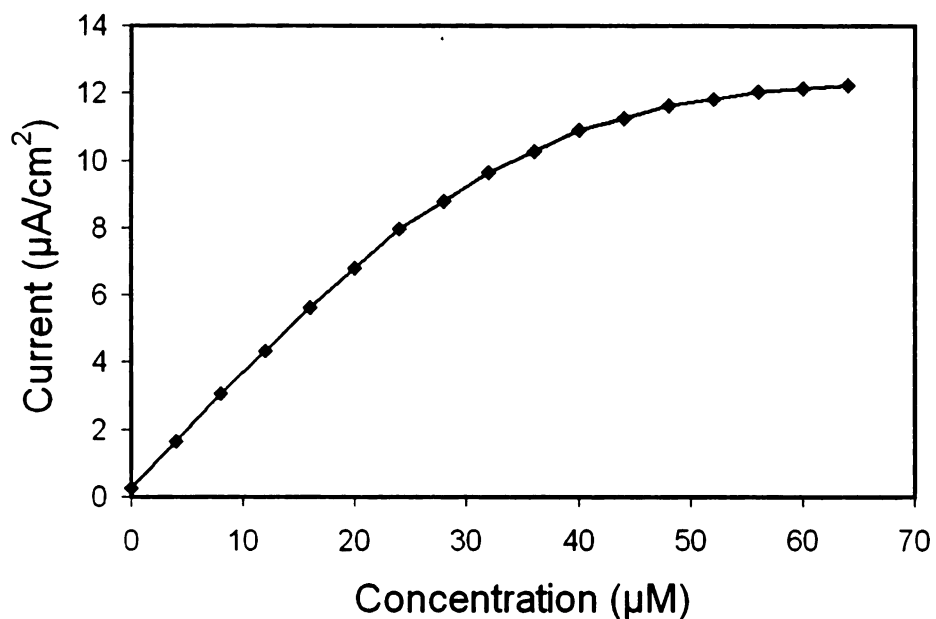


Figure 2.6: Control experiment: Current time response on an electrode containing only tyrosinase. The electrode was assembled in exactly the same way as NEST biosensor, except that the final NEST layer was not deposited.

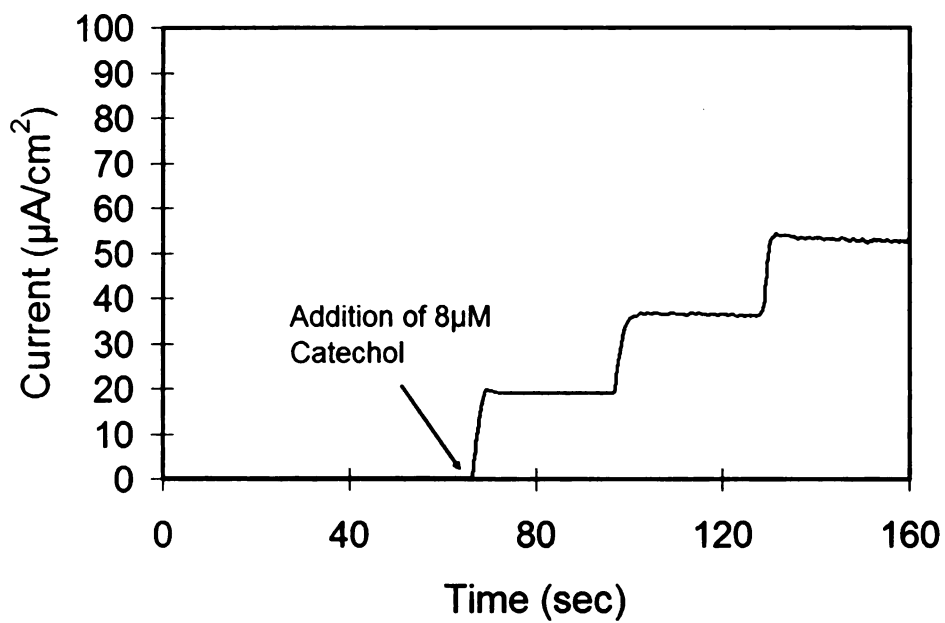


(a)

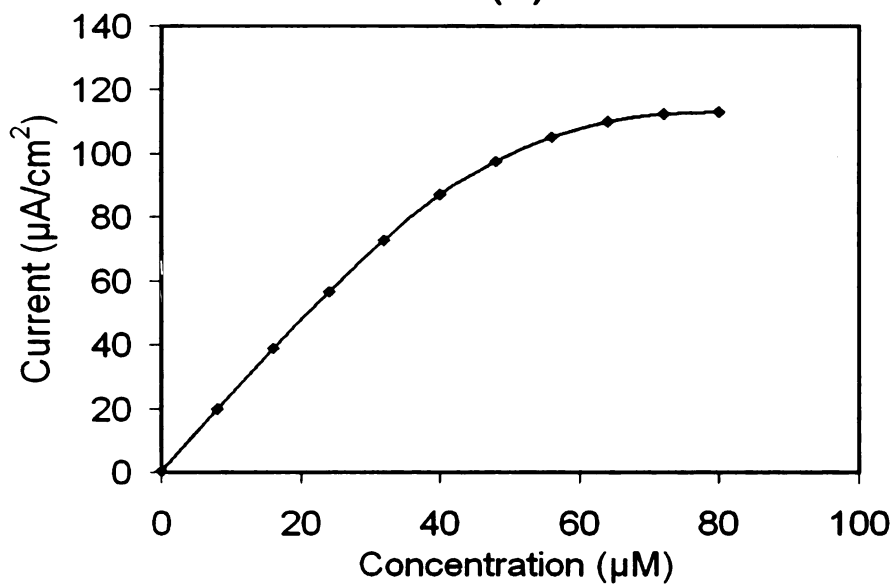


(b)

Figure 2.7: (a) Current time response of the NEST biosensor to the addition of aliquots of phenol in 0.1 M phosphate buffer (pH 7.0) to obtain final phenol concentrations as increments of 4 μM , at an applied potential of -0.1 V (vs Ag/AgCl). (b) Representative example of a calibration plot.



(a)



(b)

Figure 2.8: (a) Current time response of the NEST biosensor to the addition of aliquots of catechol in 0.1 M phosphate buffer (pH 7.0) to obtain final catechol concentrations as increments of 8 μM , at an applied potential of -0.1 V (vs Ag/AgCl). (b) Representative example of a calibration plot.

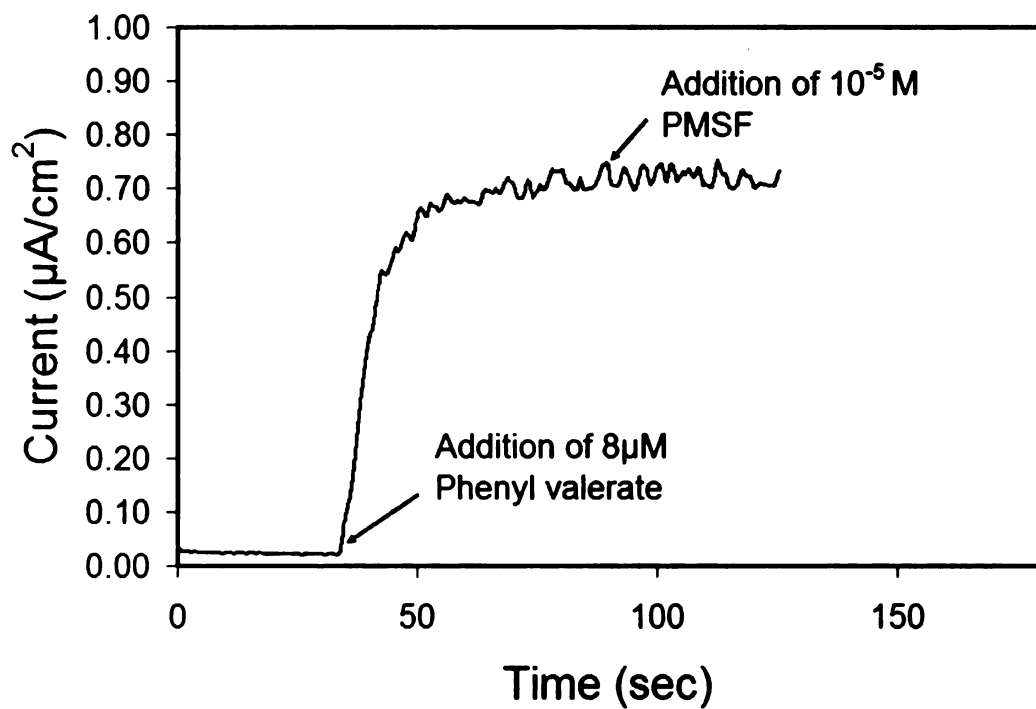


Figure 2.9: Current time response of NEST biosensor to the addition of phenyl valerate in phosphate buffer (0.1 M, pH 7.0) to obtain a final phenyl valerate concentration of 8 μM followed by the addition of NEST inhibitor PMSF to obtain a final PMSF concentration of 10 μM .

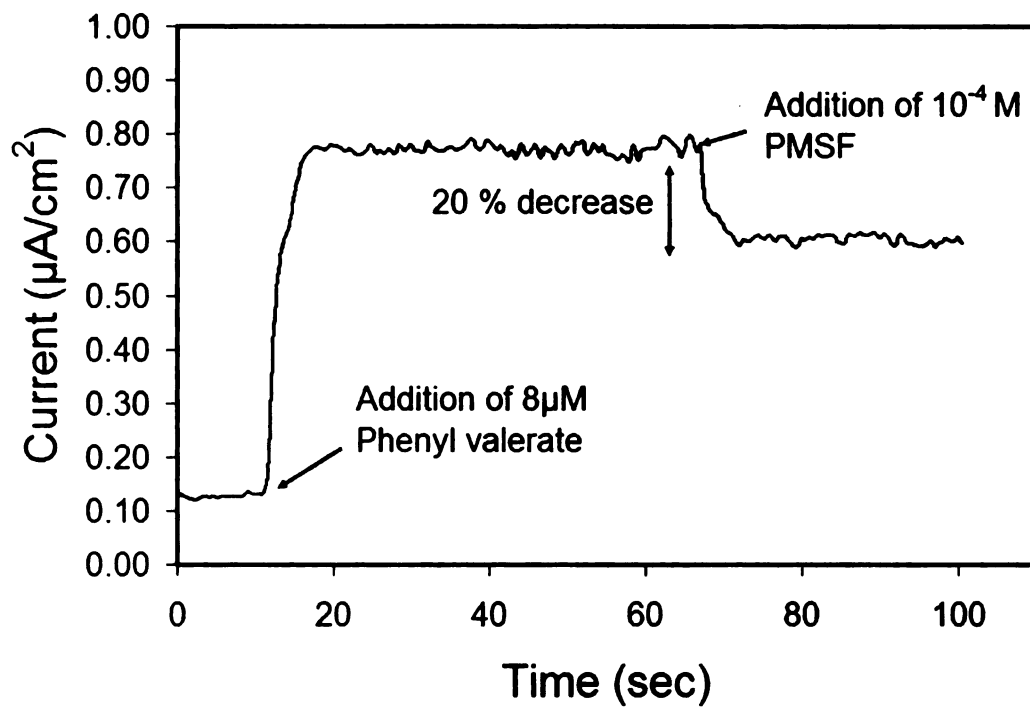


Figure 2.10: Current time response of NEST biosensor to the addition of phenyl valerate in phosphate buffer (0.1 M, pH 7.0) to obtain a final phenyl valerate concentration of 8 μM followed by the addition of NEST inhibitor PMSF to obtain a final PMSF concentration of 100 μM .

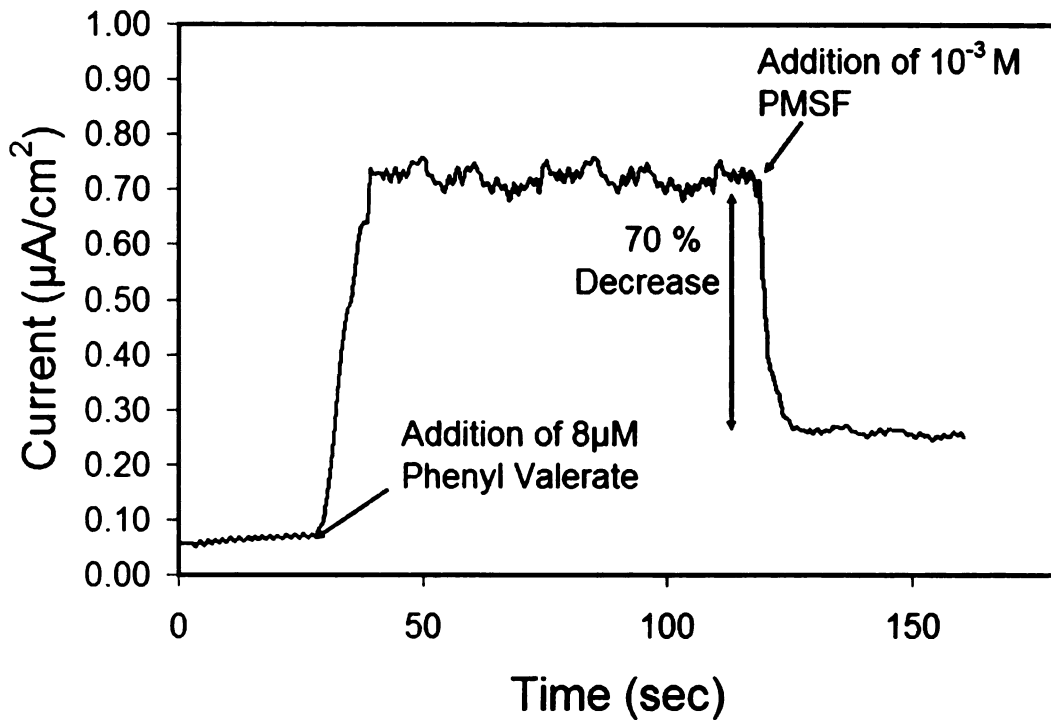


Figure 2.11: Current time response of NEST biosensor to the addition of phenyl valerate in phosphate buffer (0.1 M , pH 7.0) to obtain a final phenyl valerate concentration of 8 μM followed by the addition of NEST inhibitor PMSF to obtain a final PMSF concentration of 1000 μM .

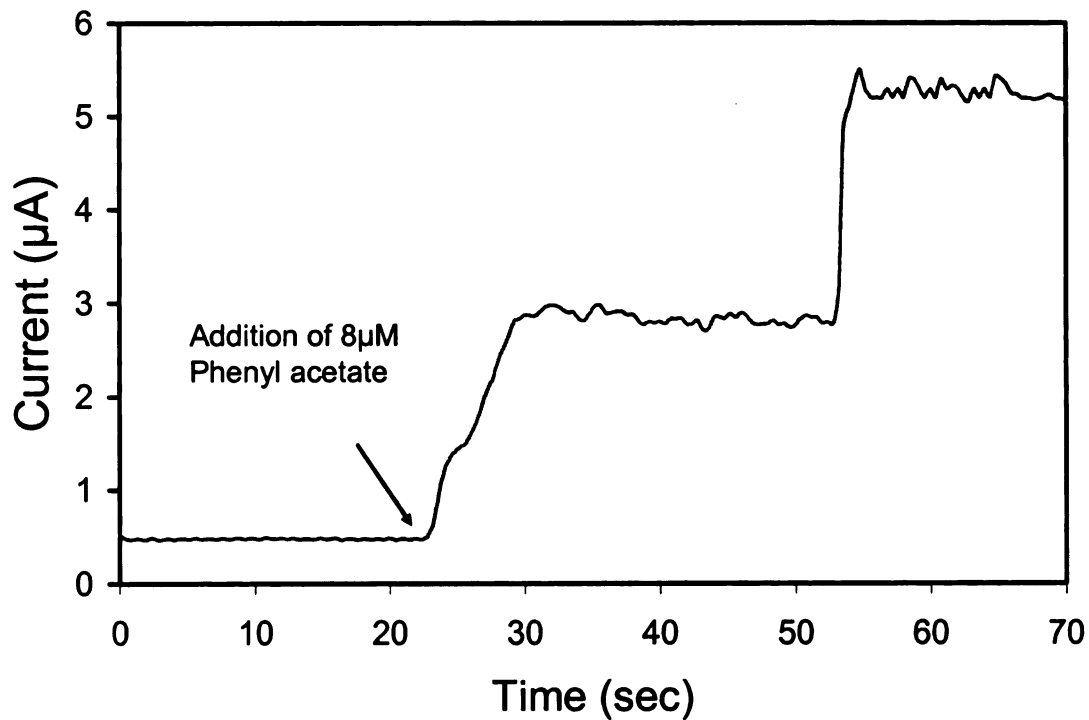


Figure 2.12: Current time response of a bi-enzyme electrode consisting of tyrosinase and AChE to the addition of aliquots of phenyl acetate to obtain final phenyl acetate concentrations as increments of $8 \mu\text{M}$, in 0.1 M phosphate buffer, $\text{pH } 7.0$, at an applied potential of -0.1 V (vs Ag/AgCl).

Table 2-1: Performance of bi-enzyme electrodes containing tyrosinase and different esterases. Phenyl valerate gave the highest current sensitivity for bi-enzyme electrodes containing tyrosinase and NEST, and also for bi-enzyme electrodes containing tyrosinase and Butyrylcholinesterase. Phenyl acetate gave the highest sensitivity for bi-enzyme electrodes containing tyrosinase and Acetylcholinesterase.

Enzyme	Substrate used	Average sensitivity ($\text{nA}\mu\text{M}^{-1}\text{cm}^{-2}$)
NEST	Phenyl valerate	87 ± 8
Acetylcholinesterase	Phenyl acetate	180 ± 25
Butyrylcholinesterase	Phenyl valerate	25 ± 10

3 HIGHLY SENSITIVE PHENOL SENSOR BASED ON LAYER-BY-LAYER ASSEMBLY

3.1 ABSTRACT

Phenols can be toxic even in low concentrations. The sensing of phenolic compounds is therefore essential to evaluate the health risk of environmental samples. Interestingly, we found that nanostructured thin films, consisting of bilayers of PLL and tyrosinase on a gold electrode, can also be used as highly sensitive sensors for detecting phenols. The films were deposited using layer by layer assembly approach and characterized using ellipsometry, Fourier transform infrared spectroscopy (FTIR), and constant potential amperometry. The current response of the films to catechol and phenol was found to be linear up to 6 bilayers. The increase in current sensitivity for catechol with each PLL-Tyr bilayer was approximately $(1.18 \pm 0.15) \mu\text{A}\mu\text{M}^{-1}\text{cm}^{-2}$ which is at least 2 orders of magnitude higher than that reported using other polyelectrolytes and tyrosinase multilayer systems, suggesting that the composition of polyelectrolytes may influence important factors such as enzyme loading and turnover number.

3.2 INTRODUCTION

Phenols are present in wastewaters and exhaust gases of many industries, including oil refineries, coke plants, resins and plastics, dyes and chemicals, and textiles (Karam and Nicell 1997). Phenols can be toxic even in low concentrations. They generally get adsorbed through skin and cause severe systemic reactions. The sensing of phenolic compounds is therefore essential to evaluate the health risk of environmental samples. Colorimetry, liquid and gas chromatography, and capillary electrophoresis are commonly used techniques for phenol determination (Townshend 1995; Vogel 1998). However, these techniques are time consuming, require special expertise on part of users, and have low sensitivity. Phenols can also be detected electrochemically by their direct oxidation at high overpotentials. However, this approach suffers from poor selectivity, due to interference by other electroactive compounds such as ascorbic acid.

To overcome these limitations, numerous biosensors based on immobilized tyrosinase have been proposed (Desprez and Labbe 1996; Ducey and Meyerhoff 1998; Kulkarni, Karve et al. 1998; Dall'Orto, Danilowicz et al. 1999; Wang, Lu et al. 2000; Ahn, Beaudette et al. 2001; Freire, Duran et al. 2002; Stanca, Popescu et al. 2003; Rajesh, Takashima et al. 2004; Solna, Sapelnikova et al. 2005; Solna and Skladal 2005). As mentioned in Chapter 2, tyrosinase is a copper containing enzyme that catalyzes the ortho-hydroxylation of monophenols (cresolase or monophenolase activity) to *o*-diphenols by oxygen and also catalyzes the oxidation of *o*-diphenols to *o*-quinones.

The underlying principle of most tyrosinase based biosensors is that the reaction product, *o*-quinone, is electrochemically active, and gets reduced at the electrode surface

at low potential, resulting in the generation of current. Moreover, the electroreduction of *o*-quinone produces catechol (*o*-diphenol) which again gets converted to *o*-quinone by tyrosinase. This recycling results in signal amplification; as a result higher sensitivity can be achieved in these sensors in comparison to conventional designs.

The current sensor systems are limited by the amount of protein immobilized on the electrode surface. The study of such electrodes has shown that the sensitivity of the sensor is proportional to the surface density of protein on the electrode surface (Forzani, Solis et al. 2000). Therefore, an increase in protein loading on the surface could promise a significant improvement in sensitivity. LBL assembly is a useful technique for increasing the protein content on the electrode surface. In this technique, a substrate is alternatively dipped in a polycationic and polyanionic solution leading to the formation of multilayered structures stabilized by electrostatic interactions. This technique has been used in the past for making alternating layers of tyrosinase, and polyelectrolytes such as poly(allylamine hydrochloride) (PAH) (Forzani, Solis et al. 2000; Coche-Guerente, Labbe et al. 2001; Forzani, Teijelo et al. 2003). However, the highest sensitivity obtained in these systems was approximately $0.005 \mu\text{A}\mu\text{M}^{-1}\text{cm}^{-2}$ for each tyrosinase and PAH bilayers.

The sensitivity of the sensors can further be increased by varying the composition of polyelectrolyte solution. As some polyelectrolyte composition may lead to enhanced protein loading or it may provide protein with a more native environment where it can exhibit higher turnover number. In this Chapter, the fabrication of multilayer films consisting of a polyelectrolyte poly-L-lysine (PLL) and tyrosinase is presented. The

resulting multilayer assemblies were characterized using ellipsometry, FTIR and ellipsometry. The current response of the films to catechol and phenol as a function of number of PLL-Tyr bilayers was studied up to 8 bilayers. The results of this study are unique in that the resulting PLL-Tyr multilayer films gave current sensitivity which is at least 2 orders of magnitude greater than those reported using other polyelectrolytes and tyrosinase multilayer systems (Forzani, Solis et al. 2000).

3.3 EXPERIMENTAL SECTION

3.3.1 Preparation of poly-L-lysine (PLL), and tyrosinase (Tyr) multilayer assemblies

Initially, the gold electrode was derivatized by dipping it in 5 mM solution of thioctic acid in ethanol for 30 min. The electrode was washed with ethanol, dried under nitrogen and dipped in PLL solution for 45 min. The PLL solution was prepared by dissolving 12 mg of PLL in 50 mL of 20 mM phosphate buffer (pH 8.5). The electrodes were then rinsed with water and dipped in a 0.2 mg/mL solution of Tyr for 1 h. The last two steps were repeated to create multiple PLL-Tyr bilayers. After the formation of PLL-Tyr bilayers, the electrodes were dipped in phosphate buffer (0.1 M, pH 7.0) for testing. All the experiments were done at room temperature.

3.3.2 Ellipsometry

Ellipsometric measurements were obtained with rotating analyzer ellipsometer (model M-44; J.A. Woollan Co. Inc., Lincoln, NE) using WVASE32 software. The thickness values for films were determined using 44 wavelengths between 414.0 and 736.1 nm. The angle of incidence was 75° for all experiments. Refractive indices of films containing

PLL and Tyr were assumed to be $n = 1.5$, $k=0$. These optical constants compare well with those determined for 4 PLL-Tyr bilayer films using ellipsometry.

3.3.3 Reflectance Fourier transform infrared spectroscopy

Reflectance FTIR spectroscopy was performed using a Nicolet Magna-IR 560 spectrometer containing a PIKE grazing angle (80°) attachment. The spectra were collected with 256 scans using a MCT detector.

3.3.4 Potential step amperometry

The electrodes (sensors) were maintained at a potential of -100 mV (vs Ag/AgCl reference electrode) using a BAS CV-50W electrochemical analyzer. To measure the response, a small aliquot of phenol or catechol was added to a beaker containing the sensor immersed in a stirred buffer solution, and the current was monitored.

3.4 RESULTS AND DISCUSSIONS

3.4.1 Ellipsometry and FTIR

Ellipsometry was used to provide proof for the assembly of the multilayers. Figure 3.1 shows the ellipsometric thicknesses in air for different number of PLL-Tyr bilayers. The thickness increase after the addition of each bilayer was 7.2 ± 0.4 nm, with the exception of the initial bilayer, which was 9.3 ± 0.4 nm thick. On the other hand, the reported thickness increase for PAH-Tyr bilayers was approximately 2.3 ± 0.3 nm (Forzani, Tejjelo et al. 2003).

Figure 3.2 shows the FTIR spectra of PLL-Tyr films containing up to 6 bilayers. The amide absorbances at 3297 cm^{-1} (amide A, due to N-H asymmetric and symmetric

stretching), 1665 cm^{-1} (amide I, due to the stretching mode of the carbonyl group coupled to the amide linkage), and 1540 cm^{-1} (amide II, due to the N-H in-plane bending of the polypeptide chains), dominates the spectrum of PLL-Tyr films. These peaks compare well with the published FTIR spectrum of tyrosinase in solid state (KBr pellet), where amide A peak was observed at 3295 cm^{-1} , amide I at 1653 cm^{-1} , and amide II at 1541 cm^{-1} . Negative shifts of amide band frequencies in relation to the native state are generally found in denatured proteins, because of mass loss due to decrease in the number of hydrogen bonds (Forzani, Teijelo et al. 2003). Although most of the tyrosinase amide bands appeared at the same frequency as that in the solid-state, the positive shifts of amide I band could be associated with a more structured protein. FTIR also confirmed the step-wise growth of PLL-Tyr films, as the absorbance values approximately increased linearly (Figure 3.1) with the number of bilayers, confirming the ellipsometric data.

3.4.2 Dependence of current response on working potential and pH

The various experimental parameters that can affect the amperometric determination of catechol (such as pH and applied potential) were optimized using the procedure outlined in Chapter 2. The optimum current sensitivity (highest signal to background ratio) was obtained at -0.1 V and $\text{pH} = 7$.

3.4.3 Amperometric response to catechol and phenol

Figure 3.3a displays a typical current-time response under the optimal experimental conditions for a gold electrode containing 6 PLL-Tyr bilayers after the successive addition of aliquots of catechol. A well defined reduction current, proportional to the amount of catechol was observed. The response time of the electrode was less than

20 s, due to the nano-scale thickness of the interface. The response to catechol was linear ($R^2 = 0.989$) in the range 5 nM to 40 μM and it reached saturation at approximately 85 μM (Figure 3.3b). The limit of detection was 5 nM at a signal-to-noise ratio of 3. The reproducibility of the sensor was investigated at a catechol concentration of 8 μM ; the mean current was approximately $57 \mu\text{Acm}^{-2}$, with a standard deviation of approximately 8%. Similarly, the response of this sensor (containing 6 PLL-Tyr bilayers) to phenol was also studied. The response to phenol was linear ($R^2 = 0.990$) in the range 1 to 25 μM , with an average sensitivity of approximately $1.2 (\pm 0.15) \mu\text{A}\mu\text{M}^{-1}\text{cm}^{-2}$, and it reached saturation at approximately 70 μM .

3.4.4 Effect of number of PLL-Tyr bilayers

Figure 3.4 shows the current sensitivity to catechol as a function of PLL-Tyr bilayers. The increase in current sensitivity was approximately linear up to 6 bilayers and it reached saturation at around 8 bilayers. The increase in current sensitivity in the linear region with each bilayer (with the exception of first bilayer where it was $1.4 \pm 0.1 \mu\text{A}\mu\text{M}^{-1}\text{cm}^{-2}$) was approximately $1.18 \pm 0.15 \mu\text{A}\mu\text{M}^{-1}\text{cm}^{-2}$. The current sensitivity corresponding to 6 PLL-Tyr bilayers was $7.1 \pm 0.55 \mu\text{A}\mu\text{M}^{-1}\text{cm}^{-2}$. Similarly, the increase in sensitivity to phenol was also found to be linear and equal to $0.2 \pm 0.02 \mu\text{A}\mu\text{M}^{-1}\text{cm}^{-2}$ for each bilayer.

3.4.5 Cyclic voltammetry

While constant potential amperometry was the primary sensing technique used in this study, other sensing techniques such as cyclic voltammetry were also tried. Figure

3.5a shows the cyclic voltammograms of the enzyme electrodes (containing 2 PLL-Tyr bilayers) at different concentrations of catechol. The electrocatalytic cathodic current indicates the effective reduction of *o*-quinone. For all catechol concentrations, the reduction current begins at 0.18 V and then reaches saturation at higher negative potentials. As expected, the reductive current was found to increase linearly with catechol concentration and then it levels off at a catechol concentration of approximately 85 μM (Figure 3.5b).

3.4.6 Discussions

The ellipsometric thickness increase after the addition of each PLL-Tyr bilayer was approx. 7.2 nm which is about three times higher than that reported for PAH-Tyr bilayers (2.3 nm). The current sensitivity obtained in the PLL-Tyr system for each bilayer was approximately $1.18 \pm 0.15 \mu\text{A}\mu\text{M}^{-1}\text{cm}^{-2}$, which is more than 2 orders of magnitude higher than that reported for PAH-Tyr bilayers (Forzani, Solis et al. 2000). Using a theoretical analysis, Forzani et al (Forzani, Solis et al. 2000) have shown that the current sensitivity in layered tyrosinase-polyelectrolyte system is directly proportional to the surface coverage (i.e mol/cm^2) of the enzyme and its turnover number. If the enzyme density (i.e mol/cm^3) is assumed to be the same in both PAH-Tyr and PLL-Tyr system, then the ellipsometric data suggests that the enzyme surface coverage in PLL-Tyr bilayers is approximately three times higher than that in PAH-Tyr bilayers. However, this three times increase in enzyme surface coverage alone cannot explain more than 2 orders of magnitude increase in current sensitivity observed with PLL-Tyr bilayers, and it suggests that other factors such as higher turnover number or different enzyme density

may be responsible for increased sensitivity. It is possible that PLL-Tyr bilayers may provide tyrosinase with a more natural environment where it may be in a more native conformation and thus exhibits higher turnover number, or PLL-Tyr bilayers may have a different enzyme density than PAH-Tyr bilayers.

3.5 CONCLUSIONS

An approach to develop highly sensitive phenol sensors is presented. Layer by layer assembly approach was used to deposit PLL-Tyr bilayers on a thioctic acid derivatized gold electrode. Ellipsometry and FTIR provided strong evidence of bilayer assembly. The current sensitivity to catechol and phenol was found to increase linearly up to 6 PLL-Tyr bilayers. The increase in sensitivity corresponding to catechol and phenol was $1.18 \mu\text{A}\mu\text{M}^{-1}\text{cm}^{-2}$ and $0.2 \mu\text{A}\mu\text{M}^{-1}\text{cm}^{-2}$, respectively. This value is at least two orders of magnitude greater than that reported using other polyelectrolyte-tyrosinase systems, suggesting that the composition of polyelectrolytes may influence important factors such as enzyme loading, density, and turnover number.

3.6 RECOMMENDATIONS FOR FUTURE WORK

Because the entire interface used in this study can be assembled using layer by layer assembly from different solutions, it may be possible to assemble this interface inside microfluidics channels, and study the effect of different parameters such as shear rate on the stability on the sensor.

Nanosized functional particles represent an area of great research interest. In the field of biosensors and biocatalysis, nanosized materials offer the potential for extremely

high surface area to volume ratio, thus allowing immobilization of large amounts of biomolecules per unit projected area. Carbon nanoparticles, such as fullerenes, carbon nanotubes (CNTs), and exfoliated graphite nanoplatelets (xGnPs), provide high conductivity and surface area without excessive diffusional resistance. These nanoparticles are widely used to prepare solid electrode systems and supporting substrates in electrochemical biosensors, due to their high chemical inertness and wide range of working potentials with low electrical resistance. Therefore, it will be interesting to study the effect of addition of these nanoparticles on the sensitivity of PLL-Tyr bilayers. It is possible that addition of these nanoparticles may lead to higher sensitivity either due to lower diffusional resistance, or increased enzyme loading and higher turnover number.

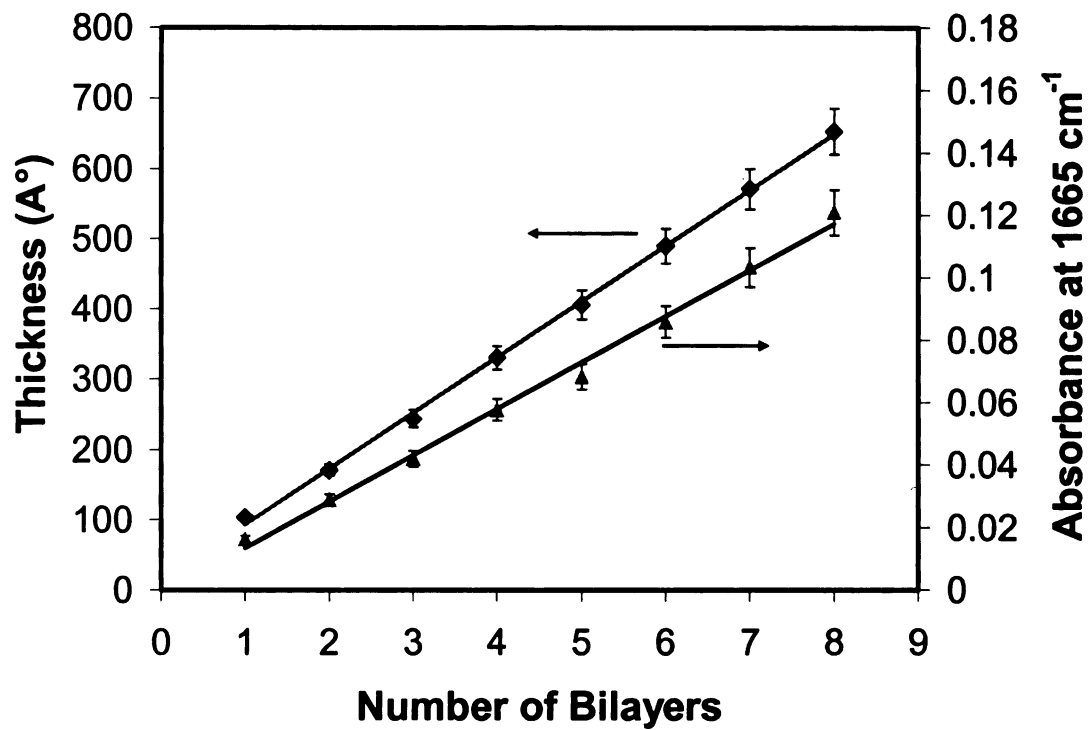


Figure 3.1: Ellipsometric thickness and FTIR absorbances at 1665 cm⁻¹ for PLL-Tyr multilayered films.

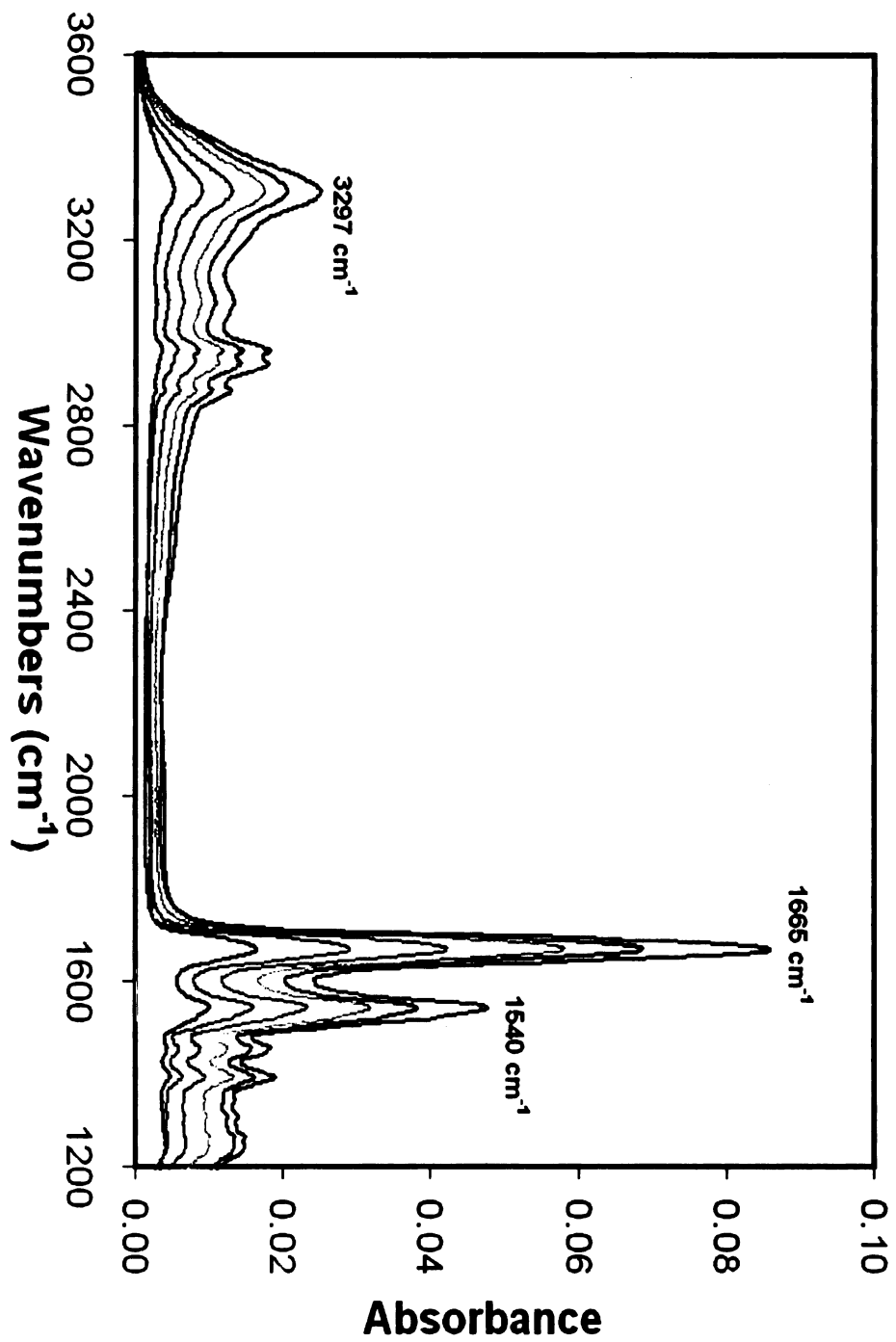
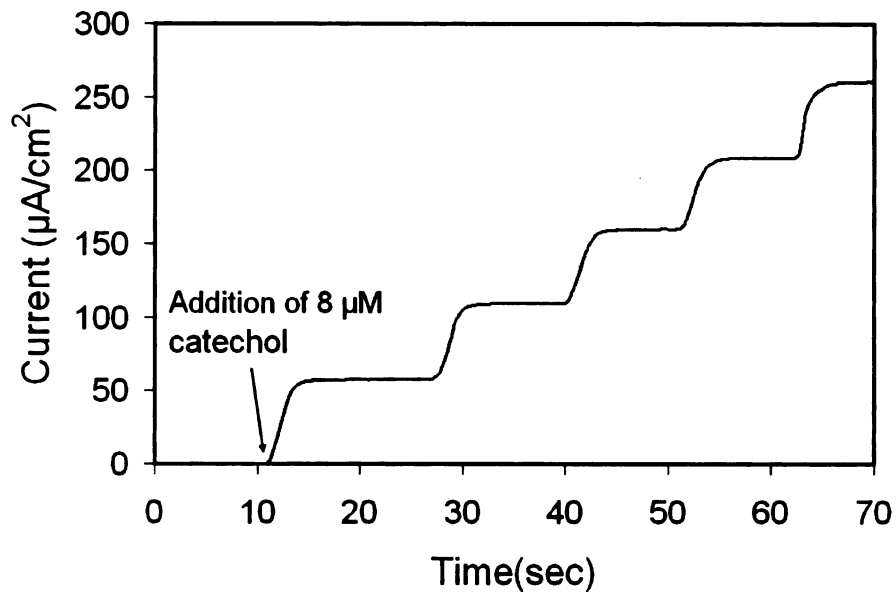
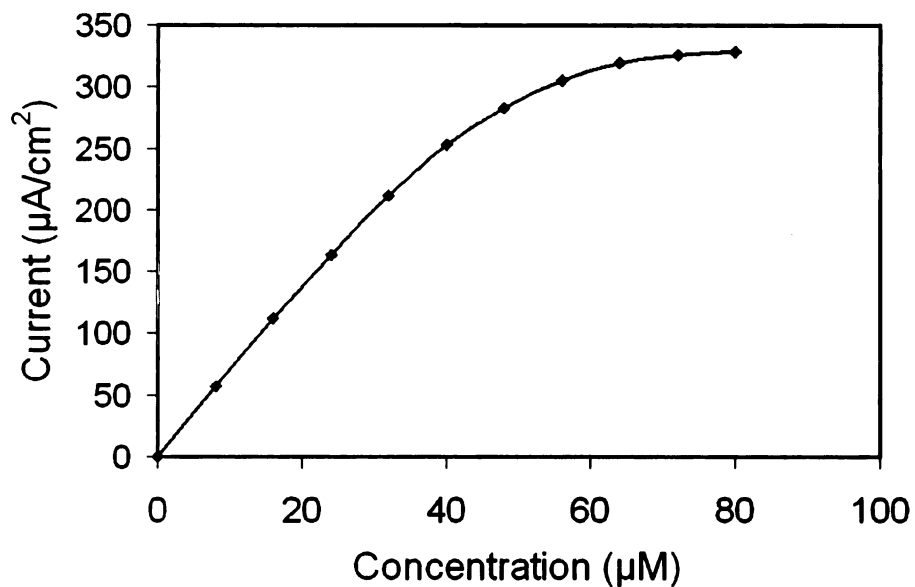


Figure 3.2: FTIR spectra of PLL-Tyr films composed of up to 6 bilayers.



(a)



(b)

Figure 3.3 (a) Current time response of the gold electrode containing 6 PLL-Tyr bilayers to the addition of aliquots of 8 μM catechol in 0.1 M phosphate buffer, pH 7.0 at an applied potential of -0.1 V (vs Ag/AgCl). (b) Calibration plot.

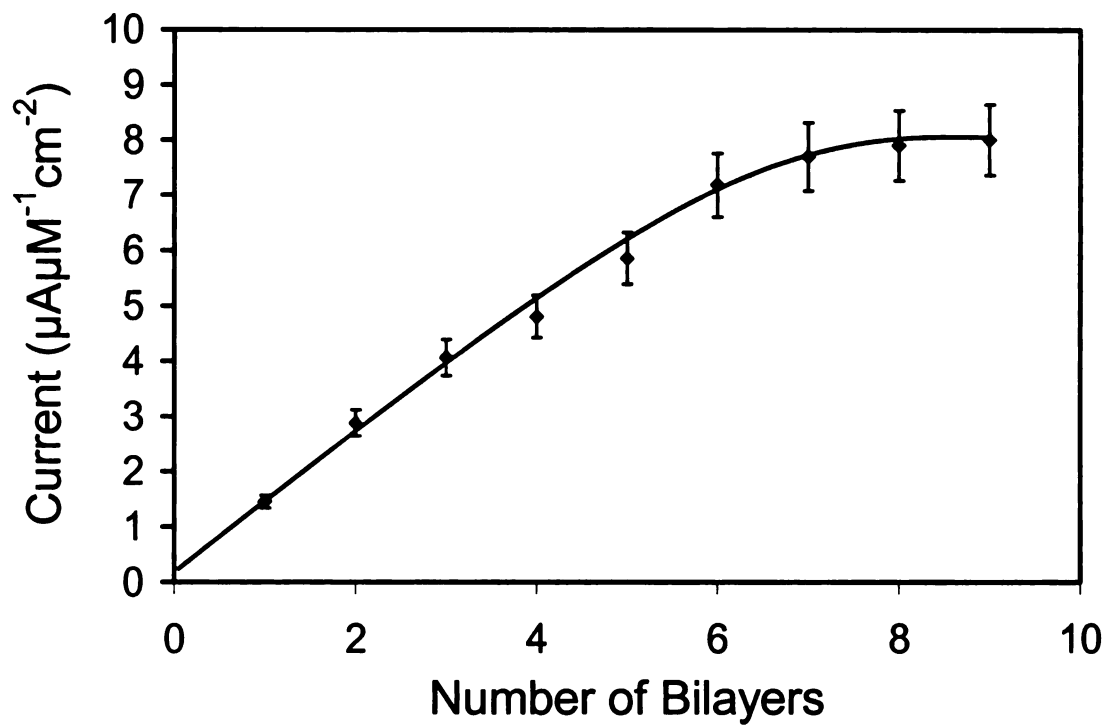


Figure 3.4: Effect of number of PLL-Tyr bilayers on the current sensitivity of the enzyme electrode to catechol.

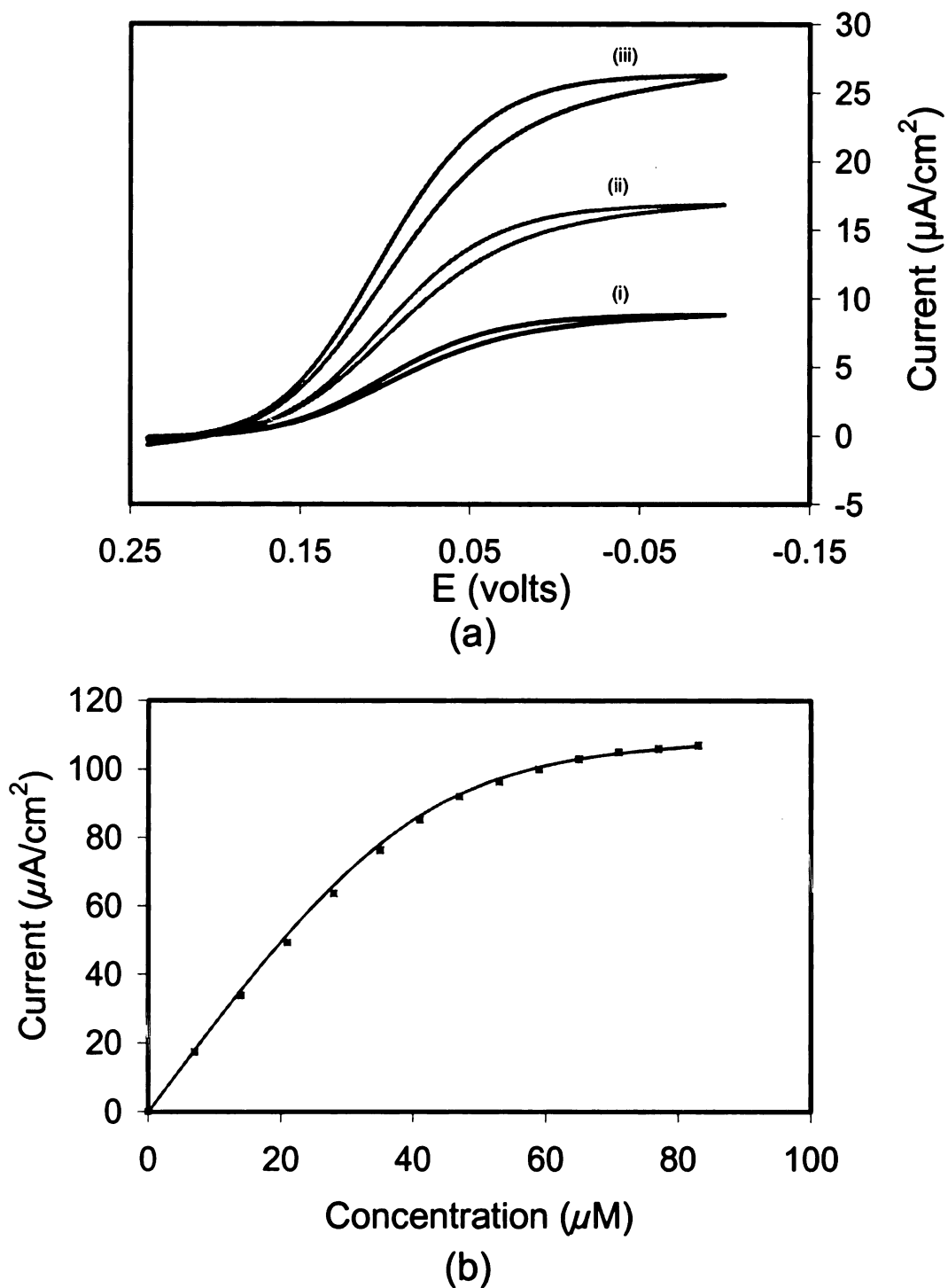


Figure 3.5: (a) Cyclic voltammograms of the enzyme electrode containing 2 PLL-Tyr bilayers, in the presence of different concentrations of catechol: (i) 3.5 μM , (ii) 7 μM , and (iii) 10.5 μM . (b) Representative example of a calibration plot. All the measurements were performed in 0.1 M phosphate buffer, pH 7.0, and scan rate of 100 mVs^{-1} .

4 THEORETICAL AND EXPERIMENTAL STUDY OF BI-ENZYME ELECTRODES WITH SUBSTRATE RECYCLING

4.1 ABSTRACT

The range of analytes for which biosensors can be developed can be increased substantially by coupling multiple enzyme activities into reaction pathways. The sensitivity of the biosensors can also be increased dramatically (or amplified) by incorporating a substrate recycling scheme. For low concentrations of substrate, this chapter presents a theoretical model for a bi-enzyme biosensor that achieves signal amplification via substrate recycling. The bi-enzyme electrode was fabricated by co-immobilizing two enzymes: Tyr and NEST. The model was validated by assembling the bi-enzyme interface on a rotating disk electrode and measuring the biosensor's response to phenyl valerate under varying rotating speeds. The model can help quantify the influence of mass transport, partition coefficients, enzyme, and electron-transfer kinetics on the metrological characteristics of the bi-enzyme electrode. This information can help optimize the performance of biosensors that use substrate recycling.

4.2 INTRODUCTION

Biosensors based on enzymes are becoming popular in various fields of analytical chemistry because of their high selectivity, specificity and low cost for mass production. In particular, enzyme electrodes have been developed for many applications such as electrochemical immunoassays, monitoring of metabolites, and detection of water and air pollutants (Uchiyama, Hasebe et al. 1993; Rajesh, Takashima et al. 2004; Solna and Skladal 2005).

The range of analytes for which reporting interfaces (biosensors) can be developed can be increased substantially by coupling multiple enzyme activities into reaction pathways. For example, NEST biosensor (described in Chapter 2), couples NEST esterase activity with two tyrosinase oxidation activities: cresolase activity and catecholase activity, resulting in electrochemical detection of phenyl valerate.

The sensitivity of the reporting interfaces can be increased substantially by incorporating a substrate recycling scheme. In these devices, an analyte that is oxidized or reduced at the electrode is electrochemically recycled so that it can interact with the electrode more than once, thus amplifying the electrode's signal. The shuttle analyte can either be the analyte of interest (the enzyme's substrate) or a compound that is produced by an additional enzyme reaction. Amplification by substrate recycling has been achieved by several mechanisms. One uses a chemical reaction to regenerate the enzyme's substrate (Uchiyama, Hasebe et al. 1993). Another uses a second enzymatic reaction, which converts the enzyme's product back to the substrate. In these two mechanisms, transduction is achieved by monitoring the production of a coproduct or the consumption of a co-substrate (Bauer, Eremenko et al. 1996). A third mechanism is based on electrochemically recycling the reaction product back to the substrate (Coche-Guerente, Labbe et al. 1999). In the latter case, substrate recycling is achieved by the amperometric transduction step.

Mathematical models can be used to analyze the simultaneous mass transfer and reaction steps that occur in biosensors that use substrate recycling in order to improve their metrological characteristics. Such a theoretical analysis can help elucidate the rate-limiting step(s) and evaluate the performance characteristics of substrate-recycling

biosensors. In work relevant to the NEST biosensor, Gorton et al.(Burestedt, Narvaez et al. 1996) theoretically considered and experimentally demonstrated the various rate limiting steps for tyrosinase enzyme modified electrodes with substrate recycling. This model assumed that diffusional resistance within the enzyme layer was negligible. Coche-Guérente et al., in a series of papers, presented a theoretical model for an immobilized enzyme layer with electrochemical substrate-recycling scheme (Coche-Guerente, Labbe et al. 1999; Coche-Guerente, Labbe et al. 2001). This model, which was applied to tyrosinase modified electrodes, includes the influence of diffusion, partition coefficient, enzyme, and electron-transfer kinetics. However, these theoretical analyses have been limited to single enzyme electrodes and are thus not suitable for bi-enzyme electrodes such as the NEST biosensor.

In this Chapter, a theoretical model is presented for a bi-enzyme rotating disk electrode consisting of NEST and tyrosinase. The molecular architecture of the bi-enzyme electrode is shown in Figure 4.1. The NEST protein converts phenyl valerate to phenol, which is converted to *o*-quinone by tyrosinase. The *o*-quinone is electrochemically reduced to catechol at the electrode's surface, resulting in current. A portion of the catechol produced is then converted to *o*-quinone by tyrosinase. Catechol thus serves as shuttle analyte that can undergo successive cycles of enzymatic oxidation-electrochemical reduction (substrate recycling), resulting in an amplification of biosensor's response.

The NEST biosensor model includes the influence of the mass transport, permeation through the enzyme layers and enzyme kinetics. This model is expressed in dimensionless form to minimize the number of constants that must be evaluated. The

biosensor was assembled on a rotating disk electrode, and the biosensor's performance was measured at a variety of rotational velocities and substrate concentrations to evaluate the constants and validate the model.

4.3 EXPERIMENTAL SECTION

4.3.1 Materials

Thioctic acid, PLL (molecular weight $\sim 15,000$), tyrosinase, sodium phosphate (monobasic and dibasic), sodium chloride were obtained from Sigma (St. Louis, MO). Ultrapure water was supplied by a Nanopure-UV four-stage purifier (Barnstead International, Dubuque, IA); the purifier was equipped with a UV source and a final $0.2 \mu\text{m}$ filter.

4.3.2 Preparation of gold electrode

The molecular architecture of the biosensor is shown schematically in Figure 4.1. Gold rotating disk electrodes (Metrohm Limited, Herisau, Switzerland) were polished with alumina powder and dipped in 5 mM solution of thioctic acid in ethanol for 30 min. The electrodes were washed with ethanol, dried under nitrogen and dipped in PLL solution for 45 min. The PLL solution was prepared by adding 12 mg of poly-lysine in 50 ml of 20 mM phosphate buffer (pH 8.5). The electrodes were then rinsed with water and dipped in equimolar solution of tyrosinase and NEST in 0.1 M phosphate buffer for 45 min. The last two steps were repeated 3 times to create 3 bilayers of PLL and tyrosinase/NEST. The electrodes were then washed with water, dried under nitrogen and dipped in phosphate buffer (0.1 M, pH 7.0) for testing. All the experiments were done at room temperature.

4.3.3 Chronoamperometry and other measurements

The bi-enzyme rotating disk electrodes containing NEST and tyrosinase were maintained at a potential of -100 mV (vs Ag/AgCl reference electrode) using a CHI 660B electrochemical analyzer (CH instruments, Austin, TX). To perform electrochemical measurements, the bi-enzyme rotating disk electrodes (area = 0.07 cm²) were dipped in 0.1 M phosphate buffer (pH 7.0), and small aliquots of phenyl valerate, phenol or catechol solution were added. The steady state current was then measured at different rotating speeds. Ellipsometric measurements were done using a WVASE 32 (J.A. Woollam Co. Inc., Lincoln, NE) ellipsometer. The angle of incidence was 75° for all experiments. The refractive indices of films were assumed to be n = 1.5, k=0.

4.4 THEORETICAL MODEL

4.4.1 Enzyme kinetics

Tyrosinase is a binuclear copper containing enzyme that catalyzes the oxidation of catechols to *o*-quinone (catecholase activity). For catechol as the substrate, it has been reported (Coche-Guerente, Labbe et al. 1999) that the overall rate (v) in solution can be described by Michaelis-Menten formalism (Equation 4.1) with an apparent Michaelis constant $K_m^{app} = 220 \mu\text{M}$.

$$v = \frac{k_{cat}[E_t][S]}{K_m^{app} + S} \quad (4.1)$$

where E_t , S and k_{cat} represent the enzyme concentration, catechol concentration and turnover number, respectively.

Since, the experiments conducted in the present study involve substrate concentrations around two orders of magnitude less than K_m^{app} , the kinetics can be assumed to be first order relative to the substrate concentration.

Besides its catecholase activity, tyrosinase is also able to catalyze ortho-hydroxylation (monophenolase activity) of monophenols to *o*-diphenols (catechols) that, in turn, are oxidized to corresponding *o*-quinones (catecholase activity). Because the hydroxylation activity of tyrosinase is expressed in conjunction with oxidation of *o*-diphenol to its *o*-quinone, some authors have defined monophenolase activity as the complete conversion of monophenols to *o*-quinone. Indeed, the hydroxylation step proceeds and has been shown to be much slower than the oxidation of *o*-diphenol to *o*-quinone and is therefore considered to be the rate limiting step (Coche-Guerente, Labbe et al. 2001). The enzymatic oxidation of phenol to *o*-quinone has also been shown to follow Michaelis-Menten formalism (Coche-Guerente, Labbe et al. 2001), with an apparent K_m^{app} of 250 μ M in homogeneous solution.

Similarly, the esterase activity of NTE (or NEST) can convert phenyl valerate to phenol, and this reaction also follows Michaelis-Menten formalism, with an apparent K_m^{app} of approximately 1.4 mM in homogeneous solution.

4.4.2 Assumptions

Figure 4.2 is a schematic representation of a bi-enzyme rotating disk electrode, modified with an enzyme layer that contains NEST and tyrosinase, and has a thickness L . The sequential steps that lead to an electrochemical signal in the presence of phenyl valerate substrate S_1 are as follows:

(1) Mass transfer of phenyl valerate (S_1), phenol (S_2), catechol (S_3), and quinone (Q_4)

through a stagnant film between the bulk and the enzyme layer. For rotating disk electrode, this film has a thickness $\delta = 1.61D_e^{1/3}\nu^{1/6}\omega^{-1/2}$ (Coche-Guerente, Labbe et al. 1999), where D_e , ν and ω represent the diffusion coefficient, kinematic viscosity and rotation speed, respectively. For simplicity, the diffusion coefficients of S_1 , S_2 , S_3 and Q_4 in the bulk aqueous phase and stagnant film were assumed to be identical (D_e).

(2) Partitioning of S_1 , S_2 , S_3 and Q_4 from the stagnant film into the enzyme layer. The

kinetics of partitioning were assumed to be rapid so that the interfacial concentrations in the film and enzyme layers remained at equilibrium. The partition coefficients (k_p) were assumed to be identical for S_1 , S_2 , S_3 and Q_4 . Thus, yielding the following equilibrium expressions.

$$[S_1]_{L-} = k_p[S_1]_{L+} \quad (4.2)$$

$$[S_2]_{L-} = k_p[S_2]_{L+} \quad (4.3)$$

$$[S_3]_{L^-} = k_p[S_3]_{L^+} \quad (4.4)$$

$$[Q_4]_{L^-} = k_p[Q_4]_{L^+} \quad (4.5)$$

(3) Diffusion of S_1 , S_2 , S_3 and Q_4 within the enzymatic layer of thickness L . The enzymatic layer was assumed to behave like a semi-permeable membrane. The model was simplified by assuming an identical diffusion coefficient (D_j) for S_1 , S_2 , S_3 and Q_4 .

(4) At steady state conditions, all the substrates S_1 , S_2 , S_3 and Q_4 are present in the enzymatic layer, although only S_1 is present in the bulk solution. Inside the enzyme layer, for low concentrations of phenyl valerate, the conversion of phenyl valerate (S_1) to phenol can be given by the following first order equation:

$$v_1 = \frac{k_1[E_1][S_1]}{K_1} \quad (4.6)$$

where E_1 denotes the total concentration of active NEST, and K_1 is the apparent K_m value. The rate of conversion of phenol to *o*-quinone and catechol to *o*-quinone has been shown to be given by similar first order expressions (Coche-Guerente, Labbe et al. 1999) (Coche-Guerente, Labbe et al. 2001):

$$v_2 = \frac{k_2[E_2][S_2]}{K_2} \quad (4.7)$$

$$v_3 = \frac{k_3[E_3][S_3]}{K_3} \quad (4.8)$$

Where, E_2 and E_3 represent the concentrations of monophenolase and catecholase active sites, respectively.

(5) Electrode potential was assumed to be sufficiently negative so that the electrochemical reduction step is not rate limiting.

4.4.3 Model equations

Using the same approach as the one already reported in a theoretical treatment of biosensors (Bartlett and Whitaker 1987; Coche-Guerente, Labbe et al. 1999; Coche-Guerente, Labbe et al. 2001), the equations describing the concentrations of S_1 , S_2 , S_3 and Q_4 at steady state are as follows:

$$\frac{\partial^2 S_1}{\partial x^2} - \frac{S_1}{\lambda_1^2} = 0 \quad (4.9)$$

$$\frac{\partial^2 S_2}{\partial x^2} - \frac{S_2}{\lambda_2^2} + \frac{S_1}{\lambda_1^2} = 0 \quad (4.10)$$

$$\frac{\partial^2 S_3}{\partial x^2} - \frac{S_3}{\lambda_3^2} = 0 \quad (4.11)$$

$$\frac{\partial^2 Q_4}{\partial x^2} + \frac{S_2}{\lambda_2^2} + \frac{S_3}{\lambda_3^2} = 0 \quad (4.12)$$

where x is the distance from electrode surface. As defined below, λ_1 , λ_2 and λ_3 represent the reaction lengths (Coche-Guerente, Labbe et al. 1999) related to phenyl valerate (S_1), phenol (S_2), and catechol (S_3):

$$\lambda_1 = \left(\frac{D_f K_1}{k_1 E_1}\right)^{\frac{1}{2}} \quad \lambda_2 = \left(\frac{D_f K_2}{k_2 E_2}\right)^{\frac{1}{2}} \quad \lambda_3 = \left(\frac{D_f K_3}{k_3 E_3}\right)^{\frac{1}{2}} \quad (4.13)$$

4.4.4 Boundary conditions

To determine concentration profiles within the enzyme layer, equations 4.9-4.12 were solved with the following boundary conditions:

- 1) Applied potential is sufficiently negative that

$$[Q_4]_{x=0} = 0 \quad (4.14)$$

- 2) Since phenyl valerate and phenol are not electro-active

$$\left[\frac{\partial S_1}{\partial x}\right]_{x=0} = 0, \quad \left[\frac{\partial S_2}{\partial x}\right]_{x=0} = 0 \quad (4.15)$$

- 3) Only phenyl valerate is present in the bulk

$$[S_1]_{x=\infty} = S_1(\infty), [S_2]_{x=\infty} = 0, [S_3]_{x=\infty} = 0, [Q_4]_{x=\infty} = 0 \quad (4.16)$$

- 4) At steady state, flux of phenyl valerate, phenol, catechol and quinone across the film equals that entering the enzyme layer.

$$D_f \left[\frac{\partial S_1}{\partial x} \right]_{x=L} = \frac{D_e}{k_p \delta} [k_p S_1(\infty) - [S_1]_{x=L}] \quad (4.17)$$

$$D_f \left[\frac{\partial S_2}{\partial x} \right]_{x=L} = -\frac{D_e}{k_p \delta} [S_2]_{x=L} \quad (4.18)$$

$$D_f \left[\frac{\partial S_3}{\partial x} \right]_{x=L} = -\frac{D_e}{k_p \delta} [S_3]_{x=L} \quad (4.19)$$

$$D_f \left[\frac{\partial Q_4}{\partial x} \right]_{x=L} = -\frac{D_e}{k_p \delta} [Q_4]_{x=L} \quad (4.20)$$

- 5) From law of conservation of mass, for any x inside the enzyme layer:

$$[Q_4] + [S_1] + [S_2] + [S_3] = k_p S_1(\infty) \quad (4.21)$$

$$6) \text{ Current density} = J = \frac{i}{A} = -nFD_f \left[\frac{\partial S_3}{\partial x} \right]_{x=0} = nFD_f \left[\frac{\partial Q_4}{\partial x} \right]_{x=0} \quad (4.22)$$

Solution of equations 4.9 to 4.12 gave the following analytical expressions for concentration profiles of S_1 , S_2 , S_3 and Q_4 . The following expressions were also confirmed by Matlab and Mathematica.

$$S_1 = \frac{k_p S_1(\infty)}{\frac{P_m \theta_1}{m_e} \sinh \theta_1 + \cosh \theta_1} \cosh\left(\frac{x}{\lambda_1}\right) \quad (4.23)$$

$$S_2 = \frac{k_p S_1(\infty)}{\frac{P_m \theta_1}{m_e} \sinh \theta_1 + \cosh \theta_1} \left(\frac{\theta_1^2}{\theta_2^2 - \theta_1^2} \right) \left[\cosh\left(\frac{x}{\lambda_1}\right) - \left(\frac{\frac{P_m \theta_1}{m_e} \sinh \theta_1 + \cosh \theta_1}{\frac{P_m \theta_2}{m_e} \sinh \theta_2 + \cosh \theta_2} \right) \cosh \frac{x}{\lambda_2} \right] \quad (4.24)$$

$$S_3 = k_p S_1(\infty) \left[1 - \frac{1}{\frac{P_m \theta_1}{m_e} \sinh \theta_1 + \cosh \theta_1} - \frac{1}{\frac{P_m \theta_1}{m_e} \sinh \theta_1 + \cosh \theta_1} \left(\frac{\theta_1^2}{\theta_2^2 - \theta_1^2} \right) \right. \\ \left. \times \left(1 - \frac{\frac{P_m \theta_1}{m_e} \sinh \theta_1 + \cosh \theta_1}{\frac{P_m \theta_2}{m_e} \sinh \theta_2 + \cosh \theta_2} \right) \right] \times \left[\cosh \frac{x}{\lambda_3} - \frac{\frac{P_m \theta_3}{m_e} \sinh \theta_3 + \cosh \theta_3}{\frac{P_m \theta_3}{m_e} \cosh \theta_3 + \sinh \theta_3} \sinh \frac{x}{\lambda_3} \right] \quad (4.25)$$

$$Q_4 = k_p S_1(\infty) - S_1 - S_2 - S_3 \quad (4.26)$$

$$\text{where } m_e = \frac{D_e}{\delta} \quad P_m = \frac{k_p D_f}{L} \quad \theta_1 = \frac{L}{\lambda_1}, \theta_2 = \frac{L}{\lambda_2}, \theta_3 = \frac{L}{\lambda_3}$$

m_e is the mass transfer coefficient across the stagnant film, and P_m denotes the permeability inside the enzyme layer. The ratio $\frac{P_m}{m_e}$ which compares the mass transfer in enzyme layer to that in bulk is also known as the Sherwood number. The dimensionless parameters θ_1 , θ_2 , and θ_3 , also known as Thiele modulus, compare the enzymatic reaction rates of phenyl valerate, phenol and catechol substrates, respectively, with their diffusion in the enzymatic layer of thickness L .

The cathodic current sensitivity (S_{pv}^C) of the electrode toward phenyl valerate substrate can then be derived from Equations 4.25 and 4.22:

$$S_{pv}^C = \frac{J_{pv}}{S_1(\infty)} = 2FP_m\theta_3 \left[1 - \frac{1}{\frac{P_m\theta_1}{m_e} \sinh\theta_1 + \cosh\theta_1} - \frac{1}{\frac{P_m\theta_1}{m_e} \sinh\theta_1 + \cosh\theta_1} \left(\frac{\theta_1^2}{\theta_2^2 - \theta_1^2} \right) \right. \\ \left. \times \left(1 - \frac{\frac{P_m\theta_1}{m_e} \sinh\theta_1 + \cosh\theta_1}{\frac{P_m\theta_2}{m_e} \sinh\theta_2 + \cosh\theta_2} \right) \right] \times \left[\frac{\frac{P_m\theta_3}{m_e} \sinh\theta_3 + \cosh\theta_3}{\frac{P_m\theta_3}{m_e} \cosh\theta_3 + \sinh\theta_3} \right] \quad (4.27)$$

where $S_1(\infty)$ denotes the bulk phenyl valerate concentration. This equation demonstrates that the bio-electrode response is affected by the rate of mass transport in the stagnant film (m_e) and the enzyme layer (P_m), as well as by the enzymatic activities toward phenyl valerate (θ_1), phenol (θ_2) and catechol (θ_3). Equation 4.27 was derived assuming that only phenyl valerate is present in the bulk. However, if only phenol is present in the bulk, then it has been shown that the following relation can be derived (Coche-Guerente, Labbe et al. 2001):

$$S_{ph}^C = \frac{J_{ph}}{S_2(\infty)} = 2FP_m\theta_3 \left(1 - \frac{1}{\frac{P_m}{m_e}\theta_2 \sinh \theta_2 + \cosh \theta_2}\right) \times \left(\frac{\frac{P_m}{m_e}\theta_3 \sinh \theta_3 + \cosh \theta_3}{\frac{P_m}{m_e}\theta_3 \cosh \theta_3 + \sinh \theta_3}\right) \quad (4.28)$$

where S_{ph}^C and $S_2(\infty)$ denote the phenol sensitivity and bulk concentration, respectively.

Similarly, if only catechol is present in the bulk, then the following relations can be derived (Coche-Guerente, Labbe et al. 1999):

$$S_{ct}^C = \frac{J_{ct}^C}{S_3(\infty)} = -2FP_m \frac{1 - \frac{P_m\theta_3}{m_e} \sinh \theta_3 - \cosh \theta_3}{\frac{P_m}{m_e} \cosh \theta_3 + \frac{\sinh \theta_3}{\theta_3}} \quad (4.29)$$

$$S_{ct}^a = \frac{J_{ct}^a}{S_3(\infty)} = 2FP_m \frac{1}{\frac{P_m}{m_e} \cosh \theta_3 + \frac{\sinh \theta_3}{\theta_3}} \quad (4.30)$$

where S_{ct}^C denotes the sensitivity of the electrode in the presence of catechol at an applied potential of -0.1 V (where major contribution to current comes from the reduction of *o*-quinone), and S_{ct}^a denotes the sensitivity at an applied potential of 0.5 V (where major contribution to current comes from oxidation of catechol which couldn't be converted to *o*-quinone by tyrosinase). For rotating disk electrodes we can assume m_e to be given by the following Levich equation (Coche-Guerente, Labbe et al. 1999):

$$m_e = \frac{D_e^{2/3}}{1.613\nu^{1/6}\omega^{-1/2}} \quad (4.31)$$

On rearranging equations 4.29 and 4.30 and substituting the value of m_e from equation 4.31, the following relations can be obtained. The following relations were used by us (data shown in the next section) to validate the model and also estimate some parameters.

$$\frac{S_{ct}^C}{S_{ct}^a} = (-1 + \cosh \theta_3) + (1.613P_m D_e^{-2/3} \nu^{1/6} \theta_3 \sinh \theta_3) \omega^{-\frac{1}{2}} \quad (4.32)$$

$$\frac{1}{S_{ct}^a} = \left(\frac{1}{2FP_m} \frac{\sinh \theta_3}{\theta_3} \right) + (1.613 \frac{D_e^{-2/3} \nu^{1/6} \cosh \theta_3}{2F}) \omega^{-\frac{1}{2}} \quad (4.33)$$

4.4.5 Validation of the model

The model was validated using NEST and tyrosinase containing bi-enzyme electrodes. Four electrodes (A, B, C and D) were used, and the steady state cathodic and anodic current sensitivities S_{ct}^C and S_{ct}^a , were measured at two different catechol concentrations (3 and 5 μM), under varying electrode rotation speeds. Similarly the cathodic current sensitivities, S_{ph}^C and S_{pv}^C , were also measured at different phenol (3 and 5 μM) and phenyl valerate concentrations (3 and 5 μM). While, the cathodic sensitivity, S_{ct}^C , remained practically constant with rotation rate, S_{ph}^C and S_{pv}^C , decreased with rotation rate.

Figure 4.3 shows reciprocal plots of S_{ct}^a and $\frac{S_{ct}^C}{S_{ct}^a}$ versus the square root of rotation rate. Both plots, as predicted by the model (equations 4.32 and 4.33), showed linearity with correlation coefficients (R^2) greater than 0.98, suggesting that the model reasonably represent the electro-enzymatic processes occurring in the presence of catechol. From the slopes and intercepts of the fitted lines in Figures 4.3a and 4.3b, Equations 4.32 and 4.33 can be used to determine $\theta_3 = 1.81 (\pm 0.2)$, $P_m = 0.0091 (\pm 0.0015)$ cm/s and $D_e = 2.2 (\pm 1.2 \times 10^{-5})$ cm²/s. Alternatively, D_e can also be determined separately using Levich plot on a bare gold electrode. The obtained value of D_e compares well with published values of D_e for catechol (Coche-Guerente, Labbe et al. 1999).

Figure 4.4 shows the current sensitivity to phenol as a function of electrode rotation speed. The sensitivity of the electrode was found to decrease with increasing rotation rates. In principle, Equation 4.28 could be fit to the data shown in Figure 4.4 and determine θ_2 , P_m and θ_3 . However, the rotating disk electrode system used by us can give data points at only six rotation speeds. To get more reliable values of the parameters, the values of P_m and θ_3 obtained with catechol present in the bulk solution were used, and Equation 4.28 was fit to the data in Figure 4.4 to give a best fit value of $\theta_2 = 0.23 (\pm 0.05)$.

Figure 4.5 shows the current sensitivity to phenyl valerate as a function of electrode rotation speed. Like phenol, the sensitivity of the electrode to phenyl valerate decreased with increasing rotation rate. Equation 4.27 was fitted to the experimental data using the previously determined P_m , θ_2 and θ_3 parameters ($\theta_3 = 1.81$, $\theta_2 = 0.23$, $P_m = 0.0091$ cm/s). A best fit value of $\theta_1 = 1.1 (\pm 0.25)$ was obtained.

To summarize the results, the average values of P_m , θ_1 , θ_2 and θ_3 came out to be 0.0091 cm/s, 1.1, 0.23 and 1.81, respectively. The thickness of the interface (L) as measured using an ellipsometer was 25 nm. If we assume partition coefficient k_p to be 1,

then the value of D_f using the relation, $P_m = \frac{D_f k_p}{L}$, would be 2.27×10^{-8} cm²/s.

Although these calculations may be approximate, but it suggests that the diffusion in the enzyme film is approximately 3 orders of magnitude slower than in bulk electrolyte.

Similar effects have already been reported in layered polyelectrolyte films (Coche-Guerente, Labbe et al. 2001). Assuming that the immobilized tyrosinase has the same kinetic constants as in the homogeneous solution, the concentrations $[E_2]$ and $[E_3]$ of monophenolase and catecholase active sites can be determined using the following relations:

$$(k_2 / K_2)[E_2] = \frac{D_f \theta_2^2}{L^2} \quad (4.34)$$

$$(k_3 / K_3)[E_3] = \frac{D_f \theta_3^2}{L^2} \quad (4.35)$$

Table 4.1 shows the calculated values of $[E_2]$ and $[E_3]$ along with the reported values of kinetic constants used to determine them (Coche-Guerente, Labbe et al. 2001). Although these calculations are coarse approximation, they suggest monophenolase active sites represent only 66% of the catecholase sites and about 40 % of the total sites.

4.4.6 Simulations and Discussions

Figure 4.6 show the simulated concentration profiles of phenyl valerate, phenol, catechol and *o*-quinone normalized to phenyl valerate bulk concentration ($S_1(\infty)$) as a function of relative position (x/L) within the interface. The concentration profile was simulated using equations 4.23-4.26, along with the experimentally determined values of different parameters ($P_m=0.0091$ cm/s, $\theta_1 = 1.1$, $\theta_2 = 0.23$, $\theta_3 = 1.81$, $\omega=500$ rpm and $D_e = 2.2 \times 10^{-5}$ cm²/s). As expected, the concentration of *o*-quinone, and the concentration

gradients of phenyl valerate ($\frac{\partial S_1}{\partial x}$) and phenol concentration ($\frac{\partial S_2}{\partial x}$), at the electrode surface ($x = 0$) are zero.

The model's predictions help explain the observed (Figure 4.5) decrease in current with increasing rotation rates in the presence of phenyl valerate. The electrochemical transduction step regenerates catechol from *o*-quinone. A portion of the catechol is lost by diffusion through the stagnant film, and the remainder is oxidized to *o*-quinone, which increases the sensor's output. As the electrode rotation rate increases, the film mass transfer coefficient also increases and increasing fraction of the catechol is lost. As a consequence, less catechol is recycled to *o*-quinone, and the *o*-quinone concentration at the electrode is reduced, leading to lower sensitivity for phenyl valerate detection. Consistent with this mechanism, Figure 4.7 shows that the predicted concentration gradient of *o*-quinone at $x=0$ decreases as the rotation rate increases.

Figure 4.8 shows the simulated current sensitivity, S_{pv}^C , as a function of amount of NEST esterase activity (θ_1) and tyrosinase's catecholase activity (θ_3), assuming $P_m = 0.0091$ cm/s and $\omega = 500$ rpm. At low θ_1 values, S_{pv}^C increases as θ_1 increases, indicating that the NEST activity is rate limiting. However, as θ_1 increases, the S_{pv}^C curve approaches an asymptote, indicating that the biosensor response is becoming limited by the catechol recycling (θ_3). For a given, θ_1 , the current sensitivity S_{pv}^C increases with θ_3 , because at higher values of catecholase activity enzymatic recycling

of *o*-quinone becomes more and more efficient, leading to amplified responses or higher sensitivities.

Amplification factor (AF) can be defined as the ratio of current sensitivities in the presence (S_{pv}^C) and absence of catecholase activity ($S_{pv, \theta_3 = 0}^C$).

$$AF = \frac{S_{pv}^C}{S_{pv, \theta_3 = 0}^C} \quad (4.36)$$

The following relation for the AF can be derived from Equation 4.33 and 4.42. This equation shows that AF is a function of Thiele modulus θ_3 and the ratio $\frac{P_m}{m_e}$, which is the reciprocal of Sherwood number.

$$AF = \left(1 + \frac{P_m}{m_e}\right) \theta_3 \left(\frac{\frac{P_m}{m_e} \theta_3 \sinh \theta_3 + \cosh \theta_3}{\frac{P_m}{m_e} \theta_3 \cosh \theta_3 + \sinh \theta_3} \right) \quad (4.43)$$

Figure 4.9 shows predicted AF values as a function of θ_3 , assuming experimentally realistic values of $P_m = 0.0091$ cm/s and $\omega = 500$ rpm. Amplification increases with θ_3 and, depending upon the rotation rate, amplification factors as high as 20 can be achieved. The mathematical model predicts about 2.5-fold signal amplification via recycling for our bi-enzyme electrode at a rotation speed of 500 rpm.

Collectively, the results of this study present an important contribution from the point of view of optimization of bi-enzyme biosensors that involve substrate recycling. The results suggest strategies that can be used to increase biosensor sensitivity. For the NEST biosensor, increasing the tyrosinase concentration and decreasing the mass transfer coefficient give higher signals for a given NEST loading. This result is interesting since tyrosinase is relatively inexpensive and commercially available, while NEST is not commercially available, and its expression and purification requires special expertise. In order to achieve higher signals, currently, we are exploring different ways of increasing tyrosinase loading on the surface. We are also looking at the possibility of using this interface as a sensor for detecting NEST inhibitors such as organophosphorous compounds.

4.5 CONCLUSIONS

This chapter presented a theoretical treatment for bi-enzyme electrodes with substrate recycling. The model was validated by studying the response of bi-enzyme rotating disk electrode consisting of two enzymes, NEST and tyrosinase, to phenyl valerate, phenol and catechol under varying rotating speeds. The validated model helped us determine and quantify the influence of important parameters such as mass transport in the bulk and enzyme layer, partition coefficients, enzyme kinetics and catechol recycling on the sensitivity of the sensor. This information can be helpful for optimizing the metrological characteristics of bi-enzyme electrodes.

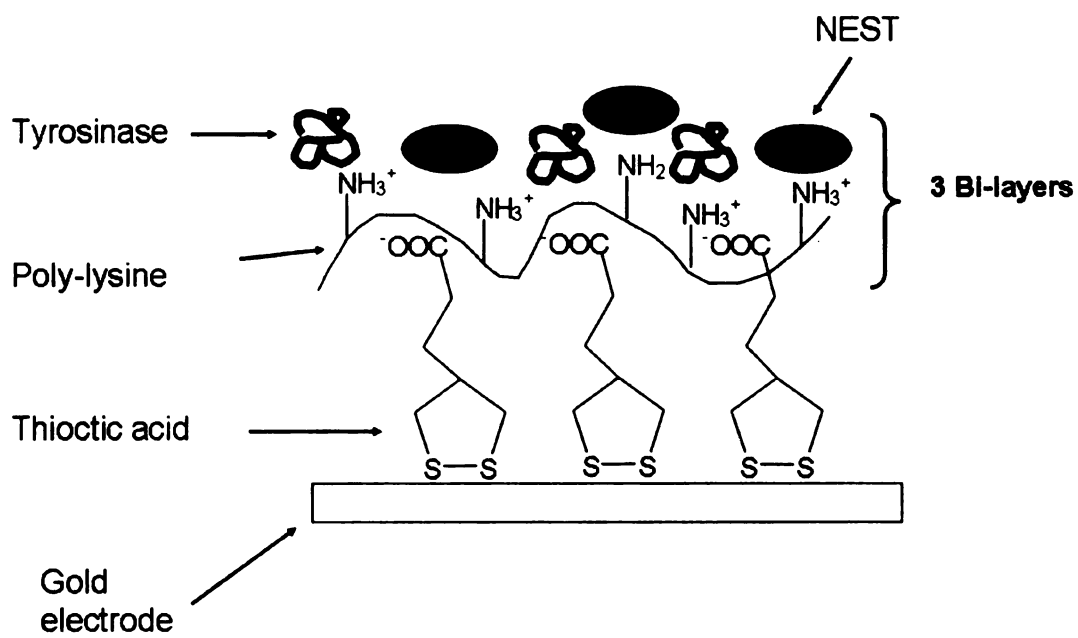


Figure 4.1: Molecular architecture of bi-enzyme electrode

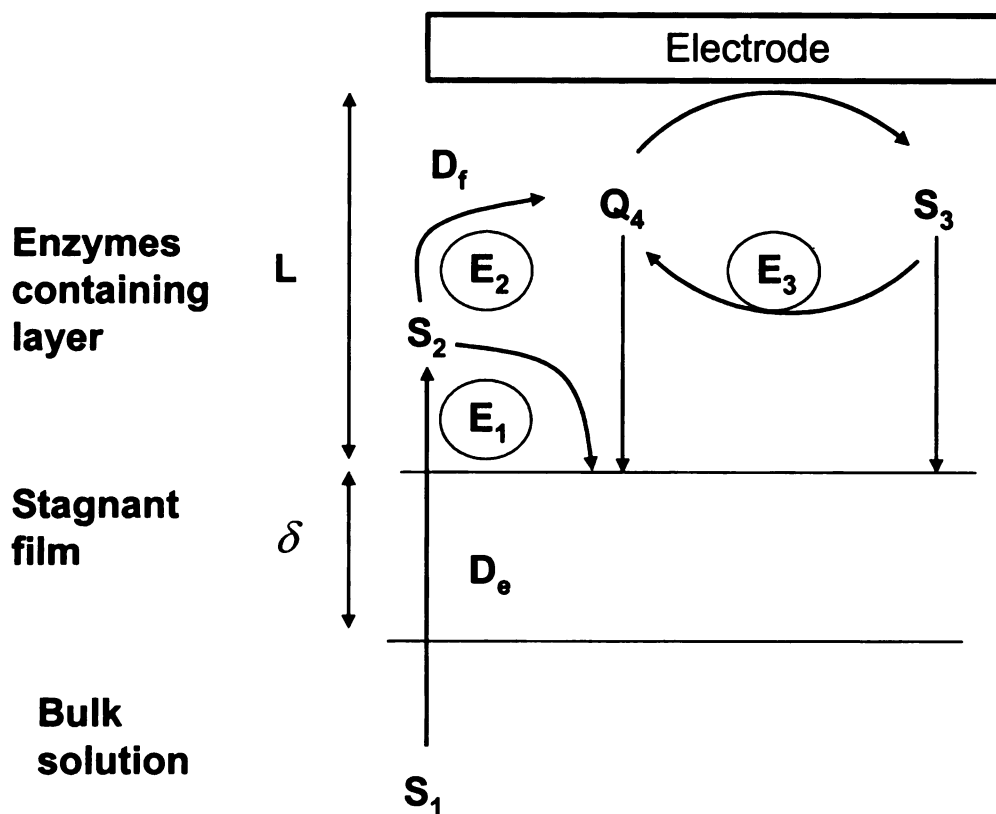
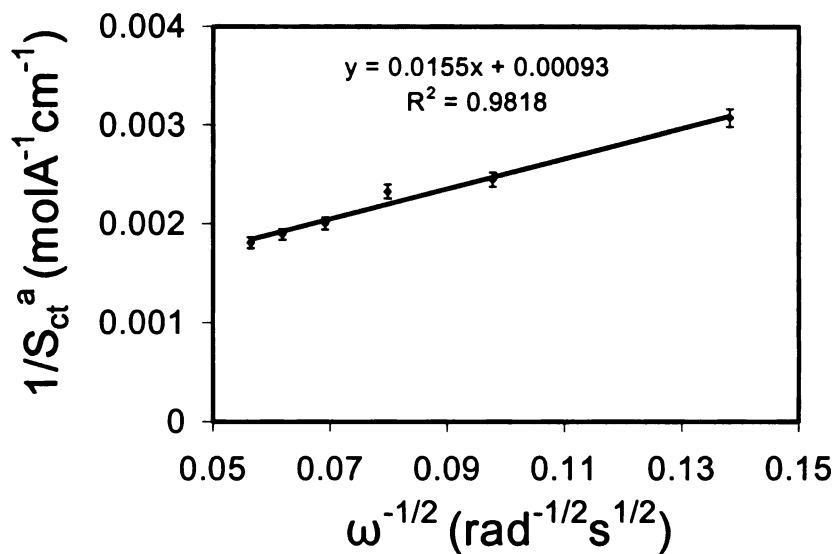
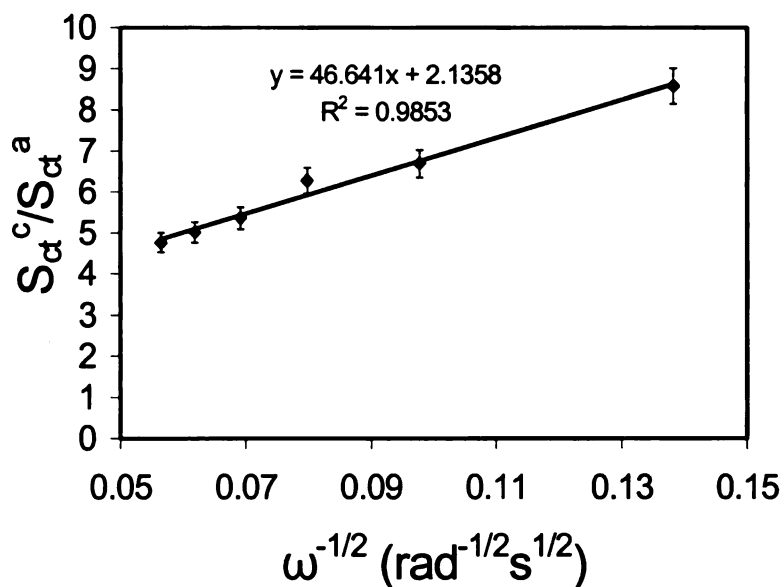


Figure 4.2: Schematic representation of a rotating disk bi-enzyme electrode and principle of its functioning in the presence of phenyl valerate substrate. S_1 , S_2 , S_3 and Q_4 denote the substrate phenyl valerate, phenol, catechol and *o*-quinone, respectively. E_1 denotes NEST esterase activity. E_2 and E_3 denote tyrosinase's phenolase and catecholase activity, respectively. L denotes the thickness of the enzyme.



(a)



(b)

Figure 4.3: Reciprocal plots of S_{ct}^a and $\frac{S_{ct}^c}{S_{ct}^a}$ versus the square root of rotation rate for electrode A.

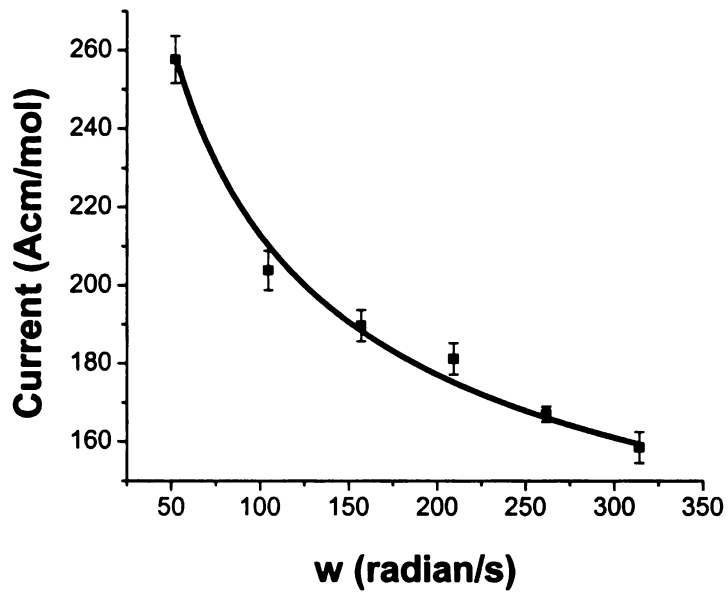


Figure 4.4: Cathodic sensitivity, S_{ph}^C , in the presence of phenol as a function of rotation rate.

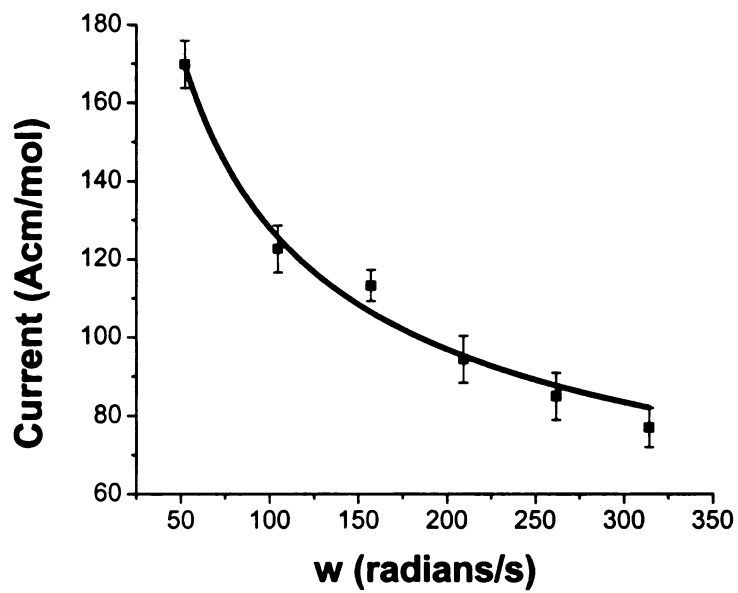


Figure 4.5: Cathodic sensitivity, S_{pv}^C , in the presence of phenyl valerate as a function of rotation rate.

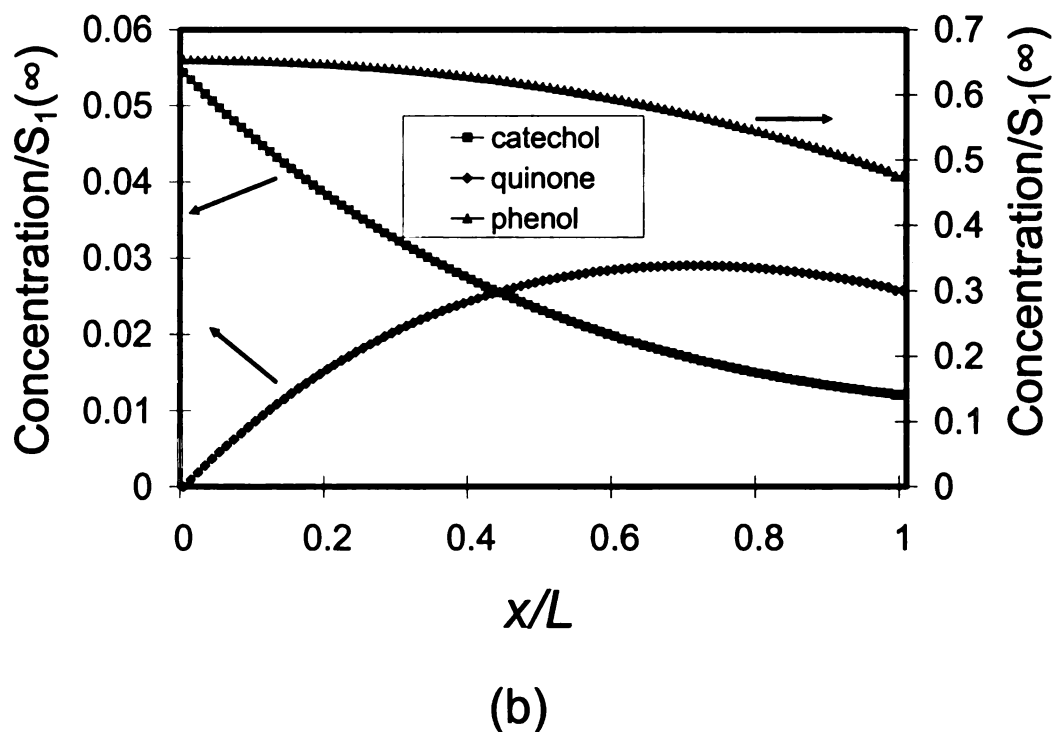
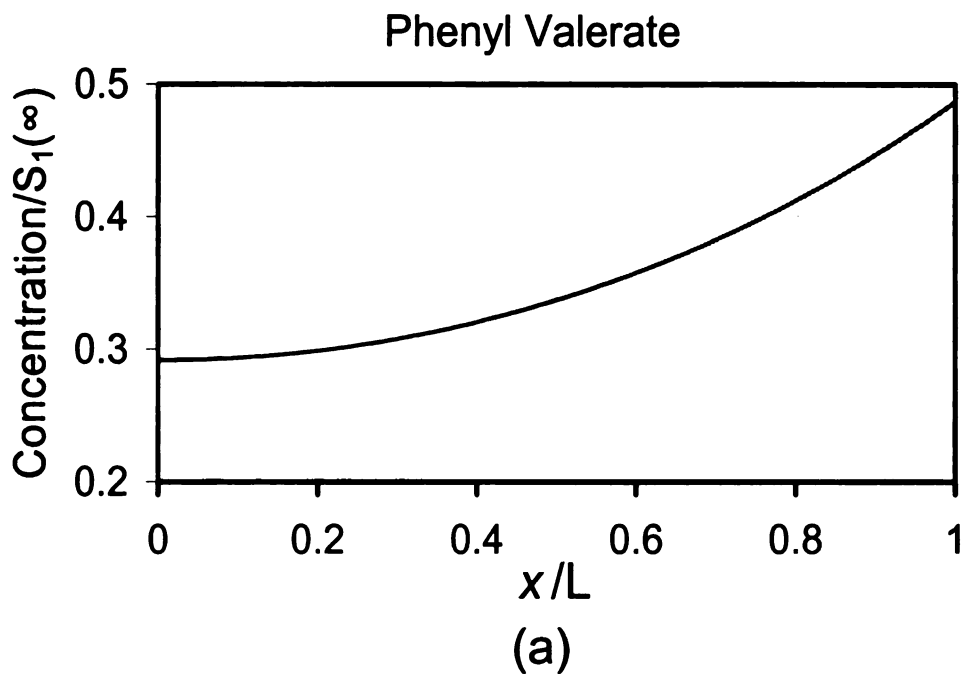


Figure 4.6: Concentration profiles of (a) phenyl valerate (b) phenol, catechol and *o*-quinone normalized to phenyl valerate bulk concentration ($S_1(\infty)$) as a function of relative position (x/L) within the bi-enzyme interface

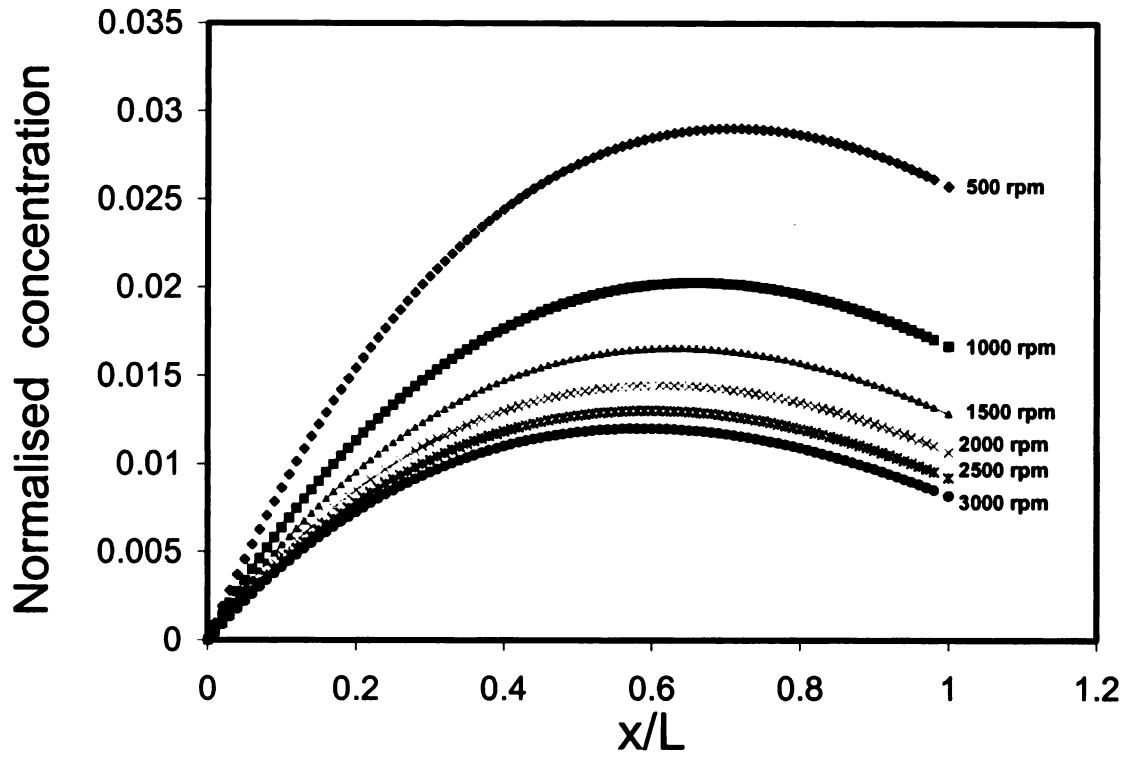


Figure 4.7: Concentration profile of *o*-quinone normalized to phenyl valerate bulk concentration ($S_1(\infty)$) at various rotation rates

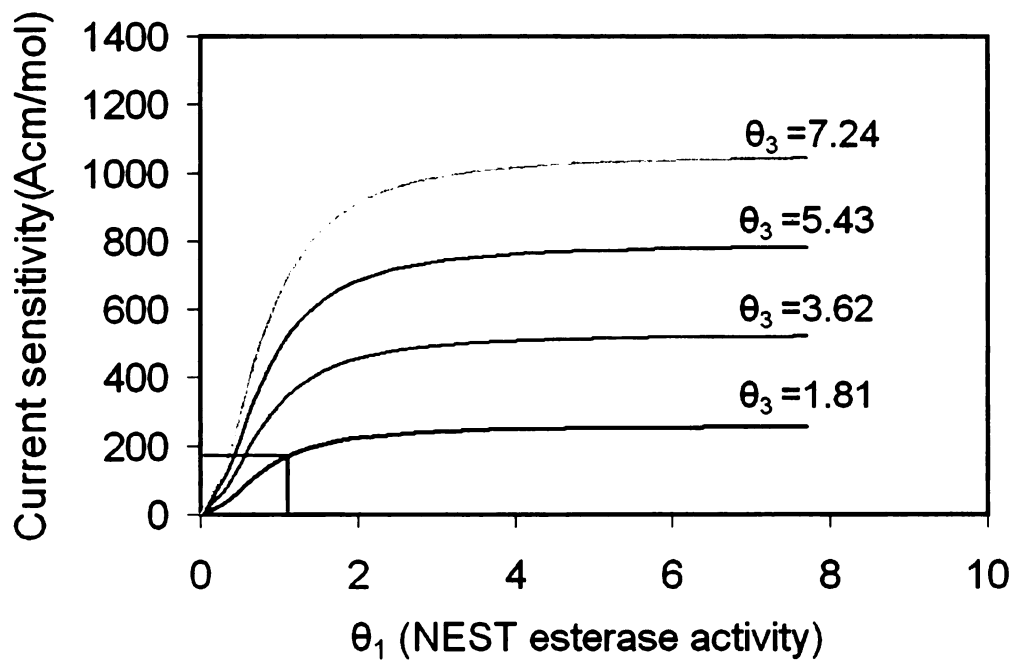


Figure 4.8: Current sensitivity, S_{pV}^C , as a function of amount of NEST esterase activity (θ_1) and tyrosinase's catecholase activity (θ_3).

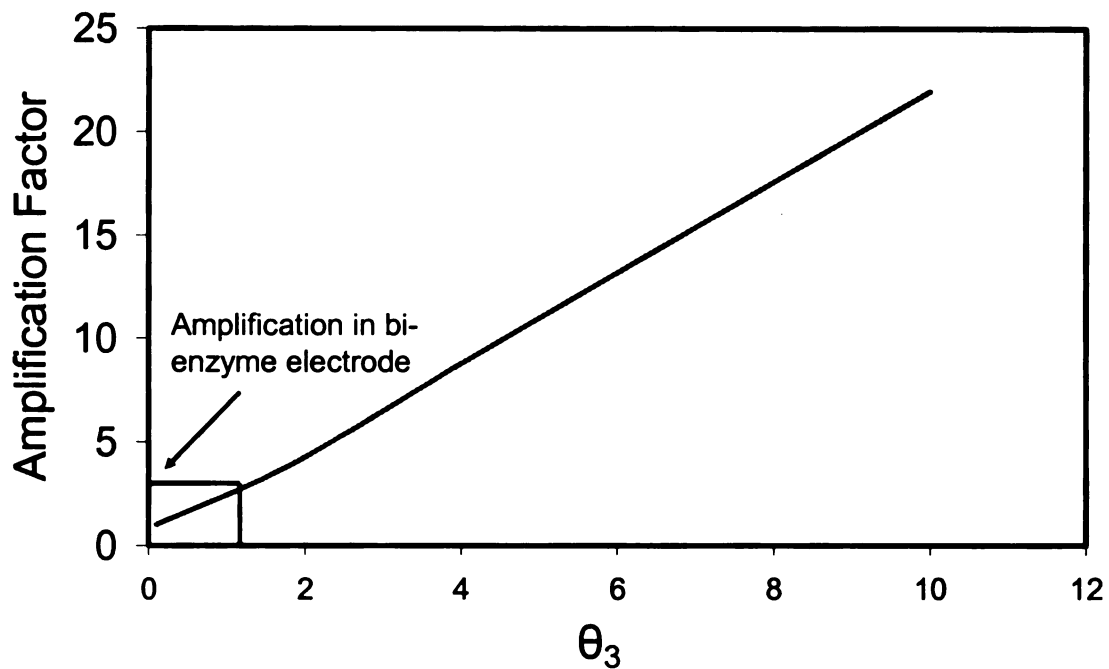


Figure 4.9: Signal amplification in bi-enzyme electrode due to the recycling of catechol. For simulation, the following values of different parameters were used: $P_m = 0.0091\text{cm/s}$, $D_e = 2.2 \times 10^{-5} \text{ cm}^2/\text{s}$, $\omega = 500 \text{ rpm}$.

Table 4.1: Kinetic characteristics of tyrosinase immobilized in bi-enzyme electrode. Values of k and K were obtained from the literature (Coche-Guerente, Labbe et al. 2001). However, enzyme concentration was calculated using equations 4.40 and 4.41.

	Monophenolase activity	Catecholase activity
K (mol/cm^3)	$(2.5 \pm 0.3) \times 10^{-7}$	$(2.2 \pm 0.2) \times 10^{-7}$
k (s^{-1})	20 ± 2	760 ± 30
k/K ($\text{mol}^{-1} \text{cm}^3 \text{s}^{-1}$)	8.4×10^7	3.45×10^9
Enzyme concentration (mol/cm^3)	2.29×10^{-6}	3.45×10^{-6}

5 ARRAYS OF LIPID BILAYERS AND LIPOSOMES ON PATTERNED POLYELECTROLYTE TEMPLATES

5.1 ABSTRACT

This paper presents novel methods to produce arrays of lipid bilayers and liposomes on patterned polyelectrolyte multilayers. We created the arrays by exposing patterns of poly(dimethyldiallylammonium chloride) (PDAC), polyethylene glycol (m-dPEG acid), and poly(allylamine hydrochloride) (PAH) on polyelectrolyte multilayers (PEMs) to liposomes of various compositions. The resulting interfaces were characterized by total internal reflection fluorescence microscopy (TIRFM), fluorescence recovery after pattern photobleaching (FRAPP), quartz crystal microbalance (QCM), and fluorescence microscopy. Liposomes composed of 1, 2-dioleoyl-*sn*-glycero-3-phosphocholine (DOPC) and 1, 2-dioleoyl-*sn*-glycero-3-phosphate (monosodium salt) (DOPA) were found to preferentially adsorb on PDAC and PAH surfaces. On the other hand, liposome adsorption on sulfonated poly(styrene) (SPS) surfaces was minimal, due to electrostatic repulsion between the negatively charged liposomes and the SPS-coated surface. Surfaces coated with m-dPEG acid were also found to resist liposome adsorption. We exploited these results to create arrays of lipid bilayers by exposing PDAC, PAH and m-dPEG patterned substrates to DOPA/DOPC vesicles of various compositions. The patterned substrates were created by stamping PDAC (or PAH) on SPS-topped multilayers, and m-dPEG acid on PDAC-topped multilayers, respectively. This technique can be used to produce functional biomimetic interfaces for potential applications in biosensors and biocatalysis, for creating arrays that could be used for high-throughput

screening of compounds that interact with cell membranes, and for probing, and possibly controlling, interactions between living cells and synthetic membranes.

5.2 INTRODUCTION

Cell membranes are complex moieties composed primarily of a bilayer lipid membrane (BLM) and associated membrane proteins. These membranes represent one of the major structural components of cells and are responsible for many vital cellular functions. Biomimetic interfaces that can mimic cell membranes and their functionalities have potential applications as biosensors and can also provide a platform for fundamental investigations of biomolecular behavior (Stelzle, Weissmuller et al. 1993; Heysel, Vogel et al. 1995; Sackmann 1996; Raguse, Braach-Maksvytis et al. 1998; Nikolelis, Hianik et al. 1999). To mimic cell membranes, supported BLMs (sBLMs) have been formed on glass, silica and unfunctionalized metal surfaces (Ariga and Okahata 1989; Kalb, Frey et al. 1992; Sackmann 1996; Tien, Barish et al. 1998; Tien and Ottova 1998; Asaka, Ottova et al. 1999; Plant 1999; Boxer 2000; Ross, Bondurant et al. 2001; Favero, D'Annibale et al. 2002; Wiegand, Arribas-Layton et al. 2002; Graneli, Rydstrom et al. 2003). Although sBLMs have enabled researchers to probe properties such as phase transition, lateral diffusion, permeation, and lipid-protein interactions, they have two serious limitations: (1) they do not provide space between the bilayer and the underlying substrate to accommodate hydrophilic moieties of trans-membrane proteins, and to allow lateral mobility of membrane components, and (2) they lack the ionic reservoirs that most cell membranes need to ensure their biological function.

To overcome these limitations, new approaches that involve the use of hydrophilic cushions on which BLMs can be deposited are being adopted by researchers. Such cushions have consisted of hydrogels, polymeric tethers, polymer films and polyelectrolyte multilayers (PEMs) (Raguse, Braach-Maksvytis et al. 1998; Cassier, Sinner et al. 1999; Naumann, Schmidt et al. 1999; Stora, Lakey et al. 1999; Wagner and Tamm 2000; Zhang, Longo et al. 2000; Cornell, Krishna et al. 2001; Krishna, Schulte et al. 2001; Krysinski, Zebrowska et al. 2001; Sinner and Knoll 2001; Kugler and Knoll 2002; Naumann, Prucker et al. 2002; Proux-Delrouyre, Elie et al. 2002; Zebrowska, Krysinski et al. 2002; Zhang, Vidu et al. 2002; Ma, Srinivasan et al. 2003; Moya, Richter et al. 2003; Naumann, Schiller et al. 2003; Naumann, Walz et al. 2003; Perez-Salas, Faucher et al. 2003; Terrettaz, Mayer et al. 2003; Yin, Burns et al. 2003; Moncelli, Becucci et al. 2004; Munro and Frank 2004). PEMs offer the following advantages (Cassier, Sinner et al. 1999; Zhang, Longo et al. 2000; Kugler and Knoll 2002; Zhang, Vidu et al. 2002; Ma, Srinivasan et al. 2003; Moya, Richter et al. 2003; Perez-Salas, Faucher et al. 2003): (1) they are robust and easy to fabricate, (2) they can be deposited on virtually any surface, (3) they can provide a reservoir for electron transfer mediators and cofactors for sensor applications, and (4) their porosity and flexibility may allow the protein to exist in its natural conformation while bound to the BLM. Lipid bilayers composed of negatively charged lipids like 1, 2-dioleoyl-*sn*-glycero-3-phosphate (monosodium salt) (DOPA), 1-stearoyl-2-oleoyl-phosphatidylserine (SOPS), and 1,2-dimyristoyl-*sn*-glycero-3-[phospho-*rac*-(1-glycerol)] (sodium salt) (DMPG) blended with other zwitterionic lipids like 1, 2-dioleoyl-*sn*-glycero-3-phosphocholine (DOPC) and 1-palmitoyl-2-oleoylphosphatidylcholine (POPC) have already been shown to form on

polyelectrolytes such as poly(allylamine hydrochloride) (PAH), poly(ethyleneimine) (PEI) and poly(diallyldimethyl ammonium chloride) (PDAC) coated substrates (Sohling and Schouten 1996; Cassier, Sinner et al. 1999; Zhang, Booth et al. 2000; Zhang, Longo et al. 2000; Kugler and Knoll 2002; Ma, Srinivasan et al. 2003). These studies (Kugler and Knoll 2002) have shown that upon increasing the percentage of charged lipids, lipid coverages increase, and diffusion coefficients decrease. In another approach (Tiourina, Radtchenko et al. 2002), PEMs were adsorbed on melamine formaldehyde latex particles which were soluble at low pH, resulting in the formation of thin polyelectrolyte shells upon dissolving the core. Lipid bilayers were then formed on the empty shells by exposing them to charged vesicles. The properties of this system as an artificial cell were then evaluated.

Arrays of BLMs have also been fabricated on glass and gold surfaces (Groves, Ulman et al. 1997; Groves, Boxer et al. 1998; Hovis and Boxer 2000; Kung, Groves et al. 2000; Kung, Kam et al. 2000; Zhang, Longo et al. 2000; Kam and Boxer 2001; Groves and Boxer 2002; Proux-Delrouyre, Elie et al. 2002; Saccani, Castano et al. 2003). In one approach, a patterned poly(dimethyl siloxane) (PDMS) stamp was brought into contact with an sBLM formed on a glass slide and then removed (Hovis and Boxer 2000). Approximately 90% of the lipids in areas in contact with the stamp were transferred to the stamp's surface, resulting in arrays of BLM patches separated from one another by regions of bare glass. The same group showed that the bilayer can be preassembled directly onto oxidized PDMS surfaces and then transferred intact to the glass slide. Bilayer patches in the resulting arrays were found to be fully fluid and stable under water. To date, this methodology has been applied only to a limited number of surfaces.

There is general interest in techniques that can help extend these types of approaches to other substrates, and also address the two limitations of sBLMs described earlier. The approach in this study is based on the ionic layer-by-layer (LBL) assembly technique introduced by Decher (Decher and Hong 1991), microcontact printing (μ CP) developed by the Whitesides group (Kumar and Whitesides 1993), and the polymer-on-polymer stamping process (POPS) developed by Hammond and coworkers (Jiang and Hammond 2000; Jiang, Zheng et al. 2002).

In this paper (Kohli, Vaidya et al. 2006), we present methods to fabricate arrays of BLMs and liposomes on PEMs. Arrays of BLMs were created by exposing PDAC patterns, polyethylene glycol (m-dPEG acid) patterns, and PAH patterns on PEMs to liposomes of various compositions. Total internal reflection fluorescence microscopy (TIRFM) and quartz crystal microbalance (QCM) gravimetry were used to monitor liposome adsorption to PEMs. Fluorescence recovery after pattern photobleaching (FRAPP) and fluorescence microscopy were also used to characterize the resulting interfaces.

5.3 EXPERIMENTAL SECTION

5.3.1 Materials

Sulfonated poly(styrene) (SPS) ($M_w \sim 70,000$), poly(diallyldimethyl ammonium chloride) (PDAC) ($M_w \sim 100,000$), and poly(allylamine hydrochloride) (PAH) were obtained from Sigma (St. Louis, MO). 1,2-dioleoyl-*sn*-glycero-3-phosphate (monosodium salt) (DOPA, Figure 5.1b), 1,2-dioleoyl-*sn*-glycero-3-phosphocholine (DOPC, Figure 5.1a), and 1-palmitoyl-2-[6-[(7-nitro-2-1,3-benzoxadiazol-4-

yl)amino]hexanoyl]-*sn*-glycero-3-phosphocholine(16:0-06:0 NBD PC, Figure 5.1c) were purchased from Avanti Polar Lipids (Alabaster, AL). NBD-PC serves as the fluorescence probe. 1-tetradecanethiol, 4-(2-hydroxyethyl)piperazine-1-ethanesulfonic acid sodium salt (HEPES) was obtained from Fluka (St. Louis, MO). The m-dPEG acid was purchased from Quanta Biodesign (Powell, OH). Structures of PDAC, PAH, SPS and m-dPEG acid are given in Figure 5.2. Sylgard 184 silicone elastomer kit (Dow Corning, Midland MI) was used to prepare the poly(dimethylsiloxane) (PDMS) stamps for μ CP. The fluorosilanes were purchased from Aldrich Chemical (St. Louis, MO). Ultrapure water was supplied by a Nanopure-UV four-stage purifier (Barnstead International, Dubuque, IA); the purifier was equipped with a UV source and a final 0.2 μ m filter.

5.3.2 Preparation of stamps

The PDMS stamps were made by pouring a 10:1 solution of elastomer and initiator over a prepared silicon master. The silicon master was pretreated with fluorosilanes to facilitate the removal of the PDMS stamps from the silicon masters. The mixture was allowed to cure overnight at 60 °C. The masters were prepared in the Microsystems Technology Lab at MIT and consisted of features (parallel lines and circles) from 1 to 20 μ m.

5.3.3 Preparation of liposomes

Small unilamellar liposomes of two different compositions were prepared: (1) 89% DOPC, 10% DOPA and 1% NBD-PC (referred in the paper as 90% DOPC/10% DOPA), (2) 79% DOPC, 10% DOPA and 1% NBD-PC (referred in the paper as 80% DOPC/20% DOPA). These liposomes were prepared by mixing appropriate amounts of

lipids in chloroform. This mixture was then dried under nitrogen, making sure lipid formed a thin, cake-like film on the walls of the test tube. The residual chloroform was removed under high vacuum. The lipids were then reconstituted in HEPES buffer (pH 7.4, 100 mM NaCl), and the resulting liposome solution was sonicated until it became clear using a Bransonic bath sonicator (Branson Ultrasonics Corporation, Danbury, CT).

5.3.4 Preparation of Polyelectrolyte Multilayers (PEMs)

A Carl Zeiss slide stainer equipped with a custom-designed ultrasonic bath was connected to a computer to perform LBL assembly (Yoo, Shiratori et al. 1998; Lee, Zheng et al. 2002; Zheng, Lee et al. 2002; Lee, Hammond et al. 2003). For PDAC/SPS and PAH/SPS multilayers, the concentration of SPS, PDAC and PAH solution was 0.01 M, 0.02 M and 0.01M respectively as based on the molecular repeat units. All polyelectrolyte solutions contained 0.1 M NaCl and were at a pH of 7.0. To deposit PEMs, the glass slides were cleaned with a dilute Lysol water mixture in a sonicator. These slides were then dried under N₂ gas and were further cleaned using Harrick plasma cleaner (Harrick Scientific Corporation, Broomfield, NY) for 10 min at 20 Pa. To form the first polyelectrolyte bilayer, the slides were immersed for 20 min in a PDAC (or PAH) solution. Following two sets of 5 min water rinse with agitation, the slides were subsequently placed in a SPS solution for 20 min. They were rinsed again with water, and this process was repeated to build multiple layers.

5.3.5 Preparation of arrays:

Two different schemes were used to prepare arrays of BLMs. **Scheme 1** (Figure 5.3): A PDMS stamp was dipped in a 250 mM solution of PDAC (or 200 mM solution of

PAH) in 75/25 ethanol-water mixture for about 20 min (Jiang and Hammond 2000; Jiang, Zheng et al. 2002). The stamp was then washed with ethanol, dried under nitrogen and brought in contact with a glass slide that was coated with 5 PDAC/SPS (or PAH/SPS) bilayers, with SPS forming the uppermost layer. The stamp was removed after 15 min, and the resulting PDAC (or PAH) patterns were then rinsed with water to remove unbound or loosely bound PDAC (or PAH). The stamp was then exposed to DOPC/DOPA liposomes of varying compositions. **Scheme 2** (Figure 5.4): A PDMS stamp was dipped in a 100 μ M solution of m-dPEG acid in a 75/25 ethanol-water mixture for 30 min (Kidambi, Chan et al. 2004). The stamp was then washed, dried under nitrogen and brought in contact with the glass slide coated with 4.5 PDAC/SPS multilayers with PDAC as the topmost layer. The stamp was removed after 20 min and the resulting m-dPEG acid patterns were then rinsed with water to remove excess m-dPEG acid. These patterns were then exposed to negatively charged DOPC/DOPA liposomes. All the fluorescence images were obtained using the Nikon Eclipse E 400 microscope (Nikon, Melville, NY) having a filter cube (Ex: 465-495/DM: 505/Em: 515-555).

5.3.6 Total internal reflection microscopy:

The experimental setup and the flow cell for TIRFM have been described previously (Gajraj and Ofoli 2000). Briefly, the apparatus consists of an inverted microscope (Zeiss Axiovert 135M, Carl Zeiss Inc. Thornwood, NY), the 488 nm line of a 5W continuous wave argon ion laser (Lexel Lasers Model 95, Fremont, CA), a side-on photomultiplier tube (Hamamatsu R4632, Bridgewater, NJ) jacketed in a thermoelectrically cooled housing (TE 177-TSRF, Products for Research, Danvers, MA), a CCD camera (NTI,

VE1000, Dage-MTI, Michigan City, IN), and a modular automation controller (MAC 2000, Ludl Electronic Products, Hawthorne, NY) that regulates the voltage supply to the photo-multiplier tube and controls translation of the X-Y stage. A double syringe pump system (Model 551382, Harvard Apparatus South Natick, MA) was used for infusion and withdrawal of sample solutions at identical rates from a custom designed flow cell. For measurements that require photon counting, an SR400 photon counter (Stanford Research Systems, Sunnyvale, CA) was used after the output signal from the PMT was amplified by a fast preamplifier (SR445, Stanford Research Systems, Sunnyvale, CA). Fluorescence intensities were recorded using software written in Labview 6.0 (National Instruments, Austin, TX). A 500 nm long-pass band filter was used to separate the excitation and emission wavelengths. An optical chopper (SR 540, Stanford Research Systems, Sunnyvale, CA) was used to prevent unintended photobleaching of fluorophores during experiments. The photon counter was triggered by an output reference voltage from the chopper, so that data collection only occurred during periods when the flow cell was illuminated by the monitoring beam. For TIRFM experiments, the flow cell was initially filled with buffer. Subsequently, a liposome solution was introduced into the flow cell at a controlled flow rate. After filling the flow cell, the infusion was halted, and adsorption was allowed to continue for 1 h, followed by a buffer wash (for desorption experiments or FRAPP experiments). Measurements were done at a temperature of $22^{\circ}\text{C} \pm 1^{\circ}\text{C}$, which is above the phase transition temperature of both DOPC (-20°C) and DOPA (-8°C) (Albrecht, Johnston et al. 1982).

5.3.7 Fluorescence recovery after pattern photobleaching (FRAPP):

The experimental configuration used for FRAPP has been depicted in Figure 5.5. Stripe patterns were imposed on the substrate by directing the 488 nm laser beam (expanded through a 5X beam expander (Edmund optics, Barrington NJ) through a 50 or 100 line per inch Ronchi ruling (Edmund optics, Barrington,NJ) placed in a real image plane. Placing a ruling in a back image plane, results in projection of a sharply focused pattern of alternating dark and bright fringes on the substrate in the sample plane. This back real image plane is located near the epi-port of the Axiovert 135M microscope, coincident with the field iris diaphragm of a fluorescence light illuminator (Zeiss) mounted through the epi-port. The fluorescent light illuminator has a lens that projects the beam through a Zeiss filter cube (Ex: 450-490/DM: 510/Em: 515-565), and a 32X Zeiss objective on to the substrate. For focusing the objective, a fluorescent coating was brushed onto a glass slide using a yellow fluorescent marker (Sanford). The objective position was then adjusted till the fringes appeared in sharp focus. The fringe spacing was estimated by using a reticule containing 10 lines per centimeter in the eyepiece. The glass slide was then replaced by the sample slide. Prior to initiating photobleaching, minute adjustments were made to the objective focus knob to bring the fringes into sharp focus.

Beam alignment was checked at the start of each experiment and objective focusing was performed prior to initiation of every FRAPP experiment. For FRAPP experiments, it is crucial that the monitoring beams and the photobleaching beams be precisely coincident. Checking that the beams coincided was accomplished with the following steps. (1) The monitoring and photobleaching beams were projected on to a screen some distance away from the vibration isolation table, and beam recombination

was checked.(2) Occasionally, as an additional check for recombination, once the laser beam was directed through the Ronchi ruling so that fringe pattern was formed on the fluorescently coated glass slide, a CCD camera or the microscope oculars was used to reconfirm that the beams recombined by observing the overlaying of the faint monitoring fringes over the photobleaching fringes (Robeson 1995). For all experiments, the monitoring beam intensity ranged from 1 μW to 5 μW . For photobleaching, the beam intensity required was approximately 0.5 W. Additional neutral density filters (NDF) were required to attenuate the monitoring beam to the desired level. The use of additional NDFs causes significant deviation in the path of the monitoring beam, so checking for recombination is especially crucial. A high bleaching intensity is required to obtain a sufficient bleach depth within a reasonable time. Typical bleach times varied from 350 ms to 500 ms. Stripe periodicity in the sample plane was approximately 25 μm .

For FRAPP experiments, liposome adsorption on the polyelectrolyte coated substrates was initiated by directly introducing the liposome solution at a flow rate of 0.34 ml/min for approximately 10-12 minutes using the syringe pump. The infusion was then halted and adsorption was allowed to continue for approximately 45 minutes. The flow cell was subsequently flushed with 4-5 flow cell volumes of buffer in order to remove the fluorescently labeled liposomes in the bulk solution.

5.3.8 Theory and Data Analyses for Fluorescence recovery after pattern photobleaching

FRAP is a technique that is commonly used to obtain estimates of translational (lateral) mobilities of proteins or lipids. There are two principal variants of this method. The first involves using a focused laser beam to create a small spot. This is known as spot

photobleaching and can be effected using epi- illumination as well as using TIRFM. In the second method (FRAPP), a laser beam is passed through a Ronchi ruling placed in a back image plane to create a pattern of alternating dark and bright stripes of well defined periodicity over a broadly illuminated area. The principle advantage of FRAPP over spot photobleaching lies in the well defined characteristics of the pattern obtained in the sample plane. For spot photobleaching, the recovery kinetics and shape depend very strongly on the shape of the focused spot at the interface. The precise shape of the spot is difficult to discern as the beam travels through several optics in order to form the spot. As a result there is considerable uncertainty in measurements of diffusion coefficient especially for non-ideal samples. In contrast the well defined periodicity of the stripe pattern produced in the sample plane offers two distinct advantages: (i) It allows us to measure slow as well as fast diffusion coefficients (10^{-10} cm²/s to 10^{-7} cm²/s), as the stripe periodicity can easily be varied and (ii) It allows us to examine samples where multiple populations with different mobilities coexist, using models that describe such populations. Other variants of FRAPP involve creation of the stripe pattern using the intersection of two beams either in the sample plane (using TIRF illumination) or in a back image plane (using EPI illumination). The advantage of using TIRFM-FRAPP over EPI-FRAPP is that due to the surface selectivity of TIRFM, a buffer wash to eliminate bulk fluorophores is not necessary. The trade-off is the complexity in the experimental configuration.

5.3.9 Theory

A complete mathematical analysis of fluorescence recovery after pattern photobleaching has been presented by Starr and Thompson (Starr and Thompson 2002).

A brief description of this analysis is presented below. Consider a sample of mobile fluorescent lipids with diffusion coefficient D . The fluorescence emission from such a sample can be described as:

$$F(t) = Q \int_{-\infty}^{\infty} \int_{-\infty}^{\infty} I(x, y) C(x, y, t) dx dy \quad (5.1)$$

where Q is a proportionality constant that incorporates factors such as fluorophore quantum yield and the instrument constant, $I(x, y)$ is the monitoring beam intensity and $C(x, y, t)$ is the concentration of unbleached molecules as a function of position and time. The equation that describes the intensity profile for a Gaussian-shaped laser beam intersected by a Ronchi ruling placed in a back image plane is given by

$$I(x, y) = \frac{I_0}{2} \exp\left[-\frac{2(x^2 + y^2)}{s^2}\right] \cdot \left[1 + \sum_{n \text{ odd}} c_n \cos(nkx)\right] \quad (5.2)$$

Here, I_0 is the intensity at the origin, s is the $1/e^2$ radius of the expanded beam, k is the spatial frequency of the pattern, superimposed on the sample plane, defined by:

$$k = \frac{2\pi}{a} \quad ; \quad c_n = \frac{4}{n\pi} (-1)^{\left(\frac{n-1}{2}\right)} \quad (5.3)$$

and a is the spatial period of the stripe pattern. The concentration profile of diffusing fluorophores is,

$$C(x, y, t) = \frac{1}{4\pi Dt} \int_{-\infty}^{\infty} \int_{-\infty}^{\infty} C(x', y', 0) \cdot \exp\left[-\frac{(x-x')^2 + (y-y')^2}{4Dt}\right] dx' dy' \quad (5.4)$$

Th

fo

pu

pr

ne

5.

T

M

T

fl

The initial concentration of unbleached fluorophores in the sample is given by:

$$C(x, y, 0) = C \exp[-KI(x, y)] \quad (5.5)$$

where C is the total fluorophore concentration and K is a constant that incorporates the bleach pulse duration, quantum yield and absorptivity of the fluorophores.

After developing Equation (5.1) using Equations (5.2), (5.3), (5.4) and (5.5), for cases where the stripe periodicity is small compared to the illuminated area, the following equation can be derived for a single mobile species model, which assumes that there is one population of mobile fluorophores, in addition to an immobile fraction.

$$\phi(t) = \phi(0) + \frac{\mu}{2} [1 - \phi(0)] \cdot \left[1 - \left(\frac{8}{\pi^2} \right) \cdot \left\{ \exp\left(-\frac{4\pi^2 Dt}{a^2} \right) + \frac{1}{9} \exp\left(-\frac{36\pi^2 Dt}{a^2} \right) \right\} \right] \quad (5.6)$$

for $t \geq 0$, where $\phi(t)$ is the ratio of the postbleach fluorescence ($t > 0$, after the bleach pulse) to the prebleach fluorescence ($t < 0$), μ represents the fraction of the fluorophores present that are mobile and a and D have already been defined previously. This analysis neglects rapidly decaying (higher order) terms.

5.3.10 Data Analysis and curve fitting

The model was fit to the data using OriginPro 7.5 (OriginLab Corporation, Northampton MA) which uses the Levenberg-Marquardt algorithm for non-linear least squares fitting. The post-bleach fluorescence emission intensity was normalized against the pre-bleach fluorescence emission intensity ($t < 0$).

5.3.11 Microgravimetric experiments:

A QCM analyzer (5 MHz crystals, Maxtek Inc., Research Quartz Crystal Microbalance, Santa Fe Springs, CA) linked to a computer with RQCM data log software (Maxtek Inc.) was used for microgravimetric measurements. Quartz crystals (Maxtek Inc.) (geometrical area 1.26 cm²) were used. The QCM crystals were cleaned in piranha solution (seven parts by volume concentrated sulfuric acid and three parts hydrogen peroxide) for 30 s and then dipped in a 1 mM solution of 3-mercaptopropanoic acid in ethanol for 24 h. PAH/SPS and PDAC/SPS multilayers were then deposited ex-situ on the crystals according to previously described procedures. Frequency changes of the quartz crystals were measured after obtaining a baseline oscillation frequency change using a 10 mM HEPES buffer (pH 7.4). The measurements were done at room temperature.

5.4 RESULTS AND DISCUSSIONS

5.4.1 Characterization of liposome adsorption by TIRFM

Curves A and B in Figure 5.6 depict adsorption of negatively charged liposomes composed of 90% DOPC/10% DOPA to PEMs, with positively charged PDAC and negatively charged SPS as the top layers, respectively. The higher intensities obtained in Curve A indicate that the liposomes adsorbed preferentially onto PDAC, presumably due to electrostatic interactions. To investigate the role of liposome charge on subsequent adsorption, we repeated the experiments with liposomes composed of 80% DOPC and 20% DOPA (Curves C and D in Figure 5.6), with PDAC and SPS as the top layer, respectively. The higher concentration of negatively charged lipids (DOPA) in the

liposomes further increased the preference of liposomes for PDAC, suggesting that adsorption of liposomes on PEMs is significantly influenced by electrostatic interactions between the charged lipids and polyelectrolytes.

Curves C and D depict experiments conducted with a separate batch of liposomes from those represented by Curves A and B. Due to variability in liposome characteristics (due to small changes in labeling ratios, etc.), the magnitude of fluorescence emission may vary somewhat from batch to batch. However, unlike the case for Curve A, Curve C for adsorption on PDAC does not appear to approach a saturation value within the duration of the experiment. This may be the result of multilayer deposition at the higher concentrations of DOPA. To avoid the possibility of multilayer formation, liposomes composed of 10% DOPA and 90% DOPC were used for all remaining experiments.

To determine the reversibility of liposome adsorption to PDAC/SPS PEMs, the flow cell was flushed with 3-4 volumes of liposome-free buffer after liposome adsorption. The wash significantly reduced the fluorescence emission when SPS was the top layer, but had a much smaller effect when PDAC was the top layer (data not shown). This result suggests that the lipids are binding more strongly to PDAC than to SPS. It is possible that the buffer wash experiments reflect, in part, depletion of liposomes in the bulk liquid. However, the intensity of the evanescent wave decays exponentially with distance from the interface, and has a penetration depth of only about 80 nm in the TIRFM setup used to conduct these experiments. As a result, illumination of fluorophores in the bulk solution would only make a small contribution to the total fluorescence emission measured. In fact, this interfacial sensitivity allowed TIRFM to monitor

liposome adsorption on slides coated with lipid monolayers to show that binding kinetics are strongly influenced by buffer ionic strength (Kalb, Frey et al. 1992).

Liposome adsorption on surfaces coated with m-dPEG acid (see structure in Figure 5.2) was also studied. Figure 5.7a shows liposome adsorption onto PEMs with m-dPEG as the top layer, followed by a wash with liposome free buffer. While some lipids did adsorb onto the m-dPEG acid layers, flushing the flow cell with 3-4 ml of buffer after adsorption resulted in a large decrease in fluorescence for m-dPEG acid coated substrates. This suggests that the liposomes were only loosely bound. By contrast, a buffer wash after approximately 45 min of liposome adsorption produced only a small decrease in fluorescence emission in the case of PEMs topped with PDAC (Figure 5.7b).

In the experiments depicted in Figure 5.7b, liposome adsorption to PEMs with either PDAC (top curve) or m-dPEG acid (bottom curve) as the topmost layer was halted by introducing buffer (at $t = 0$ min on the graph), and then the fluorescence emission intensities were monitored to track the process of desorption. To enable direct comparison of the results, the fluorescence emission intensities in each data set were normalized against the corresponding fluorescence emission intensity recorded prior to initiation of the buffer wash. There was a 70% decrease in the fluorescence emission intensity for the m-dPEG case, compared to a 10% decrease for PDAC. The apparent weakness of liposome adsorption on surfaces coated with both SPS and m-dPEG was confirmed when fluorescence microscopy was used to characterize arrays of BLMs deposited on patterns of PEMs with PDAC, SPS, and m-dPEG as the topmost layer (results discussed below). While the mechanism by which PEG resists biomolecular adsorption is not completely understood, it is believed to stem either from steric

exclusions, which is an entropic effect caused by the unfavorable change in free energy associated with the dehydration and confinement of polymer chain with high conformational freedom (Harris 1992), or from long range electrostatic repulsions (Feldman, Hahner et al. 1999; Kreuzer, Wang et al. 2003). Previous studies from our group have shown that m-dPEG acid can also resist the adsorption of PDAC (Kidambi, Chan et al. 2004), which is a positively charged polyelectrolyte. Therefore, we believe the resistance of m-dPEG acid to negatively charged liposomes stems primarily from steric repulsion.

5.4.2 Formation of arrays of lipid bilayers

Figures 5.8a and 5.8b show fluorescence images of the line and circular patterns, respectively, of liposomes deposited on PDAC. As clearly shown by these results for both linear and circular arrays, liposomes bound preferentially to PDAC (brightly fluorescing features), and negligibly to SPS (dark, featureless background). Similar results were obtained when liposomes were deposited on a surface stamped with a weak polyelectrolyte (PAH) instead of a strong polyelectrolyte (PDAC) on SPS (Figure 5.8c). These results are consistent with those obtained during the adsorption experiments (Figure 5.6).

In another approach, m-dPEG acid was stamped on a PEM-coated glass slide, with PDAC being the topmost layer. The m-dPEG acid molecule has a carboxylic acid group on one end. At a pH above the pK_a , the acid group has a negative charge and can be stamped onto PDAC, resulting in patterns of m-dPEG acid on PDAC (Kidambi, Chan et al. 2004). Upon subsequent exposure to the liposome solution, liposome adsorption

occurred on the exposed PDAC, but not on the m-dPEG acid patterns (Figure 5.9). Therefore, the fluorescence patterns in Figure 5.9 are the negative replicas of those in Figure 5.8. This ability to make either the positive or the negative image of the stamp adds to the versatility of this technique. Similar fluorescence images were obtained when PEM coated glass slides, with PAH being the topmost layer were used (data not shown).

5.4.3 Assessment of liposome adsorption and rupture to form bilayers

FRAPP was used to determine if the adsorbed liposomes remained intact on the surface or ruptured to form a bilayer. Figures 5.10a and 5.10b show the recovery curves for lipids deposited on PEMs with PDAC and PAH as the topmost layer, respectively. Fluorescence recovery for lipids on PDAC and PAH was adequately described by the single mobile species model, which assumes that there is one population of mobile fluorophores, in addition to an immobile fraction. Unlike spot photobleaching, where 100% recovery of fluorophores is possible for a completely formed BLM, only 50% recovery is theoretically possible in FRAPP under the same conditions.

The average D values on PAH and PDAC were comparable ($0.224 \times 10^{-8} \text{ cm}^2/\text{s}$ and $0.288 \times 10^{-8} \text{ cm}^2/\text{s}$, respectively). The average mobile fraction (μ) on PAH (0.68) was significantly higher than that on PDAC (0.22). Nollert et al (Nollert, Kiefer et al. 1995) have described two outcomes when liposomes adsorb to surfaces. In the first, liposomes adsorb but do not rupture. As a result, they produce an immobile fraction because the fluorescently tagged lipids cannot freely migrate between liposomes. In the other scenario, liposomes adsorb, rupture and spread to form sBLMs. Therefore, the higher μ values observed on PAH suggest that adsorbed liposomes more readily ruptured to form a

bilayer on PAH than on PDAC. Similar results have been reported in a previously published AFM study which showed that liposomes composed of DOPA adsorb onto a PDAC-coated surface, but most remain intact (Luo, Liu et al. 2001). On the other hand, liposomes form a continuous sBLM on substrates coated with PEI, which is a weak polyelectrolyte like PAH. However, other feasible mechanisms could also explain the trends seen in Table 5.1. For instance, lipids adsorbed onto PDAC may form disconnected bilayer patches.

The diffusion coefficients obtained in this study are comparable to those reported for BLM containing SOPS and POPC deposited on PDAC/SPS multilayers (0.2×10^{-8} cm²/s) (Zhang, Longo et al. 2000; Ma, Srinivasan et al. 2003). Our values are, however, lower than those reported for DMPC:DOPA (10:1) BLM deposited on SPS/PAH multilayers (Cassier, Sinner et al. 1999). In our system, the dye molecules were present in both the upper and lower leaflet. However, in the reported systems (Cassier, Sinner et al. 1999) the dye molecule is present only in the upper leaflet and thus they are measuring the diffusion coefficient only of the upper leaflet. The upper leaflet would be less influenced by the underlying substrate and thus would be expected to exhibit a higher diffusion coefficient than the bottom leaflet. Moreover, in our study, NBD was attached to one of the hydrophobic tails of phosphocholine; Cassier et. al. have reported that diffusion coefficients can increase by a factor of four if the NBD molecule is attached to the head-group than to the tail of the phosphocholine molecule (Cassier, Sinner et al. 1999).

5.4.4 Characterization of liposome adsorption and rupture by QCM

QCM analysis has been used effectively to study both kinetics of liposome adsorption and subsequent liposome fusion to form a bilayer (Ohlsson, Tjarnhage et al. 1995; Keller and Kasemo 1998; Graneli, Rydstrom et al. 2003). Adsorption of material onto a QCM chip results in a decrease in the chip's oscillating frequency. Under ideal conditions, there is a linear relationship between the change in the resonant frequency (Δf) of the QCM chip, and the change in mass (Δm) due to adsorption:

$$\Delta m = C \frac{\Delta f}{n} \quad (4.7)$$

where C is the mass sensitivity of the crystal, and n is the overtone number.

The Δf curve corresponding to sBLM formation on silicon dioxide has been shown to have two distinct phases (Keller and Kasemo 1998): (1) adsorption of intact liposomes, and (2) liposome rupture and bilayer formation. When adsorbed liposomes rupture, water trapped inside and between them is released, resulting in a loss of adsorbed mass. Thus, Phase 1 is characterized by an increase in mass (decrease in f), and Phase 2 is characterized by a subsequent decrease in mass (increase in f). There is no net measurable dissipation shift for BLM formation, as a completely formed sBLM is very compact and couples strongly to the motion of the QCM crystal. On the other hand, intact liposome adsorption is characterized by large dissipation shifts, as adsorbed liposomes are substantially larger and less compact structures. Thus, liposomes can be subjected to large deformation under shear stress, resulting in increased energy dissipation.

Figures 5.11a (Curve i) and 5.11b (Curve iii) show the Δf curves for liposome interactions with a QCM chip coated with PEMs having PDAC and PAH as the topmost layer, respectively. Neither curve exhibits two distinct phases, suggesting that BLM formation on PDAC and PAH does not follow the two-phase process reported for silicon dioxide (Keller and Kasemo 1998). The Δf value measured on PDAC ($-95 \text{ Hz} \pm 10 \text{ Hz}$) lies between $-26 (\pm 4) \text{ Hz}$ and $-110 (\pm 10) \text{ Hz}$, values generally observed for a completely formed bilayer and for intact liposomes of similar size, respectively. This result, and also the large dissipation shift (4.5×10^{-6}) corresponding to liposome adsorption (Figure 5.11a Curve ii), suggest that most of the liposomes on PDAC remain intact and don't rupture to form a bilayer. The previously described FRAPP results on PDAC, which showed about 22% mobile fraction, are also consistent with this hypothesis.

In contrast, liposome adsorption on PAH (Figure 5.11b) resulted in a comparatively smaller frequency change (Curve iii, $-45 \text{ Hz} \pm 10 \text{ Hz}$) and dissipation shift (Curve iv, $1.2 \times 10^{-6} \pm 0.1 \times 10^{-6}$). These results, together with the FRAPP results, which showed about 68% mobile fraction on PAH, suggest that most of the liposomes on PAH fused to form a BLM.

The results presented above indicate that this novel method offers several advantages over previously reported methods used to create sBLM microarrays. The use of μCP affords precise control over the 2-D geometry of the array at the micron (and potentially sub-micron) scale. The use of a PEM layer between the underlying surface and the biomimetic interface adds versatility, because PEM can be adsorbed to virtually any surface and because the PEM layer could serve as a hydrophilic reservoir needed for

some membrane proteins to function properly. This approach also provides greater control over the physical and chemical properties of the biomimetic interface, because (1) the thickness of the PEM reservoir can be controlled with nanometer precision via the number of polyelectrolyte layers deposited, (2) the diverse range of PEMs available allows the chemical properties of the reservoir to be customized, (3) the strength of liposome deposition can be controlled, based on charge or the use of m-dPEG acid, and (4) the degree to which adsorbed liposomes rupture to form BLM can be controlled via the chemical properties of the top polyelectrolyte layer.

5.5 CONCLUSIONS

We have developed an approach for fabricating arrays of BLMs and liposomes on PEMs that entails (1) establishing a patterned microarray of PEM and/or m-dPEG acid on a surface and (2) selectively depositing liposomes on either the features or the background of the pattern. TIRFM and fluorescence microscopy results indicated that liposomes composed of DOPA and DOPC adsorb strongly on PDAC and PAH surfaces but only weakly on SPS and poly(ethylene glycol) (m-dPEG acid) coated surfaces. We exploited these tendencies to create clean, patterned microarrays of BLMs and liposomes on PAH and PDAC. The mechanism of liposome rupture and bilayer formation is not yet fully understood. However, FRAPP and QCM results suggest that a higher fraction of liposomes rupture to form bilayers on PAH surfaces than on PDAC, where a significant percentage of the adsorbed lipids are essentially immobile.

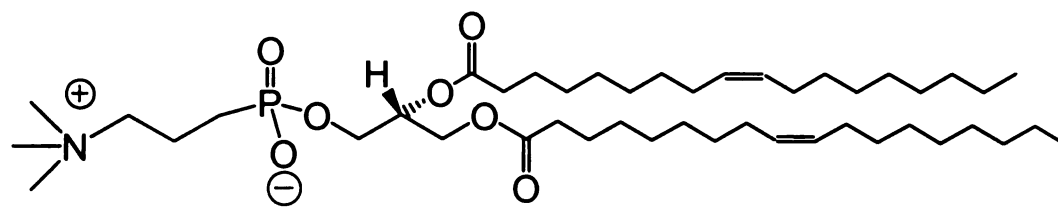
The versatility of the approach is illustrated by its unique ability to form clean microarrays in both positive and negative image of the μ CP stamp. Potential

applications include novel biosensors and biocatalysts, microarrays for high-throughput screening of compounds that interact with cell membranes, and micropatterned interfaces to study, and possibly controlling, interactions between living cells and synthetic membranes.

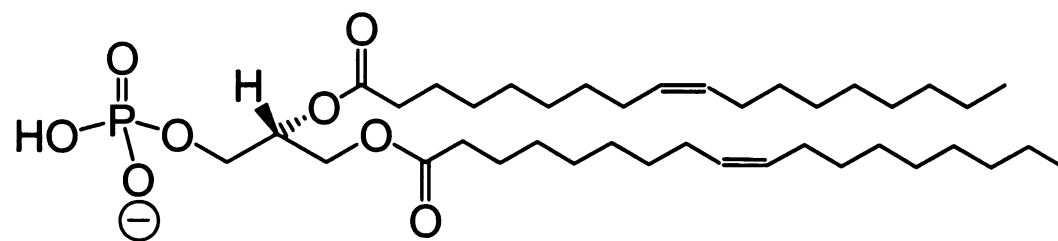
5.6 RECOMMENDATIONS FOR FUTURE WORK

One possible study for examining liposome rupture and bilayer formation on charged, PEM-coated surfaces involves making epi-FRAP measurements on liposomes that adsorb to the PEMs in the presence of an electric field. The presence of the electric field can alter the conformation of the charged PEMs, possibly altering the surface characteristics and liposome rupture. Such a study would elucidate the underlying mechanisms for liposome rupture and bilayer formation, and provide insight to tune the surface characteristics to optimize it for BLM deposition. Another interesting method to study vesicular fusion and rupture is using fluorescence resonance energy transfer (FRET), the radiation-less energy transfer from a donor molecule to an acceptor molecule. The amount of energy transfer is dependent on the extent of overlap between the emission spectrum of the donor and the absorption spectrum of the acceptor. This rate of energy transfer varies inversely with the 6th power of the distance between the donor and the acceptor (Lakowicz 1983). FRET has been used for studying the mechanism of initial rupture of liposomes using single vesicle fluorescence assays (Johnson, Ha et al. 2002). It would be useful to probe the mechanism of liposome rupture on the highly charged polyelectrolyte substrates using such assays.

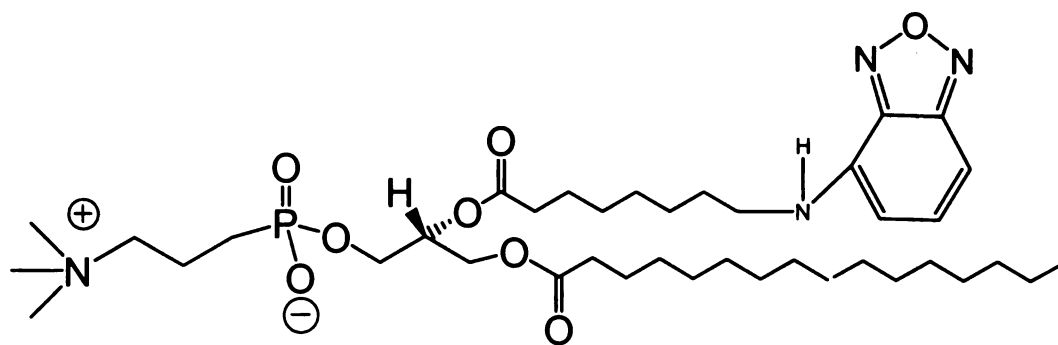
It would also be helpful to characterize liposome adsorption under a multitude of flow rates and ionic strengths to examine the shape of the adsorption profile, since the ionic strength of the solution will have a strong influence on polyelectrolyte structure of the highly charged polyelectrolytes. In addition, this study would provide insight into multi-bilayer membrane formation.



(a)

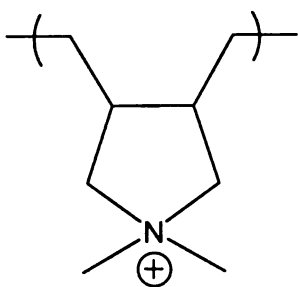


(b)

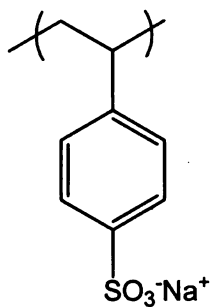


(c)

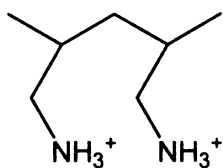
Figure 5.1: Structure of (a) DOPC, (b) DOPA, (c) NBD-PC



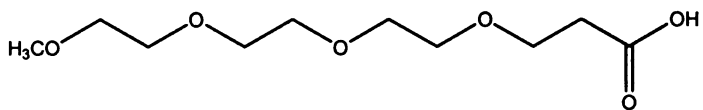
(a)



(b)



(c)



(d)

Figure 5.2: Structures of (a) PDAC, (b) SPS, (c) PAH, and (d) m-dPEG acid.

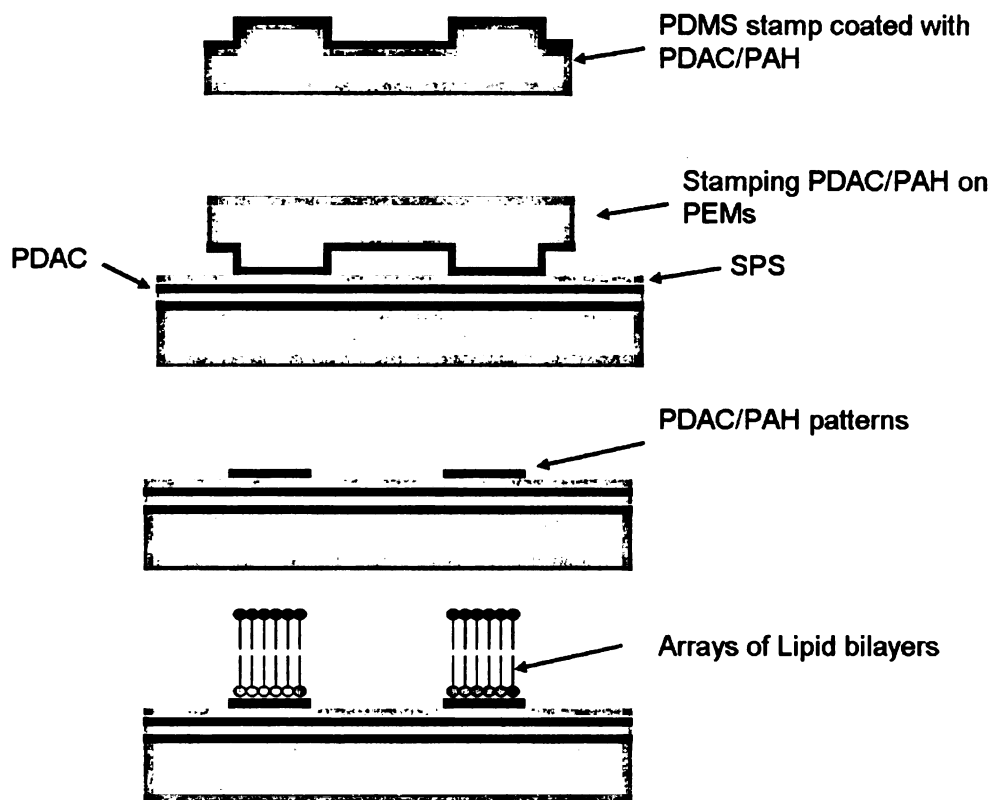


Figure 5.3: Schematic representation of the process for the fabrication of arrays of BLMs on PDAC and PAH patterned substrates.

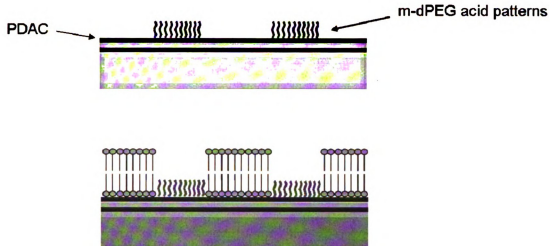


Figure 5.4: Schematic representation of the process for the fabrication of arrays of BLMs on m-dPEG acid patterned substrates.

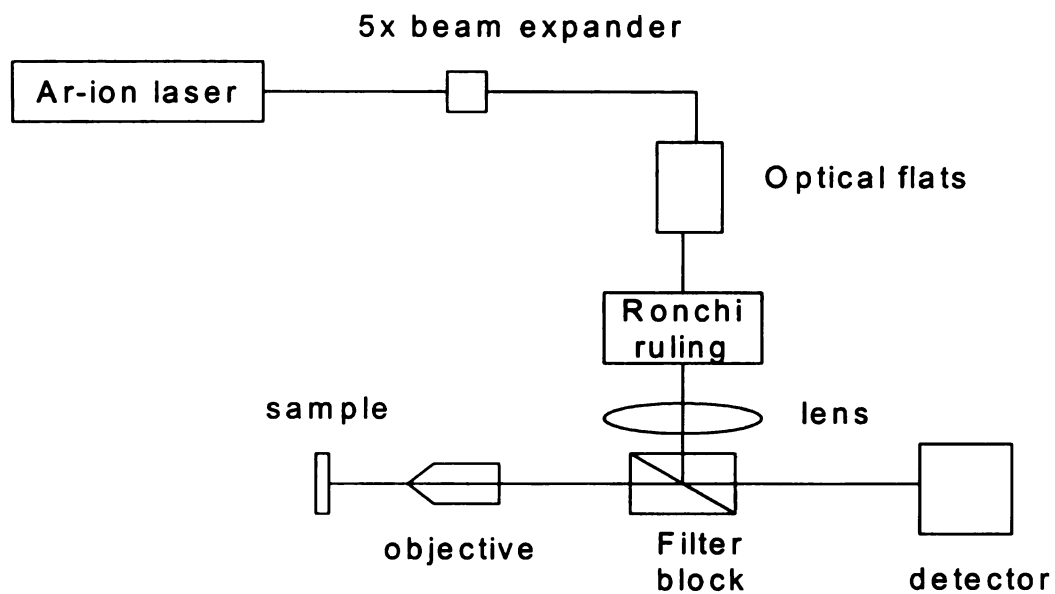


Figure 5.5: Experimental set-up for fluorescence recovery after pattern photobleaching using EPI-illumination.

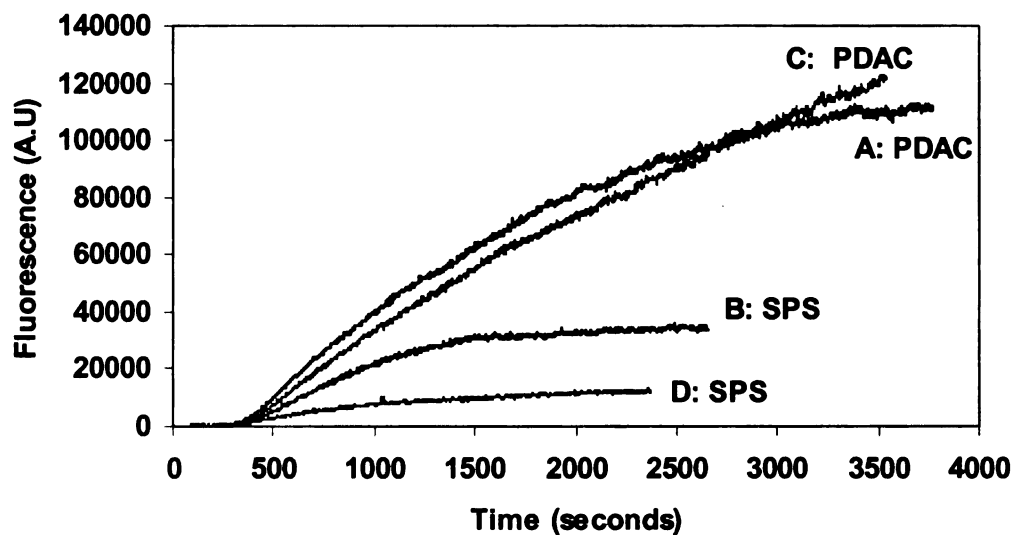


Figure 5.6: Adsorption curves of (A) liposomes (10% DOPA, 90% DOPC) on PDAC. (B) liposomes (10% DOPA, 90% DOPC) on SPS. (C) liposomes (20% DOPA, 80% DOPC) on PDAC. (D) liposomes (20% DOPA, 80% DOPC) on SPS.

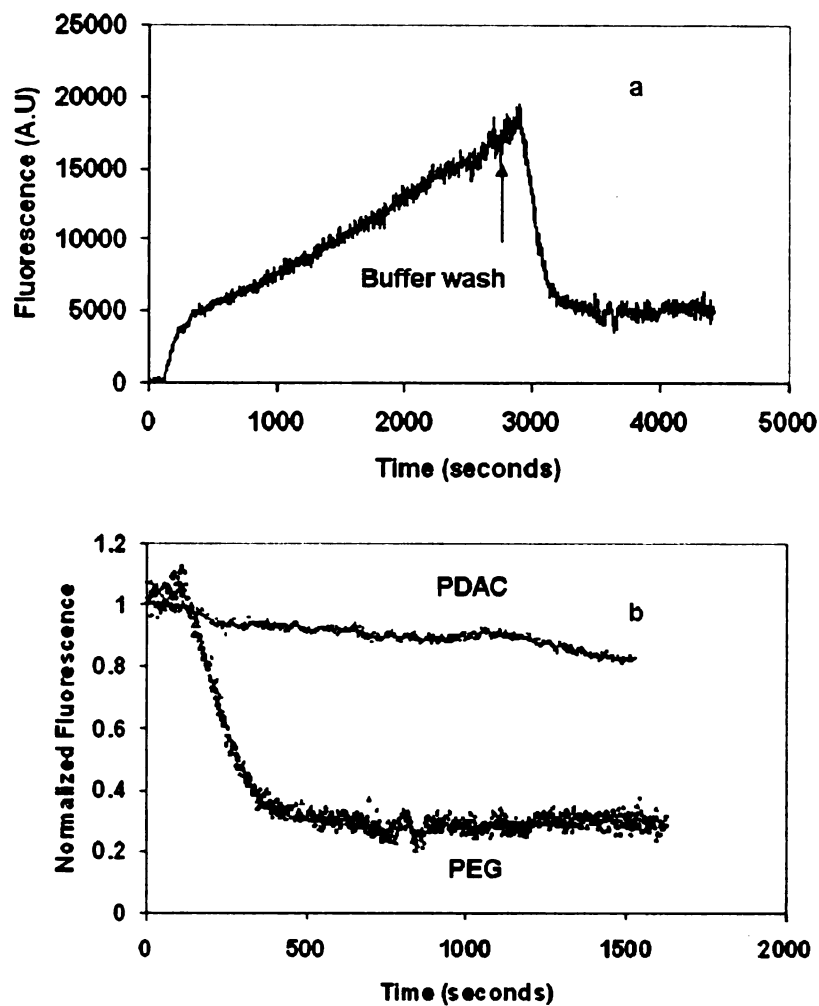


Figure 5.7: a) Adsorption of liposomes (10% DOPA, 90% DOPC) on a glass slide coated with PEMs with m-dPEG acid being the topmost layer. b) Buffer-wash experiments to study liposome desorption from PEMs. The top and bottom curves depict desorption of liposomes from PEMs with PDAC and m-dPEG as the top layer, respectively. At $t=0$, adsorption of liposomes (which have adsorbed for at least 45 min) is halted by introducing liposome-free buffer. In each curve, the fluorescence intensity has been normalized by the corresponding fluorescence value obtained prior to initiation of the buffer wash.

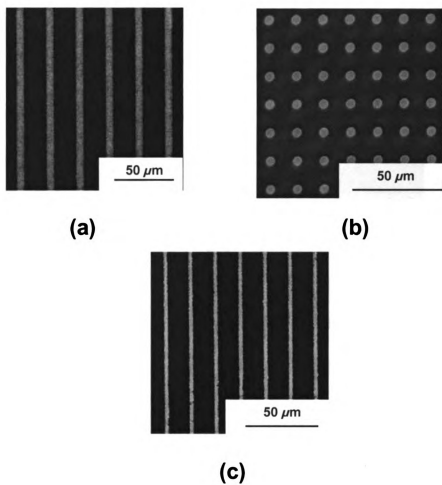


Figure 5.8: Fluorescence images showing (a) line patterns on a PDAC patterned substrate (b) circular patterns on a PDAC patterned substrate (c) line patterns on a PAH patterned substrate.

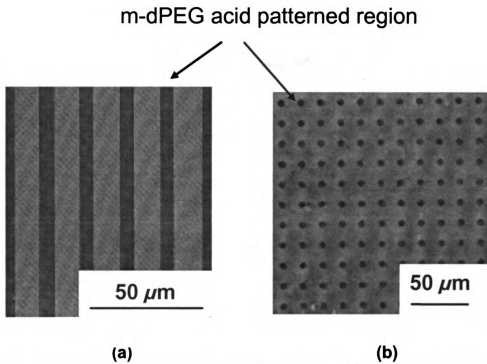


Figure 5.9: Fluorescence microscopy images showing (a) line patterns on m-dPEG acid patterned substrate (b) circular patterns on m-dPEG patterned substrate.

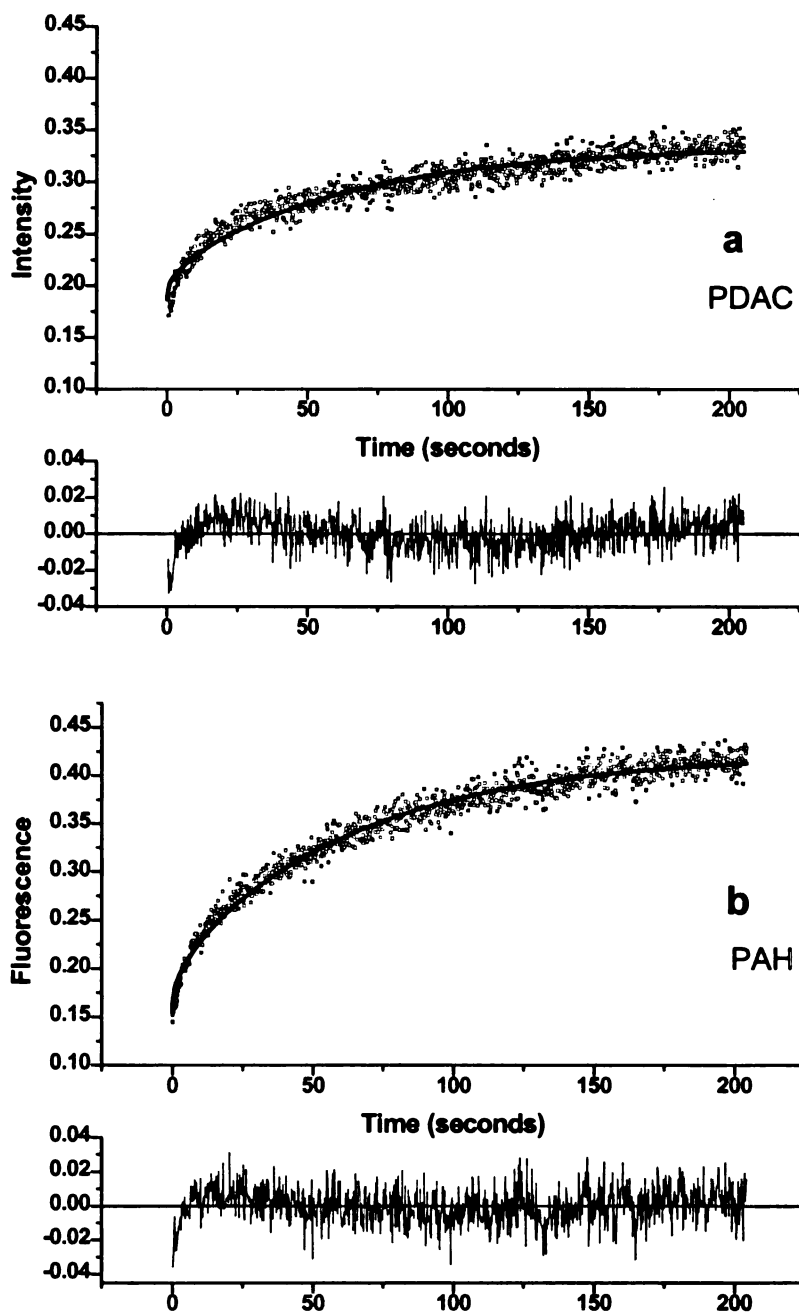


Figure 5.10: Fluorescence recovery after pattern photobleaching (FRAPP) profiles on PEMs with (a) PDAC and (b) PAH as topmost layer. Only post bleach fluorescence intensity normalized against the corresponding pre bleach fluorescence value is shown. The solid lines in the figures represent fits to the recovery data set with models (Wright, Palmer et al. 1988) describing populations with a single mobile fraction and an immobile fraction. Plots of residuals vs. time are also indicated below each figure. Average values obtained with these models are summarized in Table 1

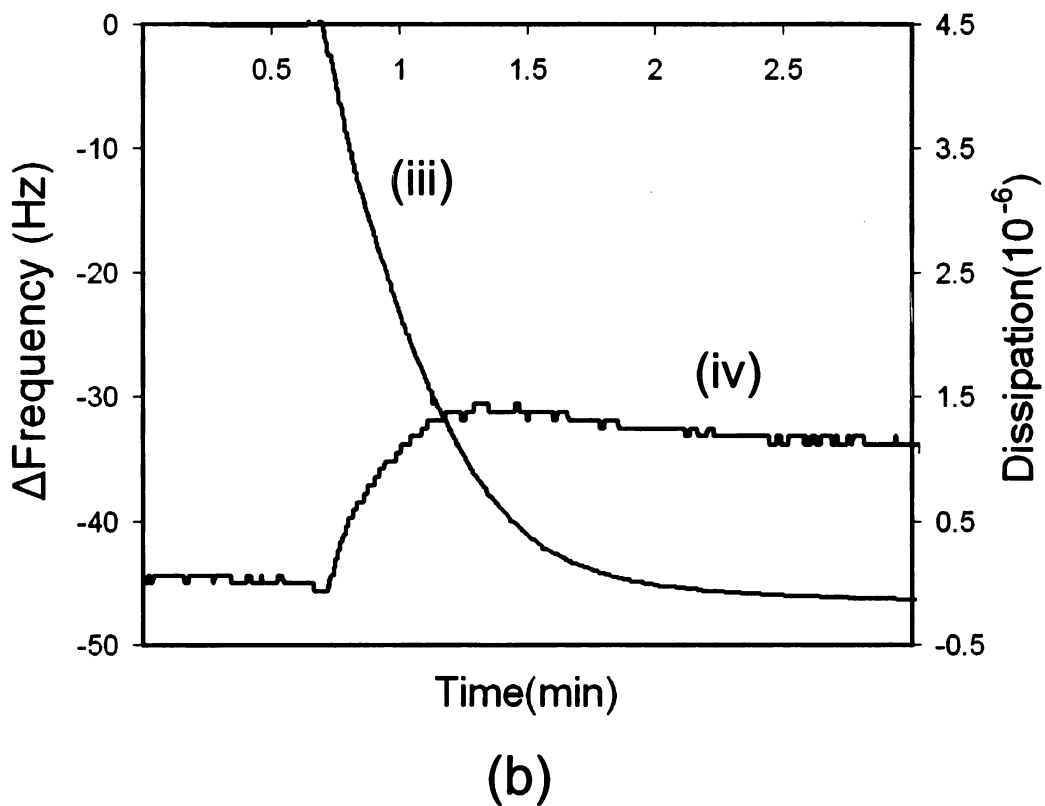
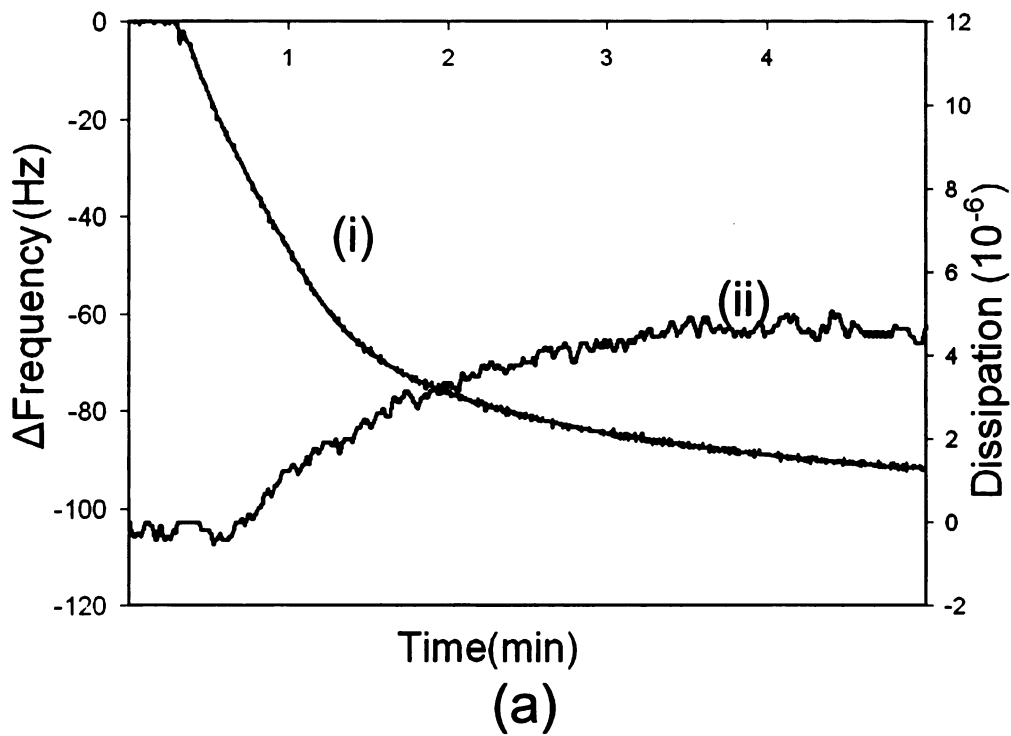


Figure 5.11: Changes in QCM resonant frequency (Curves i and iii) and dissipation (Curves ii and iv) versus time for the adsorption of liposomes on (a) PEMs having a top layer of PDAC (b) PEMs having a top layer of PAH.

Table 5-1: Average lipid diffusion coefficients (D), and average mobile fractions (m) for BLMs formed on PEMs with PDAC and PAH as the topmost layer. The estimates were obtained by averaging parameters fit from all recovery curves.

Substrate	Average diffusion coefficient ($\times 10^{-8} \text{ cm}^2/\text{s}$)		Average mobile fraction	
	PAH	D	0.224 ± 0.01	μ
PDAC	D	0.288 ± 0.03	μ	0.22 ± 0.07

6 TETHERED LIPID BILAYERS ON ELECTROLESSLY DEPOSITED GOLD FOR BIOELECTRONIC APPLICATIONS

6.1 ABSTRACT

This paper presents the formation of a novel biomimetic interface consisting of an electrolessly deposited gold film overlaid with a tethered bilayer lipid membrane (tBLM). Self-assembly of colloidal gold particles was used to create an electrolessly deposited gold film on a glass slide. The properties of the film were characterized using field-effect scanning electron microscopy (FE-SEM), energy dispersive spectroscopy (EDS), and atomic force microscopy (AFM). Bilayer lipid membranes (BLMs) were then tethered to the gold film by first depositing an inner molecular leaflet using a mixture of 1,2-dipalmitoyl-*sn*-glycero-3-phosphoethanolamine-*N*-[3-(2-pyridyldithio)propionate] (DGP), 1,2-di-*O*-phytanyl-*sn*-glycero-3-phosphoethanolamine (DPGP) and cystamine in ethanol onto a freshly prepared electrolessly deposited gold surface. The outer leaflet was then formed by the fusion of liposomes made from DPGP or 1,2-dioleoyl-*sn*-glycero-3-phosphocholine (DOPC) on the inner leaflet. To provide functionality, two membrane biomolecules were also incorporated into the tBLMs: the ionophore valinomycin and a segment of neuropathy target esterase (NTE) containing the esterase domain. Electrochemical impedance spectroscopy (EIS), UV/Visible spectroscopy and fluorescence recovery after pattern photobleaching (FRAPP) were used to characterize the resulting biomimetic interfaces and confirm membrane biomolecule activity. Microcontact printing was used to form arrays of electrolessly deposited gold patterns on glass slides. Subsequent deposition of lipids yielded arrays of tBLMs. This approach can be extended to form functional biomimetic interfaces on a wide range of inexpensive

materials, including plastics. Potential applications include high-throughput screening of drugs and chemicals that interact with cell membranes, and for probing, and possibly controlling, interactions between living cells and synthetic membranes. In addition, the gold electrode provides the possibility of electrochemical applications, including biocatalysis, bio-fuel cells, and biosensors.

6.2 INTRODUCTION

Biomimetic interfaces, consisting of tBLMs with membrane proteins incorporated into them or bound to them, have primarily been used for sensing applications (Raguse, Braach-Maksvytis et al. 1998; Stora, Lakey et al. 1999; Wagner and Tamm 2000; Yin, Burns et al. 2003). Novel approaches that can increase the range of tBLMs applications to include areas such as biocatalysis and biofuel cells are of scientific and commercial interest. Another major challenge in the commercialization of such biomimetic interfaces is the costs involved to produce the gold substrates needed to deposit the tBLM on the electrode. Although methods such chemical vapor deposition (CVD) and physical vapor deposition (PVD) have been used to deposit gold, these methods are very expensive and also suffer from several limitations. Therefore, there is a need for approaches that can help reduce the cost of fabrication of substrates and overcome some of the limitations associated with CVD and PVD.

Electroless deposition is an inexpensive metal-plating technique that can easily be performed on a laboratory bench top and in aqueous solutions (Supriya and Claus 2004; Guan, Chen et al. 2005). Unlike CVD and PVD, it doesn't require any adhesion layer and can be used to tune the properties of arrays or films of metals with nanometer-scale

precision on virtually any surface, including glass, silicon wafers, and mechanically flexible plastics. Due to their high surface area to volume ratio, porous substrates are generally used as electrodes in biocatalytic reactors and biofuel cells. CVD and PVD are expensive and poorly suited to uniformly coating the internal pore surfaces of porous substrates. However, electroless deposition, because of capillary action offers the potential for both coating the internal pores and low processing costs.

Arrays of BLMs on PEMs may be ideal for applications involving membrane proteins that require either a cofactor or mediator for their activity. The cofactors and mediators can be attached or entrapped near the membrane protein using the functional groups on the polyelectrolyte. However, BLMs on PEMs have low impedance; as a result they cannot be used for applications requiring high impedance such as ion channels based studies. On the other hand, tBLMs formed using tethers like PEG have been shown in literature to have high impedance (Raguse, Braach-Maksvytis et al. 1998). Therefore, approaches that can help generate arrays of such tBLMs are of scientific importance.

This chapter presents (Kohli, Hassler et al. 2006) an economical and versatile approach that can easily be extended to fabricate functional and nanostructured biomimetic interfaces on a wide variety of surfaces including electrodes of biocatalytic reactors, thus increasing the repertoire of tBLM based applications. The approach entails combining electroless metal deposition, and molecular self assembly, to sequentially deposit a conductive gold layer and a tBLM on a substrate. The properties of the gold film were characterized using field-effect scanning electron microscopy (FE-SEM), energy dispersive spectroscopy (EDS), and atomic force microscopy (AFM). The fluidity of the tBLM was measured using fluorescence recovery after pattern

photobleaching (FRAPP). The suitability of the interface to maintain membrane proteins or other biomolecules in a functional conformation was shown using the ionophore valinomycin, and a segment of neuropathy target esterase (NTE) containing its catalytic domain (NEST). To further demonstrate the versatility of this approach, microcontact printing was combined with electroless gold deposition and layer by layer to deposit arrays of tBLMs. The resulting arrays were characterized using atomic force microscopy (AFM), field-emission scanning electron microscopy, fluorescence microscopy, and energy dispersive spectroscopy (EDS).

6.3 EXPERIMENTAL SECTION

6.3.1 Materials

1,2-dipalmitoyl-*sn*-glycero-3-phosphoethanolamine-*N*-[3-(2-pyridyldithio) propionate] (DGP, Figure 6.1a), 1,2-dioleoyl-*sn*-glycero-3-phosphocholine (DOPC), 1,2-di-*O*-phytanyl-*sn*-glycero-3-phosphoethanolamine (DPGP, Figure 6.1b) and 1,2-dioleoyl-*sn*-glycero-3-phosphoethanolamine-*N*-(7-nitro-2-1,3-benzoxadiazol-4-yl) (NBD-PE, Figure 6.1c) were purchased from Avanti Polar Lipids (Alabaster, AL). Cystamine, 3-mercaptopropyltrimethoxy silane (MPS), gold chloride trihydrate (HAuCl₄·3H₂O), hydroxylamine, dithiothreitol (DTT), fluorosilanes and sodium citrate dihydrate were obtained from Sigma (St. Louis, MO). Poly (ethylene glycol) PEG-silane 2000 was obtained from Nektar Therapeutics (San Carlos, CA). Sylgard 184 silicone elastomer kit (Dow Corning, Midland, MI) was used to prepare the poly(dimethylsiloxane) (PDMS) stamps for μ CP. Deionized (DI) water was supplied by a Nanopure-UV four-stage

purifier (Barnstead International, Dubuque, IA); the purifier was equipped with a UV source and a final 0.2 μm filter. All aqueous solutions were prepared using DI water.

6.3.2 Preparation of stamps

The PDMS stamps were made by pouring a 10:1 (w/w) solution of elastomer and initiator over a pretreated silicon master, which acts as a mold, to allow the surface morphology of the stamp to form a negative replica of the master. The silicon master was pretreated with fluorosilanes to facilitate the removal of the PDMS stamps. The mixture was allowed to cure overnight at 60 °C and then peeled off. The masters were prepared in the Keck microfabrication facility at MSU and consisted of features (parallel lines and circles) from 1 to 20 μm .

6.3.3 Synthesis of colloidal gold particles

106 mL of 2.2 mM aqueous sodium citrate was rapidly boiled in a flask, and 1 mL of 24.3 mM $\text{HAuCl}_4 \cdot 3\text{H}_2\text{O}$ was rapidly added under vigorous stirring. The solution was boiled for 15 min, cooled to room temperature, and stored at 4 °C. (Supriya and Claus 2004)

6.3.4 Formation of gold film and patterns by electroless deposition

The gold films were fabricated as illustrated in Figure 6.2 using a variation of the method reported by Frens (Frens 1973; Supriya and Claus 2004). Glass slides were cleaned in piranha solution (7 parts by volume concentrated H_2SO_4 , and 3 parts 30% (v/v) H_2O_2) then washed with DI water and dried under nitrogen. The slides were dipped into a 1% (v/v) solution of MPS in methanol for 10 min with stirring, rinsed with

methanol, and heated to 110 °C for 2 h to complete the silanization. The surface-modified slides were then immersed in colloidal gold solution at room temperature (22 °C ± 1°C) for 2 h to allow thiol bonds to form between gold nanoparticles and sulfur groups. The slides were then rinsed with DI water and immersed in 200 mL of aqueous solution containing 2.6 mg of hydroxylamine and 20 mg of H₂AuCl₄·3H₂O under constant agitation for 30 min. This step, called seeding, resulted in chemical reduction of gold ions onto the immobilized gold nanoparticles. The seeding process was repeated three times to achieve a continuous, conductive film.

To obtain gold patterns (Figure 6.3), a PDMS stamp was dipped into 1 mM solution of MPS in ethanol for 5 min. The stamp was washed with absolute ethanol, dried under nitrogen, and brought into contact with a glass slide. The stamp was removed after 2 min, and the resulting MPS patterned slide was washed with ethanol to remove loosely bound MPS. The slide was heated to 110°C for 2 h and immersed in colloidal gold solution. The patterned slide was then sonicated in DI water for 10 min to remove loosely bound gold particles from the background of the glass slides. The gold-particle-patterned slide was then exposed to the seeding solution for 30 min three times to create gold patterns.

6.3.5 Preparation of liposomes for fluorescence and electrochemical measurements

For fluorescence experiments, small unilamellar liposomes (~ 20 ± 5 nm) were prepared by adding 20 mg of DPGP and 0.2 mg of NBD-PE in 1 mL of chloroform. This mixture was then dried under nitrogen, making sure the lipid formed a thin cake-like film on the walls of the test tube. The residual chloroform was removed under high vacuum. The

lipids were then reconstituted in 20 mL of 0.1 M aqueous NaCl solution, and the resulting liposome solution was sonicated with a Bransonic bath sonicator (Branson Ultrasonics Corporation, Danbury, CT) until it became clear. Liposomes were prepared in the same way for electrochemical experiments, except no NBD-PE was added. The liposome size was determined using Coulter N4 MD Particle Size Analyzer (Coulter Electronics Inc., Hialeah, FL)

6.3.6 Formation of tBLMs containing valinomycin

The inner leaflet of the tBLM was formed by dipping a freshly prepared electrolessly deposited gold slide into an ethanolic solution of 1 mM DGP, 1 mM DPGP, and 500 μ M cystamine for 2 h. The slide was washed with absolute ethanol and dried under nitrogen. The modified slide was dipped in liposome solution (1 mg/mL) for 45 min and washed with 0.1 M aqueous NaCl solution to obtain the outer leaflet.

An ethanolic stock solution of valinomycin (2 mg/mL) was diluted in the aqueous solution to obtain a valinomycin concentration of 5×10^{-7} M and allowed to equilibrate for 1 h at room temperature. No change in impedance was observed on valinomycin insertion in this aqueous solution (0.1 M NaCl). However, the impedance dropped when this solution was replaced with another solution containing 0.05 M NaCl and 0.05 M KCl, providing evidence of the insertion and activity of this potassium-selective ionophore into the tBLM.

6.3.7 Formation of NEST-containing liposomes (NEST-DOPC liposomes)

NEST was expressed and purified according to published procedures (Atkins and Glynn 2000). For incorporation into liposomes, NEST solution (0.1 mg/mL) in PEN buffer (50

mM phosphate buffer, 0.5 mM EDTA and 300 mM NaCl) containing 0.3% (w/v) CHAPS was mixed with DOPC (10 mg/mL in 9%(w/v) CHAPS) in 1:4 ratio (protein wt:DOPC wt) and dialyzed against 500 volumes of PEN buffer containing 1 mM DTT overnight. (Atkins and Glynn 2000)

6.3.8 Preparation of phenyl valerate micellar suspension

To prepare phenyl valerate solution, 15 mg of phenyl valerate was dissolved in 1 ml of dimethylformamide (DMF), and 15 ml of water containing 0.03% Triton was added slowly under stirring.

6.3.9 Formation and characterization of NEST-containing tBLMs

The inner leaflet of the lipid bilayer was formed as described above. The NEST-DOPC liposome solution was pumped across the inner leaflet at a rate of 0.34 mL/min for 12 min using a syringe pump. Flow was then halted, and adsorption was allowed to continue for approximately 1 h. Five to six flow cell volumes of PEN buffer were then passed through the system to remove the liposomes in the bulk solution. Further details regarding the setup and design of the flow cell can be found in a previous publication (Gajraj and Ofoli 2000).

To measure NEST activity in the tBLM, the PEN buffer in the flow cell was replaced with a micellar suspension of phenyl valerate and allowed to react with the NEST-containing tBLM for 20 min. The resulting suspension was collected, and the amount of phenol produced was measured according to published procedures (Kayyali, Moore et al. 1991; Atkins and Glynn 2000). Briefly, 400 μ L of resulting suspension was mixed with 400 μ L of 1.23 mM 4-aminoantipyrine containing 3.8 mg of sodium dodecyl

sulfate and allowed to react for 5 min. To develop color, 200 μL of 12.1 mM potassium ferricyanide solution was then added to this solution, and after 5 min the absorbance (A) at 486 nm was measured. The spectrophotometer was blanked using suspension obtained in the same way, except the phenyl valerate suspension was treated with a tBLM containing no NEST protein. The amount of phenol produced was determined from the absorbance using a calibration plot depicting A_{486} as a function of known phenol concentrations.

6.3.10 Arrays of lipid bilayers

To obtain arrays of tBLMs, a gold-patterned glass slide was dipped in 1 mM solution of PEG-silane 2000 in absolute ethanol for 20 min, rinsed with absolute ethanol, and heated at 120 °C for 2 h to bind PEG-silane to the exposed glass background of the array. The bottom leaflet of the tBLM was deposited on the gold features as described above. The top leaflet was then added by dipping the modified slide in liposome solution for 45 min and washing with 0.1 M NaCl solution. Because the PEG-background region resisted liposome adsorption, liposomes adsorbed only on the modified gold patterned region.

6.3.11 Electrochemical impedance spectroscopy (EIS) measurements

Impedance measurements were done using an electrochemical analyzer (CH 650A, CH Instruments, Austin, TX). The impedance spectrum was obtained by sweeping an applied potential of 50 mV from 10^{-1} Hz to 10^4 Hz, superimposed on a DC offset of 0 V. A three-electrode configuration was used with a Ag/AgCl reference electrode, a platinum counter electrode, and a modified gold working electrode having an area of 0.16 cm^2 .

Commercially available software (Z-view, Scribner Associates, Southern Pines, NC) was used to fit electrical circuit models to the impedance spectra.

6.3.12 Fluorescence recovery after pattern photobleaching (FRAPP)

Liposomes were adsorbed on the electrolessly deposited gold substrates by causing the liposome solution to flow over them at a rate of 0.34 mL/min for 10-12 min using a syringe pump. The infusion was then halted, and liposome adsorption was allowed to continue for approximately 1 h. The flow cell (Gajraj and Ofoli 2000) was subsequently flushed with four to five flow cell volumes of 0.1 M NaCl to remove the remaining liposomes in the bulk solution and FRAPP measurements were performed. All experiments were done at room temperature, which is above the phase transition temperature of DPGP and DOPC (Albrecht, Johnston et al. 1982).

6.3.13 Other measurements

All fluorescence images were obtained with a Nikon Eclipse E 400 microscope (Nikon, Melville, NY) using a filter cube (Ex: 465-495/DM: 505/Em: 515-555). Field-emission scanning electron microscopy (FE-SEM) images and energy dispersive spectroscopy (EDS) images were obtained using a JEOL 6400 V scanning electron microscope (JEOL USA, Inc., Peabody, MA) equipped with a Noran EDXS detector. Atomic force microscopy (AFM) images were obtained with a Nanoscope IV multimode scope (Digital Instruments, Santa Barbara, CA) using etched silicon probes in tapping mode. The thickness of the patterned arrays was determined using cross-sectional analysis of the AFM images.

6.4 RESULTS AND DISCUSSIONS

6.4.1 Formation of gold films

Figure 6.4a shows a FE-SEM image of a monolayer of gold nanoparticles on a glass slide. The particles were initially not in contact, so the interface was not conductive. Grabar et al. studied adsorption of gold particles on MPS-coated glass slides and concluded that the particle coverage is controlled initially by diffusion, and at later times by interparticle repulsion (Grabar, Smith et al. 1996). Colloidal gold particles derived from $[\text{AuCl}_4]^-$ have a negative charge resulting from strongly adsorbed Cl^- and/or $[\text{AuCl}_2]^-$ produced by incomplete reduction of $[\text{AuCl}_4]^-$. This interparticle repulsion prevents the close packing of colloidal gold on the surface.

However, the gold coverage was increased by the seeding step, as shown in Figure 6.2 and Figure 6.4(b-d). The rate of Au^{3+} reduction on the immobilized gold particles greatly exceeds that in the seeding solution; thus, little new nucleation occurs in the solution, and virtually all of the reduced Au is used to grow the gold particles. (Supriya and Claus 2004) The FE-SEM images in Figure 6.4(b-d) show the growth of gold film on a glass slide following each successive seeding step. The final gold film had a root mean square (RMS) roughness of around 10 nm (data not shown). For comparison, a smooth glass slide, a frosted glass slide, and a gold-sputtered silicon wafer have RMS roughnesses of about 0.6, 14, and 4 nm, respectively (Tristram-Nagle, Petrache et al. 1998; Naumann, Schiller et al. 2003).

6.4.2 Functional tBLMs containing valinomycin

Figure 6.5a depicts the spatial organization of the molecules that make up the tBLM. The mobile lipid, DPGP, (Figure 6.1b), forms the bulk of the BLM. The hydrophilic portion of the reservoir lipid DGP, Figure 6.1a, establishes the ionic reservoir between the BLM and the gold surface. The hydrophobic portion of the reservoir lipid embeds in the BLM, tethering it to the gold surface. The bulky thiobenzyl moiety of the tethering lipids not only binds the lipid to the gold, but also increases the lateral spacing between adjacent reservoir lipid molecules. Cystamine competes with the thiobenzyl group for surface binding sites on the gold, and thus it provides a means to further control the spacing between the reservoir lipids.

Figure 6.5b (curve i and ii), shows Bode plots of tBLM in the absence and presence of valinomycin, respectively, in aqueous solution containing 50 mM KCl/50 mM NaCl. BLMs provide an excellent barrier to ions. Introduction of the K^+ -selective ionophore valinomycin into BLM imparts a valinomycin-mediated transmembrane K^+ flux, making it possible to confirm the functionality of valinomycin-containing BLM by measuring differential impedance to potassium and sodium ions.

Figure 6.5c depicts the electrical analogue model generally used to describe tBLM systems. In this model, the membrane capacitance (C_m) is bypassed by a variable ohmic resistance (R_m), which represents the ionophore-mediated ion flux and any background ion leakage. The membrane capacitance is in series with an effective interfacial capacitance, C_{dl} , which includes the Helmholtz and diffuse capacitances. The model

parameters calculated by Z-view software to fit the data in Figure 6.5b (curve ii) were $C_m = 0.59 \mu\text{F}/\text{cm}^2$, $C_{dl} = 3.9 \mu\text{F}/\text{cm}^2$, and $R_m = 46 \text{ K}\Omega \text{ cm}^2$.

The C_{dl} value in the assembled bilayer system was found to be smaller than the published interfacial capacitance of a gold surface ($\sim 20\text{-}30 \mu\text{F}/\text{cm}^2$), possibly because of the presence of thiobenzyl groups and cystamine molecules partially blocking the surface, or because the tether organizes the water in the reservoir region such that the dielectric constant within the reservoir region is lower than that of the bulk aqueous solution. (Raguse, Braach-Maksvytis et al. 1998) The value of C_m ($0.59 \mu\text{F}/\text{cm}^2$) compared well with the values generally reported for BLM ($\sim 0.5 \mu\text{F}/\text{cm}^2$). Additional evidence for the formation of a functional BLM on electrolessly deposited gold films is provided by the decrease in R_m upon the insertion of valinomycin (Figure 6.5b, curve ii), as indicated by the change in slope at around 10 Hz instead of at around 5 Hz (Figure 6.5b, curve i) for a lipid bilayer containing no ion channel. The impedance increased again (data not shown) when the aqueous solution (50 mM KCl/50 mM NaCl) was replaced with a solution (100 mM NaCl) containing no KCl. These results provide strong evidence that the valinomycin is embedded in an active conformation in an intact tBLM.

6.4.3 Functional BLM containing NEST protein

The phenyl valerate assay was used to confirm whether tBLMs could immobilize NEST in a functional conformation. Incubation of phenyl valerate with NEST-containing BLMs on gold resulted in the production of about 2 ± 0.19 nmol/min of phenol over an area of 1 cm^2 . Incubation of phenyl valerate with NEST-DOPC liposomes in solution

resulted in the production of 40 ± 1.2 nmol/min of phenol per μg of NEST protein. This result suggests the immobilization of approximately 50 ng/cm^2 of active NEST in tBLMs. To our knowledge, this is the first time NEST has been immobilized in an active conformation on a lipid bilayer.

6.4.4 BLM fluidity measurement using FRAPP

Figure 6.6 shows the fluorescence recovery curve for a DGP-DPGP-cystamine modified gold slide contacted with fluorescently labeled liposome solution. Fluorescence recovery was adequately described by a single mobile species model described in Chapter 5, which assumes only one population of diffusive fluorophores in addition to an immobile fraction. Equation 5.6 was fitted to the FRAPP data, and average best-fit values of D ($0.48 \times 10^{-8} \pm 0.055 \times 10^{-8} \text{ cm}^2/\text{sec}$) and m (0.87 ± 0.096) were obtained. These values compare well with published values for tBLM. (Munro and Frank 2004)

These results provide strong evidence that the preponderance of the surface is covered by a tBLM. If the surface were covered primarily by unruptured liposomes, extremely low D and m values would be expected, because fluorescently tagged lipids would not transfer freely between adjacent liposomes.

6.4.5 Fabrication and characterization of gold patterns

Figures 6.7a and 6.7b show circular and line gold patterns, respectively, on a glass slide. The lighter features show regions that were in contact with the stamp and are thus covered with gold. The well-defined features of the patterns and the clean background suggest negligible adsorption of gold particles on the background glass slide.

EDS was also used to confirm selective gold deposition on the patterned regions. In this technique, the area of interest is bombarded with an electron beam of high energy (~10 KeV), causing release of X-rays, the wavelengths of which are characteristic of the elements in that region. Figures 6.8a and 6.8b show that Region 1 (MPS patterned region) has a gold peak, but Region 2 (background glass slide) does not. These results confirm that gold particles adsorb selectively on the MPS-patterned region. Because the penetration depth of the electron beam is around 10 μm , X-rays from the underlying glass substrate are also collected by the detector. As a result, peak related to Si can be seen in both figures. Peaks due to other elements generally present in the glass, such as O, Ca and Al, are not observed, because X-rays associated with these elements lie outside the energy range shown.

Figure 6.9a shows an AFM image of gold patterns. The light areas are deposited gold regions, while dark areas are the underlying substrate. Figures 6.9b and 6.9c show the 3-D image and topographical image, respectively, of the resulting patterns. The gold regions had an average height of 55 ± 7 nm and average RMS roughness of 10 nm.

6.4.6 Fabrication of tBLM arrays

PEG coatings have been shown to resist the adsorption of cells as well as macromolecules, such as proteins and polyelectrolytes, through a mechanism that is believed to stem either from steric exclusions between the biomolecule and the PEG chain (Harris 1992) or from long-range electrostatic repulsions (Feldman, Hahner et al. 1999).

Figure 6.10 shows the fluorescence image of tBLM line patterns. The sharp contrast and clean boundaries between the fluorescent line features and the nonfluorescent background regions, as expected, indicate that fluorescent liposomes bound strongly to the tethering layer (gold patterned region) but not the PEG-coated background region.

While the above-mentioned studies were done on electrolessly deposited gold films on a glass slide, we were also successful in forming electrolessly deposited gold films on mechanically flexible substrates, such as plastics, using negatively charged polyelectrolytes and amine-terminated positively charged polyelectrolytes (data not shown).

6.4.7 Significance of results and potential applications

Collectively, the results of this study represent an important milestone toward development of products and processes based on the activities of membrane proteins or other biomolecules. The FE-SEM, EDS and AFM studies confirmed electroless deposition of gold on an inexpensive substrate (e.g., glass) and showed that the thickness of the gold layer can be controlled. The FRAPP and EIS results showed that silanization, electroless gold deposition, and molecular self-assembly of lipids can be combined to form tBLM on the electrolessly deposited gold. The results with valinomycin and NEST indicated that an ionophore and a fragment of a membrane protein can be bound to the tBLM in an active conformation, so that the activities of these biomolecules can be expressed and measured. The array results indicated that discrete units of the tBLM can be deposited as a high-density microarray that could potentially be used for high-

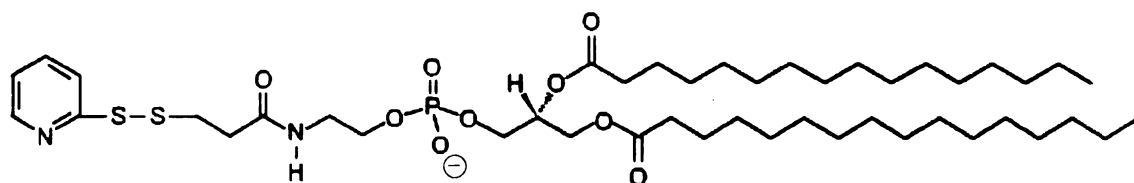
throughput studies of membrane protein or ionophore function. Ongoing research involves applying the interface described here in devices to characterize the functional properties of membrane proteins and cellular interactions with membrane proteins, drug screening, biosensors, biocatalytic reactors, and biological fuel cells.

6.5 CONCLUSIONS

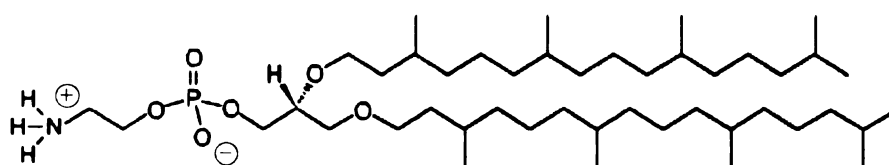
A versatile approach has been developed that can easily be extended to fabricate functional and nanostructured biomimetic interfaces on a wide variety of surfaces. The approach entails sequentially depositing onto the surface a silane layer, a conductive gold layer, a hydrophilic reservoir, and a tBLM. The diffusion coefficient of the tBLMs on electrolessly deposited gold was comparable to that on vapor-deposited gold. Two different classes of membrane biomolecules, the ionophore valinomycin, and the esterase NEST, exhibited their activities when embedded in the tBLM, indicating that the interface can incorporate membrane biomolecules in an active conformation. Because the approach deposits both a conductive gold electrode and a tBLM in close proximity, it can be used for bioelectronic applications, in which the biomolecule's activity is coupled to an electrical signal. Such applications include devices to characterize the functional properties of membrane proteins, biosensors, biocatalytic reactors, and biological fuel cells. Because the entire interface can be fabricated using layer-by-layer assembly from different solutions, this approach may allow biomimetic interfaces to be assembled inside microfluidic channels, thus enabling the production of high-density biosensor arrays for high-throughput applications.

6.6 RECOMMENDATIONS FOR FUTURE WORK

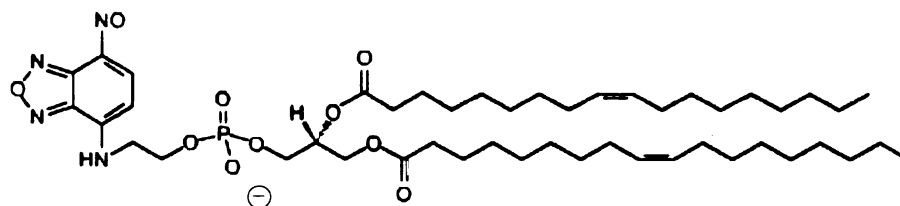
It will be interesting to deposit functional tBLMs on the internal pores of a porous substrate such as alumina. This may be achieved by coating the alumina pores using a low molecular weight, amine terminated polyelectrolyte. Electroless deposition may then be used to deposit gold inside these pores by exploiting the affinity of gold nanoparticles to primary amines. tBLMs may then be formed on the electrolessly deposited gold using the procedure outlined in this Chapter. These tBLMs may be made functional by incorporating membrane proteins having biocatalytic potential such as cytochrome c oxidase. The properties of the modified alumina substrate, as an electrode in a biofuel cell or a biocatalytic reactor, may then be evaluated.



(a)



(b)



(c)

Figure 6.1: Structure of various lipid molecules: (a) DGP (reservoir lipid); (b) DPGP (mobile lipid); (c) NBD-PE.

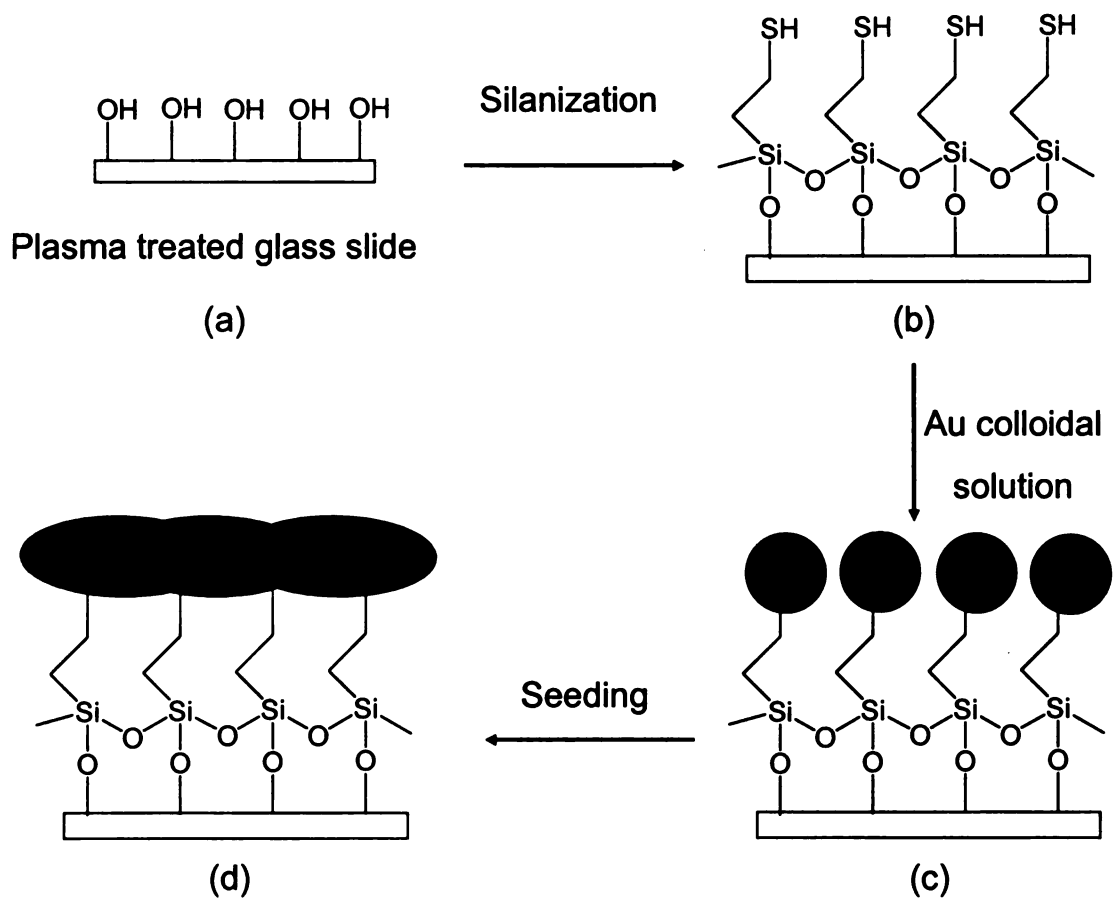


Figure 6.2: Schematic representation of the process for the deposition of Au films: (a) plasma-treated glass slide; (b) slide after silanization with MPS; (c) modified slide after dipping in Au particle solution; (d) formation of conductive Au films after seeding step

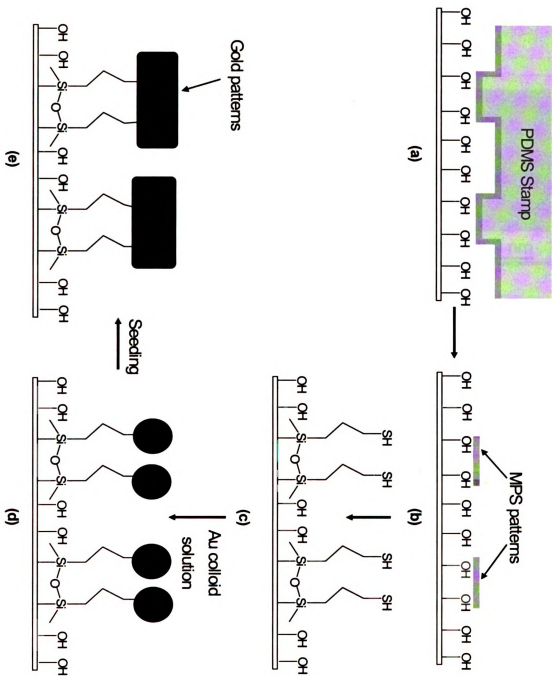


Figure 6.3: Schematic representation of the process for the fabrication of Au patterns: (a) stamping of MPS on a glass slide; (b) MPS patterns on a glass slide; (c) MPS-patterned modified glass slide after heating; (d) MPS-patterned slide after dipping in Au colloid solution; (e) formation of Au patterns after seeding step.

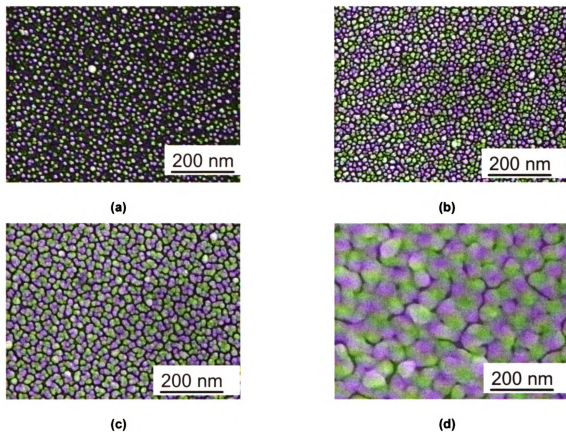
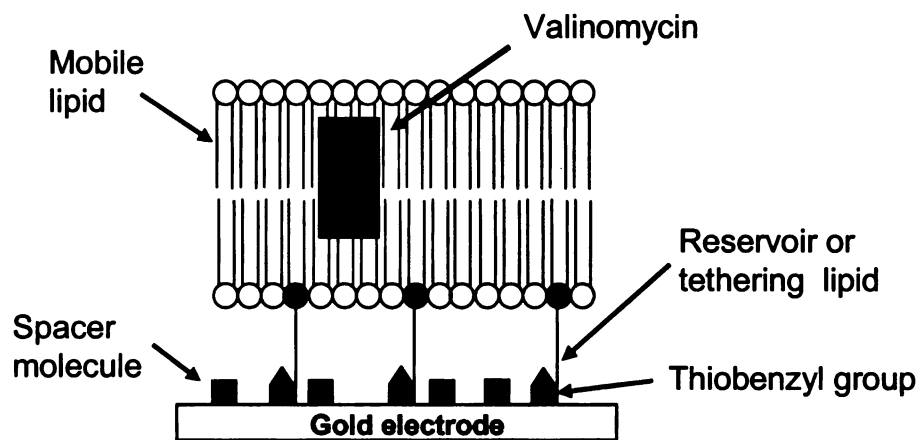
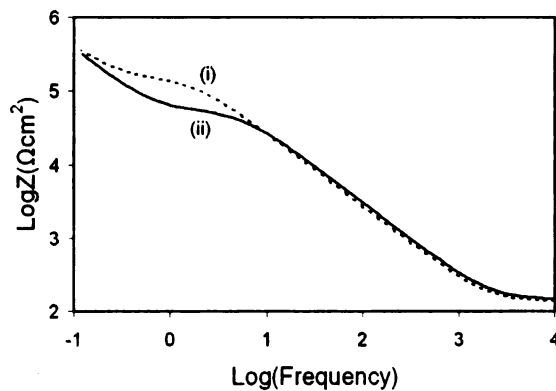


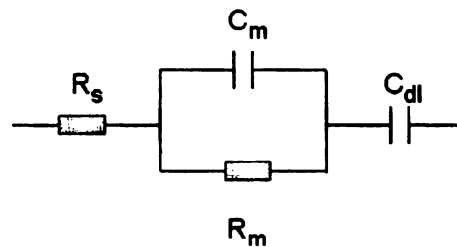
Figure 6.4: FE-SEM images showing the growth of gold on glass slides: (a) after dipping in colloidal solution; (b) seeding once; (c) seeding twice; (d) seeding three times.



(a)



(b)



(c)

Figure 6.5: a) Representation of a tethered bilayer membrane containing an ionophore (valinomycin). (b) Electrochemical spectra in a 50 mM KCl / 50 mM NaCl aqueous solution of a tethered lipid bilayer (curve i), and a valinomycin-containing lipid bilayer (curve ii). (c) Equivalent circuit of a bilayer.

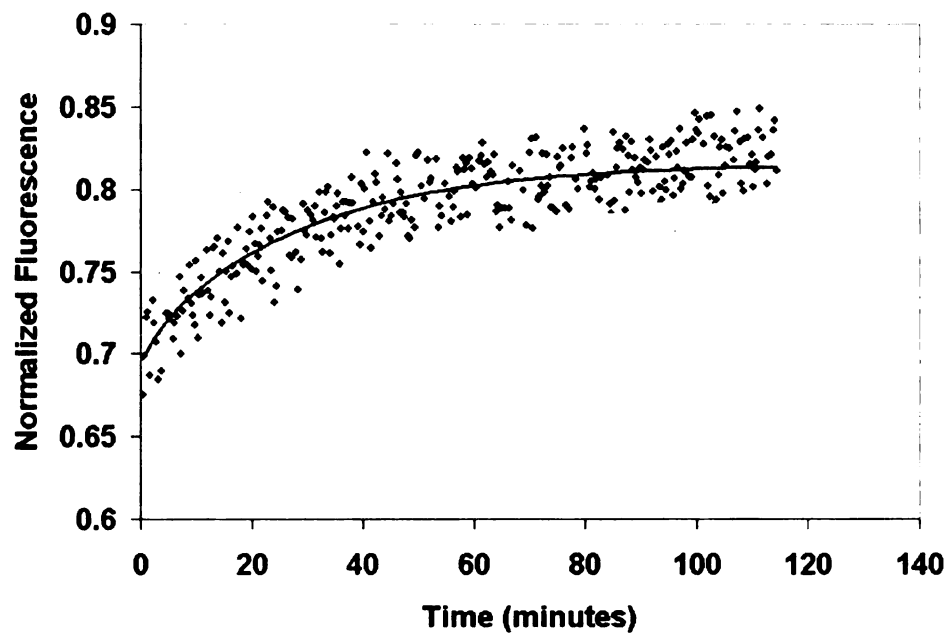


Figure 6.6: Fluorescence recovery after pattern photobleaching (FRAPP) profile of lipid bilayers on electrolessly deposited gold films. The dots represent post-bleach fluorescence intensity normalized against the corresponding pre-bleach fluorescence value. The solid line in the figure represents the fit of the recovery data.

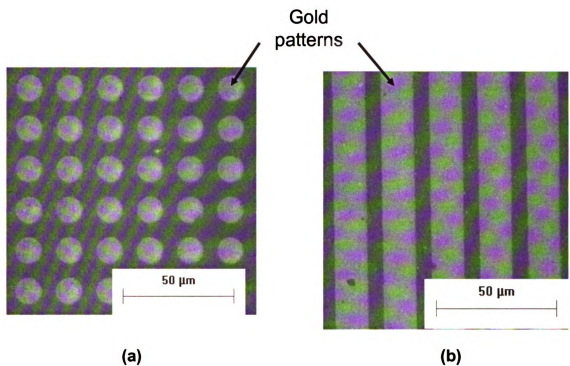


Figure 6.7: Optical microscopy images of gold: (a) circular patterns on a glass slide; (b) line patterns on a glass slide.

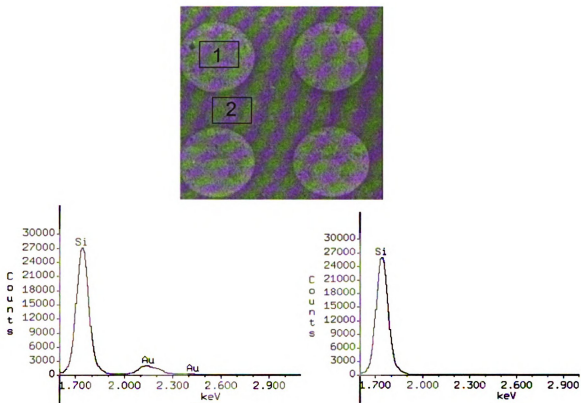


Figure 6.8: EDS image showing (a) X-rays collected from Region 1 of a SEM image; (b) X-rays collected from Region 2 of a SEM image. There is a peak corresponding to Au in X-rays collected from Region 1 but not in X-rays from Region 2, confirming the selective deposition of Au on the patterned surface.

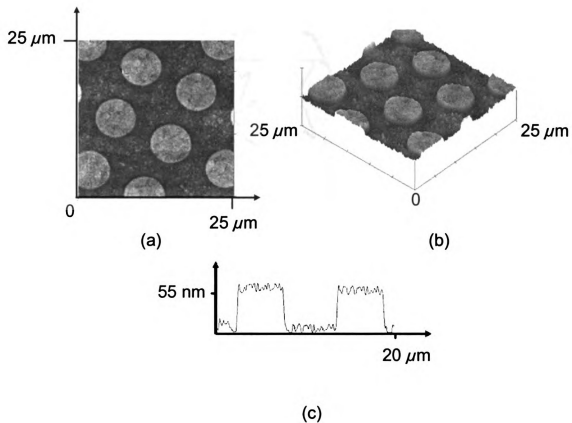


Figure 6.9: (a) Topographical AFM image of gold patterns; (b) 3-D image of the patterns; (c) pattern height on glass slide. All these images were obtained in air using tapping mode.

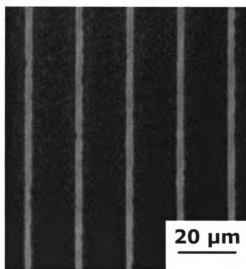


Figure 6.10: Fluorescence image showing line patterns of a lipid bilayer consisting of NBD-PE as the fluorophores. The image was obtained using a filter cube (Ex: 465-495/DM: 505/Em: 515-555).

7 INTACT TRANSFER OF LAYERED BIONANOCOMPOSITE ARRAYS

7.1 ABSTRACT

Microarrays containing multiple, nanostructured layers of biological materials would enable high-throughput screening of drug candidates, investigation of protein-mediated cell adhesion, and fabrication of novel biosensors. In this paper, we present an approach that allows high-quality microarrays of layered, bionanocomposite films to be deposited. The approach uses layer-by-layer self-assembly to preestablish a multilayered structure on an elastomeric stamp, and then uses microcontact printing to transfer the 3-D structure intact to the target surface. This approach extends the method previously used for intact transfer of polyelectrolyte multilayer patterns to include amphiphilic biomolecules, such as proteins and dendrimers. The approach overcomes a problem encountered when using microcontact printing to establish a pattern on the target surface and then building sequential layers on the pattern via layer-by-layer self-assembly. Amphiphilic molecules tend to adsorb both to the patterned features as well as the underlying substrate, resulting in low-quality patterns. By circumventing this problem, this research significantly extends the range of surfaces and layering constituents that can be used to fabricate 3D, patterned, bionanocomposite structures.

7.2 INTRODUCTION

Elastomeric patterning methods, such as microcontact printing (μ CP) (Kumar and Whitesides 1993), microcontact molding (μ CM) (Kim and Xia 1995), and microfluidics (Kim, Park et al. 2001), allow a two-dimensional pattern to be fabricated on a surface. In μ CP, an elastomeric stamp having the desired topographic pattern is coated

with a molecular ink and then brought into contact with the surface. Removal of the stamp leaves behind a thin layer of ink having the same pattern as the stamp. Based on the chemical contrast between the inked features and the ink-free background, additional layers can then be selectively deposited on either the features or background by directed self-assembly (Lee, Zheng et al. 2002; Kidambi, Chan et al. 2004).

Biological activity can be imparted to these structures by incorporating protein or other biomolecules during the LBL assembly process. Protein and DNA patternings using photolithography or electron beam lithography have been reported (Michel, Lussi et al. 2002; Zhang, Tanii et al. 2004). In these studies, patterned interfaces were created having discrete regions of reactive terminal groups, onto which proteins or DNA molecules were subsequently adsorbed.

The biological activity can further be augmented by co-immobilization of other macromolecules, like dendrimers or polyelectrolyte multilayers (PEMs) both of which allow the local environment of the protein to be customized. Dendrimers are radially symmetrical polymeric molecules that are grown by sequential addition of branched monomers to the outer shell. With each new addition (generation), the molecular weight of the dendrimer and the density of its terminal functional groups increases substantially (Tomalia, Naylor et al. 1990; Dvornic and Tomalia 1996; Tomalia and Dvornic 1996; Kohli, Dvornic et al. 2004). Dendrimers can have a highly functionalized outer surface, making them promising candidates for applications in drug delivery (Boas and Heegaard 2004), imaging (Balzani, Ceroni et al. 2003) and sensing (Ghosh and Banthia 2004). Dendrimers can also serve as functional frames to encapsulate small molecules needed by the proteins, including enzyme cofactors and electron mediators. PEMs can be used to

immobilize hydrophobic membrane proteins onto hydrophilic substrates, entrap ionic or polar small molecules needed by the proteins, and act as an ion-selective barrier to screen out interfering molecules (Lvov, Ariga et al. 1995).

In some cases, layer-by-layer assembly of 3-D structures onto patterns deposited by μ CP is hindered by the lack of sufficient chemical contrast between the features and background (i.e., the bare surface), making it difficult to deposit additional layers cleanly on only the feature or the background. This problem can be particularly challenging when a layer of amphiphilic molecules (e.g., proteins and dendrimers) is to be deposited, because amphiphilic molecules can adsorb both to hydrophilic and hydrophobic surfaces. Polyelectrolyte multilayers also present challenges, because the alternating anionic and cationic layers could adsorb to either positive or negative charges on the background surface.

In this chapter, we present an approach that overcomes the abovementioned difficulties in establishing well-defined, 3D bionanocomposite patterns (Kohli, Worden et al. 2005). The approach (intact transfer printing, ITP) entails combining spin self-assembly (Kohli, Dvornic et al. 2004) and layer-by-layer self-assembly (Lvov, Ariga et al. 1995; Kidambi, Chan et al. 2004) to pre-establish a multilayered structure on an elastomeric stamp, and then using μ CP to transfer the 3-D structure intact to the target surface. While μ CP was recently used to transfer preformed PEMs to a substrate (Park and Hammond 2004), this paper presents for the first time conclusive evidence of formation of bionanocomposite layered structures on a micropatterned stamp and subsequent transfer of the structures intact to a target substrate.

As examples, in this paper we present the fabrication and characterization of some 3-D nanostructured architectures (or structures) consisting of dehydrogenase enzymes, polyamidoamine (PAMAM) dendrimers and PEMs, possible using this approach. For the present study, generation four (G 4) PAMAM dendrimers and two different dehydrogenase enzymes were used: secondary alcohol dehydrogenase and sorbitol dehydrogenase (sDH).

This research is expected to significantly extend the range of surfaces and layering constituents that can be used to fabricate 3D, patterned bionanocomposite structures. Such structures have a broad range of potential applications, including fabricating protein-containing micro-arrays, studying mechanisms of protein-mediated cell adhesion (MacBeath and Schreiber 2000; Berg, Yang et al. 2004), diagnosing disease states (Fodor, Read et al. 1991), constructing biosensors, and investigating interactions between proteins and other molecules.

7.3 EXPERIMENTAL SECTION

7.3.1 Materials

G4 amine-terminated PAMAM dendrimer (10 wt % solution in methanol, M_w , 14,215) sulfonated poly(styrene) (SPS) (M_w ~70,000), sorbitol dehydrogenase (sDH), poly(diallyldimethyl ammonium chloride) (PDAC) (M_w ~100,000) were obtained from Sigma (St. Louis, MO). Fluorescein isothiocyanate (FITC) and Alexa fluor 568 were obtained from Invitrogen (Carlsbad, CA). Secondary alcohol dehydrogenase (sADH) was expressed and purified according to published procedures (Burdette and Zeikus 1994).

Sylgard 184 silicone elastomer kit (Dow Corning, Midland, MI) was used to prepare the poly(dimethylsiloxane) (PDMS) stamps for μ CP. Ultrapure water supplied by a Nanopure-UV four-stage purifier (Barnstead International, Dubuque, IA); the purifier was equipped with a UV source and a final 0.2 μ m filter.

7.3.2 Preparation of polyelectrolyte multilayers (PEMs)

A Carl Zeiss slide stainer equipped with a custom-designed ultrasonic bath was connected to a computer to perform LBL assembly (Lee, Zheng et al. 2002; Lee, Hammond et al. 2003; Kidambi, Chan et al. 2004). For PDAC/SPS multilayers, the concentration of SPS and PDAC was 0.01 M and 0.02 M, respectively, as based on the molecular repeat units. All polyelectrolyte solutions contained 0.1 M NaCl and were at a pH of 7.0. PEMs were deposited on the glass slide using the procedure described earlier.

7.3.3 Fluorescent labeling of PAMAM dendrimers, sADH and sDH

FITC was predissolved in acetone and added to an aqueous solution of PAMAM dendrimers. The resulting solution was allowed to stand overnight with occasional stirring. The total amount of dye was adjusted to label just one amino group per PAMAM molecule on average, assuming perfect reaction efficiency. The PAMAM solutions were then dialyzed against pure water (pH, 7.4) using membrane tubing (M_w cutoff 2000) to dialyze out unreacted FITC.

sADH was labeled using both FITC (green dye) and alexa fluor (red dye). A 5.5 mg sample of sADH, in 2 mL Tris buffer was dialyzed against a 0.1 M sodium bicarbonate solution, pH= 8.5, for 24 h. The bicarbonate solution was changed every 6 h during the dialysis process. FITC (or alexa fluor) was then added to the resulting protein

solution, in 1:1 mol ratio and continuously stirred for 10 h. The protein solution was then dialyzed against phosphate buffer (pH 7.4) for 24 h, changing the buffer every 6 h, to remove excess FITC (or alexa fluor).

Alexa fluor was added to the sDH protein solution (2 mg/ml), in 1:1 mol ratio and continuously stirred for 6 h. The protein solution was then dialyzed against phosphate buffer (pH 7.4) for 24 h, changing the buffer every 6 h, to remove excess alexa fluor.

7.3.4 Fabrication of 3-D structures or architectures

Figure 7.1 depicts the different 3-D architectures (or structures) that were fabricated and studied. In Case 1, a PDMS stamp was dipped in a solution of FITC labeled sADH (1 mg/ml) or alexa fluor labeled sDH solution (1 mg/mL) in 20 mM phosphate buffer (pH 7.4) for 2 h. The stamp was washed thoroughly with water and then either 20 or 40 PDAC/SPS multilayers were grown on it according to previously described procedure. The modified PDMS stamp was washed with water, dried under nitrogen and brought into contact with a glass slide coated with 10.5 PDAC/SPS bilayers. The stamp was removed after 20 min and the resulting patterned substrate was washed thoroughly with water to remove loosely bound molecules. In case 2, a PDMS stamp was dipped in a solution of sADH (1 mg/mL) (either FITC labeled or unlabeled) in 20 mM phosphate buffer (pH 7.4) for 2 h. The stamp was washed with water and dipped in 10 μ M aqueous solution of PAMAM dendrimers (pH 7.4) (FITC labeled or unlabeled) for 30 min. The stamp was rinsed with water and 30 PDAC/SPS multilayers were grown on to it. The modified PDMS stamp was washed with water, dried under nitrogen and brought into contact with a glass slide coated with 10.5 PDAC/SPS bilayers. The stamp was removed

after 20 min and the resulting patterned substrate was washed thoroughly with water. In case 3, a plasma cleaned PDMS stamp was dipped in FITC labeled sADH solution (1 mg/ml, pH 7.4 in phosphate buffer) for 2h. The stamp was rinsed with water and 1 PDAC/SPS bilayer was grown in it. The stamp was then washed with water and dipped in alexa fluor labeled sADH solution (1 mg/mL, pH 7.4 in phosphate buffer) for 2h. The modified PDMS stamp was then washed with water, dried under nitrogen and brought into contact with a glass slide coated with 10.5 PDAC/SPS bilayers. The stamp was removed after 20 min and the resulting patterned substrate was washed thoroughly with water.

7.3.5 Other measurements

All the fluorescence images were obtained with the Nikon Eclipse E 400 microscope (Nikon, Melville, NY) using two filter sets, one for FITC (Ex: 465-495/DM: 505/Em: 515-555), and the other one for alexa fluor (Ex: 510-560/DM: 565/Em: 590-690). AFM images were obtained with a Nanoscope IV multimode scope (Digital Instruments, Santa Barbara, CA). The microscope was equipped with tapping-mode etched silicon probes. The thickness analysis of the patterns was determined using cross-sectional analysis of the AFM images.

7.4 RESULTS AND DISCUSSIONS

Figure 7.1 depicts the procedure (ITP) used for fabricating different 3-D architectures or structures. Briefly, a multilayered film consisting of proteins, polyelectrolytes or dendrimers is assembled on top of an elastometric stamp using layer by layer assembly, and then transferred intact to a substrate which is oppositely charged from the multilayer

film's top surface. The choice of the base layer is a critical element in ITP process. The base layer should strongly and evenly adsorb on stamp; non uniform pattern transfer can occur without a smooth base layer. However, the attractive interactions between the base layer and stamp should be weak enough to allow easy detachment from the stamp during printing. To achieve this balance, we exploited hydrophobic interactions between the PDMS stamp and sADH (or sDH) base layer in the fabrication of all 3-D structures. The adsorption of this base layer using non-electrostatic interactions provides a charged surface for the assembly of other layers. The ITP process was not reproducible and non-uniform when other macromolecules such as PDAC or SPS were used as base layers.

Figure 7.2a and 7.2b show the two dimensional and cross-sectional AFM images, respectively, when a single layer of sADH was transferred. The light regions show the deposited sADH patterns, while the dark regions are the underlying substrate. The sADH patterns had an average height of 7 ± 2 nm. Figures 7.3a and 7.3b show the two-dimensional and cross-sectional images, respectively, when a multilayer film (see Figure 7.1, case 1) consisting of sADH base layer and 20 PDAC/SPS bilayers, $(\text{sADH})_1(\text{PDAC/SPS})_{20}$, was transferred on a PEM coated glass substrate. The average pattern height was approx. 67 ± 3 nm. On the other hand, the average pattern height (see Figures 7.3c and 7.3d) was approx. 127 ± 4 nm when a $(\text{sADH})_1(\text{PDAC/SPS})_{40}$ multilayer film was transferred. On taking into account the contribution from sADH layer (approx. 7 nm), the pattern height was found to linearly increase with the number of PDAC/SPS bilayers and determined to be approximately 60 ± 3 nm for 20 PDAC/SPS bilayers and 120 ± 4 nm for 40 PDAC/SPS bilayers. From these values, the average

height of a pair of PDAC/SPS was determined to be 3 ± 0.15 nm. This agrees well with literature values of 3.4 nm for similar deposition conditions (Kidambi, Chan et al. 2004).

Fluorescence microscopy was used to check the efficiency and feasibility of the multilayer film transfer. Figure 7.4a shows the fluorescence image of the circular patterns obtained on the transfer of a multilayer film consisting of a layer of fluorescently labeled sADH and 20 PDAC/SPS bilayers. As can be seen by the fluorescent features of the circular arrays and clean background regions, the multilayer film transfer occurred only in the patterned region and negligibly in the background (unpatterned) region. The fluorescence image of the stamp (Figure 7.4b) itself revealed little fluorescence in the circular region where the transferred film existed. On the other hand, the background region retained fluorescence. This suggests that the transferred film was complete, and the multilayer film remained completely intact during the transfer process. The ITP process was reproducible over an area of around 1 cm x 1 cm and is possibly reproducible over larger areas also.

The ability to make multilevel and multicomponent patterns consisting of amphiphilic molecules such as proteins and PEMs has potential applications in biocatalysis and also for the fabrication of practical devices. To demonstrate multilevel and multicomponent patterning, two different multilayer composite films were stamped on a surface (Figure 7.5). One multilayer film consisting of alexa fluor labeled sDH and 20 PDAC/SPS bilayers was stamped first on a PEM (10.5 PDAC/SPS bilayers) coated surface. This was followed by the stamping of a second multilayer film consisting of FITC labeled sADH and 20 PDAC/SPS bilayers at an angle perpendicular to the first printed lines. Figure 7.6a shows the red fluorescence from vertically printed

(sDH)₁(PDAC/SPS)₂₀ lines and Figure 7.6b shows green fluorescence from horizontally printed (sADH)₁(PDAC/SPS)₂₀ lines. Figure 7.6c shows a digitally combined image showing both the red and green fluorescence, suggesting the transfer of both multilayer systems. The pattern height in the crossed region and uncrossed region using the AFM cross-sectional analyses was found to be approximately 125-130 nm and 65-70 nm, respectively. As expected, these results suggest the combination of multilayer films at the crossover regions and intact transfer at the uncrossed regions.

The possibility of multicomponent multilayer film transfer was further demonstrated by transferring a multilayer film (see Figure 7.1, Case 2) consisting of sADH, G4 PAMAM dendrimers and PDAC/SPS bilayers, (sADH)₁(PAMAM)₁(PDAC/SPS)₃₀, intact to a surface. Fluorescence microscopy was used to establish the existence of alternating protein and dendrimer layers in the multilayered films after deposition. In one case (Figure 7.7a), only the protein was fluorescently labeled. In the other case (Figure 7.7b), only the dendrimer was labeled. Fluorescence observed in both Figures confirms the presence of both the protein and dendrimer layers. AFM was then used to confirm incorporation of PEM bilayers into the multilayered films. Figures 7.8a and 7.8b show the AFM images of a patterned film containing sequential layers of protein, dendrimers and PEMs (30 PDAC/SPS bilayers) on a PEM coated substrate. Figures 7.8c and 7.8d show the AFM images of a patterned film containing sequential layers of protein and dendrimers. The height of patterns was approximately 101 ± 4 nm with PEMs, and approximately 9 ± 2 nm without PEMs. Based on these data, the average height of each PDAC/SPS bilayer was estimated to be about 3.07 ± 0.14 nm, which is in agreement with published values.

Further proof of the potential advantages of ITP was demonstrated by stamping a multilayer film (Figure 7.1, Case 3) consisting of a PDAC/SPS bilayer sandwiched between two sADH layers. Fluorescence microscopy was again used to confirm the presence of different protein layers. The base sADH layer was fluorescently labeled with a green dye FITC, and the top sADH layer was labeled with a red dye alexa Fluor. The observance of both the green (Figure 7.9a) and red fluorescence (Figure 7.9b), confirms the presence of both sADH layers. AFM was then used to confirm the incorporation of PDAC/SPS bilayer in between these sADH layers. Figure 7.9c shows the cross-sectional topographical image of a patterned film containing sequential layers of sADH and 1 PDAC/SPS bilayer. The average height of pattern was 10 ± 1 nm. On taking into account the contribution from sADH layer (approximately 7 nm), the height corresponding to each PDAC/SPS bilayer can be estimated to be 3 ± 1 nm, which is consistent with our other results. Figure 7.9d shows the topographical image of a patterned film consisting of (sADH)₁(PDAC/SPS)₁(sADH)₁. The average height of the patterns was 17 ± 2 nm. Based on these data, the height of the topmost sADH layer was estimated to be approx. 7 ± 2 nm.

We believe electrostatic interactions between the enzymes, dendrimers and PEMs are responsible for stabilizing these different multilayered structures. Weak polyelectrolytes change their conformation or charge density with pH.(Yoo, Shiratori et al. 1998; Yang and Rubner 2002) Thus, the shape and stability of the resulting 3-D structures formed with weak polyelectrolytes often vary with pH. To avoid such effects, we used the strong polyelectrolytes SPS and PDAC, whose charge density is relatively unaffected by pH.

Our novel approach, in which bionanocomposite arrays are preestablished on a stamp and then transferred intact to the target substrate, is based on *topographical contrast* between the feature and background regions of the pattern, rather than *chemical contrast*. Thus, the new method offers significant advantages over the conventional, directed-self-assembly approach in cases when the chemical contrast is marginal or when amphiphilic or zwitterionic molecules (e.g., proteins) are involved. In such cases, adsorption is likely to occur on both the background and feature regions, leading to poor resolution. This effect is clearly illustrated by the much cleaner patterns seen in Figure 7.7a, where the SADH-containing pattern was transferred intact, than in Figure 7.10, where SADH was adsorbed from solution onto both the dendrimer features and the SPS background.

This research significantly extends the range of surfaces and layering constituents that can be used to fabricate 3D, patterned, bionanocomposite structures. Such structures have a broad range of potential applications, including fabricating protein-containing microarrays for screening drug candidates, studying mechanisms of protein-mediated cell adhesion (Mac Beath and Schreiber 2000; Berg, Yang et al. 2004) diagnosing disease states (Fodor, Read et al. 1991) constructing biosensors, and investigating interactions between proteins and other molecules

7.5 CONCLUSIONS

In this paper, different 3-D architectures have been fabricated and characterized using a unique multilayer approach. This multilayer approach, in which bionanocomposite arrays are preestablished on a stamp and then transferred intact to the target substrate, is based on the topographical contrast, rather than chemical contrast.

Thus this method offers several advantages over conventional, directed self assembly approach in cases when the chemical contrast is marginal or when amphiphilic or zwitterionic (e.g., proteins). In such cases, adsorption is likely to occur on both the background and feature regions, leading to poor resolution. This research, thus, significantly extends the range of interfaces and layering constituents that can be used to fabricate 3-D bionanocomposite arrays.

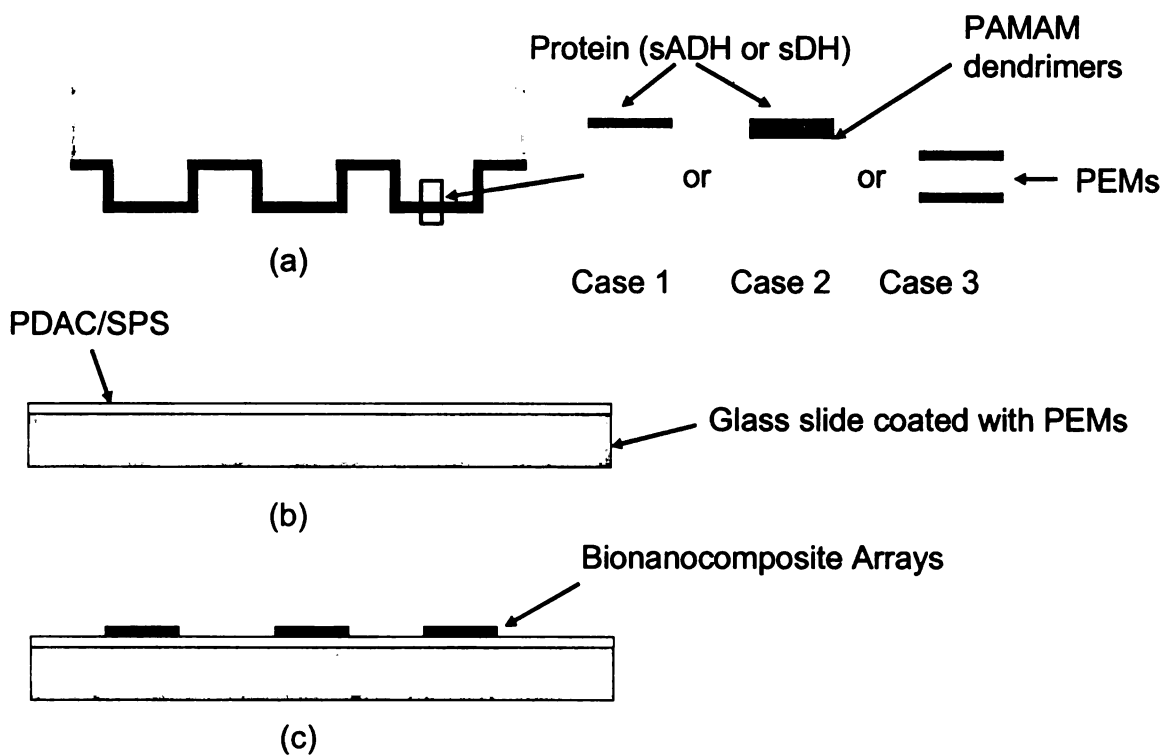


Figure 7.1: Schematic representation of the procedure used for printing: (a) stamp coated with sequential layers of proteins (sADH or sDH) and PEMs (PDAC/SPS bilayers) (Case 1); alternating layers of sADH and G4 PAMAM dendrimers on PEMs (case 2); and PDAC/SPS bilayer sandwiched between sADH layers (case 3). (b) Glass slide coated with PEMs (10.5 bilayers). (c) Patterned substrate

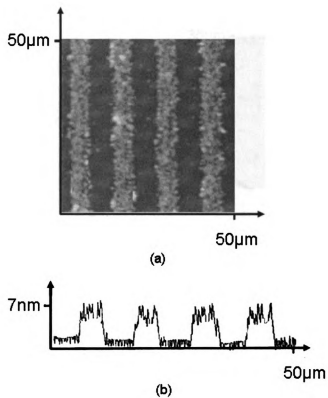


Figure 7.2: (a) Two-dimensional AFM image of sADH patterns, on a PEM (10.5 PDAC/SPS bilayers) coated glass substrate. (b) Cross-sectional AFM image of sADH patterns, on a PEM (10.5 PDAC/SPS bilayers) coated glass substrate.

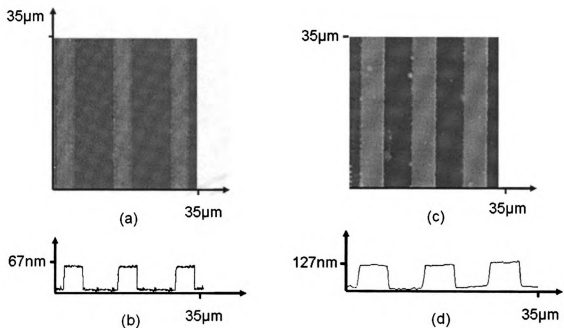


Figure 7.3: Two-dimensional and cross-sectional AFM images: (a-b) when a $(sADH)_1(PDAC/SPS)_{20}$ multilayer film was transferred to a PEM (10.5 PDAC/SPS bilayers) coated glass substrate; (c-d) when a $(sADH)_1(PDAC/SPS)_{40}$ multilayer film was transferred to a PEM (10.5 PDAC/SPS bilayer) coated glass substrate.

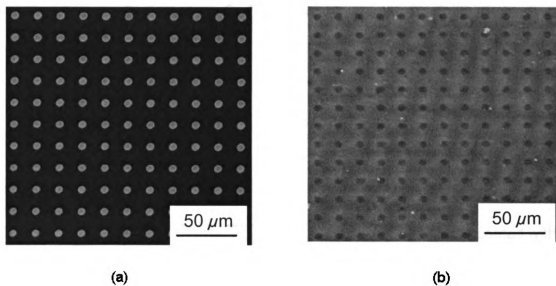


Figure 7.4: Fluorescence images of: (a) the circular patterns obtained on the transfer of a multilayer film consisting of a layer of fluorescently labeled sADH and 20 PDAC/SPS bilayers, on a PEM (10.5 PDAC/SPS bilayers) coated glass substrate; (b) the PDMS stamp surface after printing.

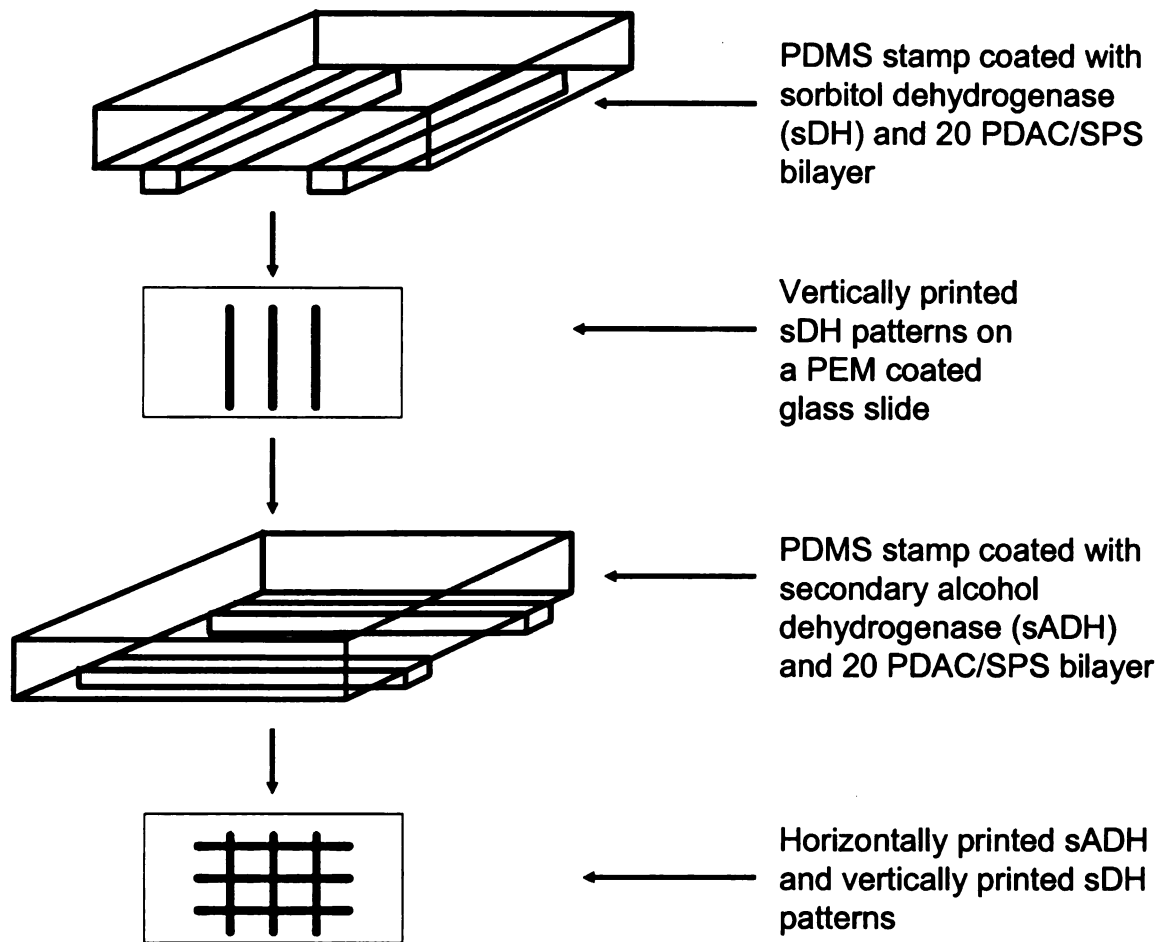


Figure 7.5: Schematic representation of the process used for multilevel and multicomponent stamping

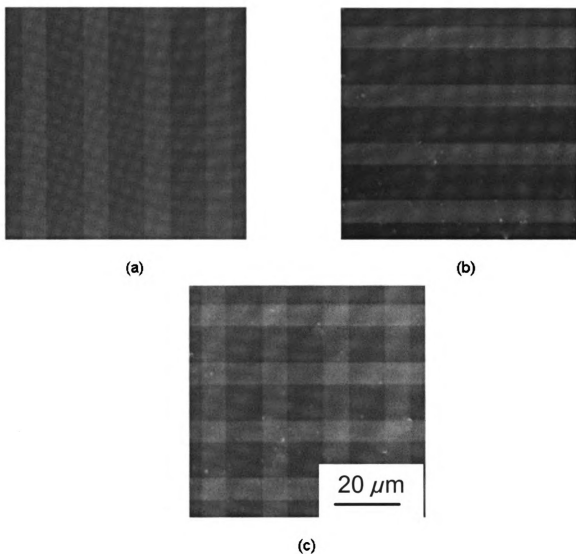


Figure 7.6: (a) Red fluorescence from vertically printed (Alexa fluor labeled-sDH)₁(PDAC/SPS)₂₀ lines on a PEM (10.5 PDAC/SPS bilayers) coated glass substrate; (b) Green fluorescence from horizontally printed (FITC labeled-sADH)₁(PDAC/SPS)₂₀ lines, on a PEM (10.5 PDAC/SPS bilayers) coated glass substrate;(c) Digitally combined fluorescence image showing both red and green fluorescence

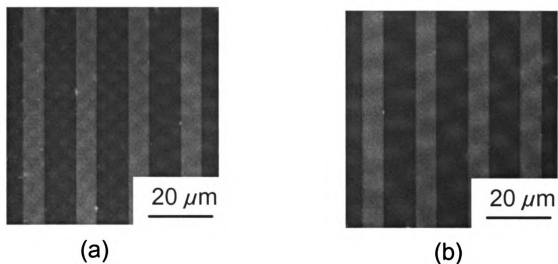


Figure 7.7: (a) Fluorescence image of the patterned films of sADH, G4 PAMAM dendrimers and PEMs (30 PDAC/SPS bilayers) with fluorescently labeled sADH as the topmost layer, on a PEM (10.5 PDAC/SPS bilayers) coated glass substrate. (b) Fluorescence image of the line patterns of fluorescently labeled dendrimers sandwiched between patterned sADH layer and PEMs (30 PDAC/SPS), on a PEM (10.5 PDAC/SPS bilayers) coated glass substrate.

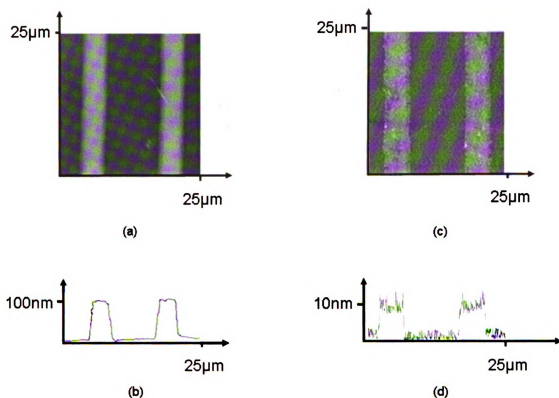


Figure 7.8: (a-b) Two-dimensional and cross-sectional AFM images of a patterned film containing sequential layers of sADH, PAMAM dendrimers and PEMs (30 PDAC/SPS bilayers), with sADH as the topmost layer, on a PEM (10.5 PDAC/SPS bilayers) coated glass substrate. (c-d) Two-dimensional and cross-sectional AFM images of a patterned film containing sequential layers of sADH and PAMAM dendrimers with sADH as the topmost layer, on a PEM (10.5 PDAC/SPS bilayers) coated glass substrate.

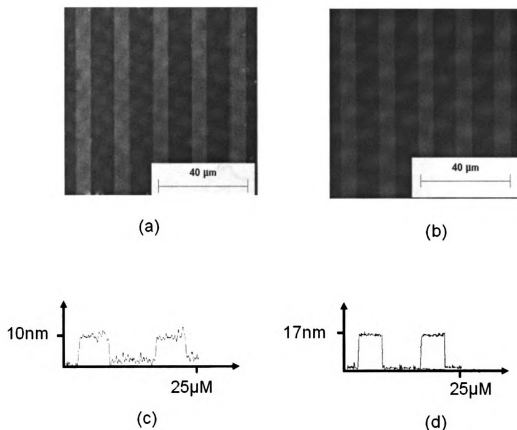


Figure 7.9: (a-b) Fluorescence images of the patterned films of a PDAC/SPS bilayer sandwiched between FITC labeled sADH base layer and Alexa fluor labeled sADH topmost layer, on a PEM (10.5 PDAC/SPS bilayers) coated glass substrate, (a) Green fluorescence emanating from FITC labeled sADH base layer, obtained using the following filter set, Ex: 465-495/DM: 505/Em: 515-555; (b) Red fluorescence emanating from Alexa fluor labeled sADH topmost layer, obtained using the following filter set, Ex: 510-560/DM: 565/Em: 590-690. (c) Cross-sectional topographical image of a patterned film containing sequential layers of sADH and 1 PDAC/SPS bilayer, on a PEM (10.5 PDAC/SPS bilayers) coated glass substrate. (d) Topographical AFM image of a patterned film consisting of a PDAC/SPS bilayer sandwiched between two sADH layers, on a PEM (10.5 PDAC/SPS bilayers) coated glass substrate.

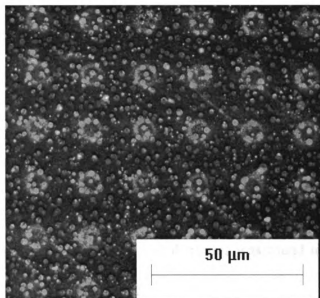


Figure 7.10: Arrays of amphiphilic proteins obtained on patterned substrate using directed self-assembly

8 NANOSTRUCTURED CROSS-LINKABLE MICROPATTERNS VIA AMPHIPHILIC DENDRIMER STAMPING

8.1 ABSTRACT

Microcontact printing was used to deposit stable, nanostructured, amphiphilic and cross-linkable patterns of PAMAMOS-DMOMS dendrimer multilayers onto silicon wafers, glass, and polyelectrolyte multilayers. The effects of dendrimer ink concentration, contact time, and inking method, on the thickness, uniformity and stability of the resulting patterns were studied using optical microscopy, fluorescence microscopy, AFM, and contact-angle analysis. Dendrimer film thickness was found to be controllable via conditions used during spin-self assembly.

8.2 INTRODUCTION

Functional, 3-D nanostructures and microstructures on surfaces can serve as excellent molecular templates for applications in optoelectronics and biotechnology (Rudolph 1994; Blawas and Reichert 1998; Kidambi, Chan et al. 2004). Coupling stable, amphiphilic films with hydrophobic biological molecules can yield biomimetic interfaces able to reproduce biological functions *in vitro* (Trojanowicz 2001). Recently, thin films of amphiphilic molecules have been used to couple proteins to carbon nanotubes (Berzina, Troitsky et al. 1996; Feng, Li et al. 2003). 3-D patterns of amphiphilic molecules can also be used in photon harvesting, organic and polymeric electroluminescent devices (e.g., light-emitting diodes), organic solid-state lasers, and photonic band gap materials (Arias-Marin, Arnault et al. 2000; Fluerau, Schrader et al. 2000; Schulz, Dietzel et al. 2001; Krebs, Spanggaard et al. 2003). Micro- and nanoscale partitioning of regions with different chemical composition, charge, or environmental conditions is a widely used biological motif, as evidenced by the many membrane-separated organelles and membrane-mediated signaling mechanisms found in cells (Tien and Ottova 2000; Tavares, Fletcher et al. 2001).

Dendrimers make up a unique, highly diverse class of polymers that have well-defined macromolecular architectures and are almost perfectly monodisperse. Radially layered poly-(amidoamine-organosilicon) (PAMAMOS) dendrimers are especially versatile, amphiphilic and cross-linkable globular-shaped macromolecules (Dvornic, de Leuze-Jallouli et al. 2000). PAMAMOS dendrimers having dimethoxymethylsilyl (DMOMS) end-groups can be denoted as PAMAMOS-DMOMS (p, q), where p and q are integers that define the generation of the polyamidoamine (PAMAM) interior and the

number of exterior layers of organosilicon (OS) branch cells, respectively (see Figure 8.1). PAMAMOS are generally prepared from commercially available PAMAMs with different relative degrees of amino end-group conversion (i.e., OS substitution). In this study, PAMAMOS-DMOMS (2,1) dendrimers were used (see Experimental section).

Microcontact printing (μ CP) is a soft lithographic technique used in physics, chemistry, materials science and biology to transfer patterned thin organic films to surfaces with sub-micron resolution (Kumar, Biebuyck et al. 1994; Wilbur, Kumar et al. 1996). Unlike other fabrication methods that merely provide topographic contrast between the feature and the background, μ CP also allows chemical contrast to be achieved via selection of an appropriate ink. μ CP offers advantages over conventional photolithographic techniques because it is simple to perform and is not diffraction limited. These techniques have been used to make patterns of various small and large molecules on metals and silicon substrates (St. John and Craighead 1996; Xia, Kim et al. 1996; Yang, Tryk et al. 1996) as well as to deposit proteins, biological cells (Yang, Mendelsohn et al. 2003; Berg, Yang et al. 2004; Kim, Doh et al. 2004), polymer thin films (POPS) (Jiang, Zheng et al. 2002), controlled particle cluster arrays (Lee, Zheng et al. 2002) and their selective metal plating (Lee, Hammond et al. 2003), and polyelectrolyte aggregates (Lee, Ahn et al. 2004). μ CP of PAMAM dendrimers has recently been reported (Ghosh, Lackowski et al. 2001; Arrington, Curry et al. 2002; Bittner, Wu et al. 2002; Li, Kang et al. 2002; Wu, Bittner et al. 2002; Li, Muir et al. 2003). In these studies the effect of dendrimer concentration on the pattern thickness was evaluated, and new approaches for electroless metallization of these patterns were

suggested. However, no attempt was made to study the effect of other process parameters controlling the patterns.

In this paper we report the first application of microcontact printing of the amphiphilic and cross-linkable PAMAMOS-DMOMS dendrimers on glass slides, silicon wafers and polyelectrolyte multilayers (PEMs) in which the pattern average thickness was controlled by spin-self assembly (i.e., spin-inking). The resulting 3-D micro-patterned amphiphilic networks were characterized by optical microscopy and atomic force microscopy (AFM). Also, the effects of dendrimer ink concentration, inking method and contact time on the thickness, uniformity and stability of the deposited patterns are presented. The results provide a framework for controlling the geometry of the deposited patterns. The lateral footprint of the pattern can be controlled by the shape of the elastomeric stamp, and the thickness of the patterns can be controlled by adjusting the spin coating method, the surface properties of the stamp, and the substrate used. The results also confirmed the well-known influences of spin speed, concentration, and solvent on the thickness of spin coated films (Pethrick and Rankin 1999; Cho, Char et al. 2001).

8.3 EXPERIMENTAL SECTION

Glass slides (Corning Glass Works, Corning, N.Y.) were cleaned with Alconox precision cleaner (Alconox Inc., New York, NY) in a Branson ultrasonic cleaner (Branson Ultrasonics Corporation, Danbury, CT) followed by sonication in pure water. They were then dried under nitrogen flow and subjected to oxygen plasma treatment in Harrick plasma cleaner (Harrick Scientific Corporation, Broadway Ossining, NY) for 5 min at 20 Pa vacuum. Polyelectrolyte multilayers (10 bilayers) were deposited on the glass slides using a standard procedure described elsewhere (Lee, Zheng et al. 2002; Zheng, Lee et al. 2002) with sulfonated poly(styrene) (SPS) as the polyanion and poly(dimethyldiallylammonium chloride) (PDAC) as the polycation.

Si (100) wafers (Silicon Sense Inc., Nashua, NH) were cleaned by immersion in Piranha solution (70% sulfuric acid and 30% hydrogen peroxide) at room temperature for 30 min, then rinsed with DI water and dried under nitrogen.

Patterned polydimethylsiloxane (PDMS) stamps were fabricated by pouring a 10:1 mixture of Sylgard 184 elastomer/curing agent (Dow Corning, Midland, MI) over a patterned silicon master. The mixture was cured for approximately 24 h at 60°C and then carefully peeled off the master.

Second generation (G2) PAMAMOS-DMOMS (2, 1) dendrimers were obtained as a 20% w/w methanolic solution from Dendritech, Inc. (Midland, MI). This solution was further diluted to the desired concentrations (from 0.01% to 1 wt.-%) with methanol.

Two different methods were utilized to apply ink: spin inking and dip inking. For spin inking, the stamps were cleaned and treated in the plasma cleaner for 30 s to make their surfaces hydrophilic. They were then coated with ink using a pipette and subsequently spun at 3000 rpm for 20 s. Monolayer coating of polymers by this spin self-assembly has been reported previously (Jang, Kim et al. 2003; Liu, Wang et al. 2003) . In the dipping method, the stamps were immersed in ink for several minutes and then dried under nitrogen flow. The ink was then transferred to the silicon substrate by bringing the stamp into conformal contact with the substrate.

PAMAMOS dendrimers were labeled with fluorescein isothiocyanate (FITC) using the standard procedure (Yu and Russo 1996). FITC was predissolved in acetone and added to methanol solutions of PAMAMOS. The resulting solutions were then allowed to stand overnight with occasional stirring. The total amount of dye was adjusted to label just one amino group per PAMAMOS molecule on average, assuming perfect reaction efficiency. The PAMAMOS solutions were then dialyzed against pure water using sterilized and rinsed membrane tubing. Water for rinsing and dilution was supplied by a Barnstead Nanopure Diamond-UV purification unit (Barnstead International, Dubuque, Iowa) equipped with a UV source and final 0.2 μm filter.

Optical-microscope images were obtained using a Nikon Eclipse ME 600 microscope, and fluorescence images were obtained using the Nikon Eclipse E 400 microscope (Nikon, Melville, NY). Advancing contact angle measurements were performed with a SEO Contact Angle Analyzer (Phoenix 450, Surface Electro Optics Corporation Ltd., Korea). AFM images were obtained with a Nanoscope IV multimode scope (Digital Instruments, Santa Barbara, CA). The microscope was equipped with

tapping-mode etched silicon probes. The thickness analysis of the micropatterned films was determined using cross-sectional analysis of the AFM images.

8.4 RESULTS AND DISCUSSIONS

The thickness of nanostructured micropatterns was found to be controllable, and the optimum stamping conditions for the uniform nanostructured micropatterned amphiphilic films with high lateral resolution were determined (see Figs. 8.2, 8.3). For all substrates tested, the pattern average thickness increased with dendrimer concentration over the concentration range from 0.1% to 1wt.-% when the stamp was spin-coated at 3000 rpm for 20 s. In this way, the transferred pattern average thickness can be controlled in the range of 100 to 550 nm by controlling the spin-coating conditions. Thin and unstable patterns (e.g., see Fig. 8.2a) were formed at concentrations less than 0.5 wt %, while higher concentrations (>0.5 wt %) resulted in thicker and stable patterns (e.g., see Figs. 8.2 (b-d) and 3). These results confirm the suitability of the spin-inking method as an alternative to the dip-inking (Wilbur, Kumar et al. 1996) to control the height and uniformity of the nanostructured and micropatterned films and is consistent with the previously reported dependence of spin coated film thickness on concentration, spin speed, and solvent (Pethrick and Rankin 1999; Cho, Char et al. 2001; Chiarelli, Johal et al. 2002).

Several parameters were systematically varied to obtain high-quality patterns having smooth, intact regions of deposited ink, whose shape faithfully reproduced the topography of the stamp. Under non-optimal conditions, undesirable pattern features were observed, including ink diffusion at the boundaries, which resulted in ragged edges,

and dendrimer aggregation within inked regions, which resulted in irregularly shaped ink microdomains separated by fissures in case of line patterns and doughnut shaped structures in case of circular patterns (e.g., Fig. 8.2a). The effects of dendrimer concentration and contact time on pattern characteristics are presented qualitatively in Table 8.1 for glass slides, silicon wafers, and polyelectrolyte multilayer-coated substrates having SPS as the surface layer. As can be seen in Table 8.1, silicon wafers and polyelectrolyte coated glass slides with sulfonated polystyrene (SPS) as the top-most layer required longer contact times for pattern transfer than bare glass surfaces. For a glass substrate, a 1 wt.-% solution of PAMAMOS spin-coated at 3000 rpm for 20 s and a contact time of 5 min resulted in the formation of uniform, stable patterns. For silicon wafers, a 1 wt.-% solution of PAMAMOS dendrimers spin-coated twice at 3000 rpm for 20 s and a contact time of 30 min resulted in uniform, stable patterns. For an SPS surface a 1 wt.-% solution dip-coated for 30 min and a contact time of 1 h resulted in the best patterns. At lower concentrations and contact times, thinner and unstable patterns were formed that showed ink aggregation. The reasons for dendrimer aggregation under these conditions are not clear from these data alone. However, mechanisms involved in polyelectrolyte aggregation under similar conditions have been explained elsewhere (Lee, Ahn et al. 2004). While aggregation could be eliminated by increasing the dendrimer concentration and contact time, at very high concentrations and contact times, diffusion also became a problem.

The optical microscopy image presented in Figure 8.2b shows excellent contrast between the PAMAMOS pattern produced and the substrate, indicating successful multilayered deposition of PAMAMOS. Fluorescent labeling of PAMAMOS-DMOMS

was necessary for lower concentrations of dendrimer inks, because printed features were difficult to visualize by optical microscopy alone. Previous developmental work on PAMAMOS-DMOMS has shown that up to 80 or 90% of the amino end-groups of PAMAM starting material typically reacts with (3-acryloxypropyl) dimethoxymethylsilane, leaving approximately 10-20% of the end-groups as primary or secondary amines that are available for reaction with suitable electrophiles (Dvornic, de Leuze-Jallouli et al. 2000). Hence, the dendrimers could be covalently bound to fluorescein isothiocyanate. Figures 8.2c, 8.2d show fluorescence images of circular patterns on a glass substrate and the line patterns on a polyelectrolyte coated glass slides with SPS as the top surface.

Figure 8.3a shows an AFM image of a patterned glass substrate stamped with a 1wt.-% dendrimer solution, for a contact time of 5 min, and Figure 8.3b shows an AFM image of patterned silicon wafer stamped with the same dendrimer solution for a contact time of 30 min. The light areas are deposited dendrimers, while the dark areas are the underlying substrate. The structure heights for these patterns are depicted in Figures 8.3c and 8.3d, respectively. The results indicate consistent coverage where the stamp met the substrate and uniform average thickness across the pattern. The pattern shape, as seen in the cross-sectional views (Figure 8.3c and 8.3d), was found to be round for most of the patterns transferred. This surface curvature, we believe, arises from a complex interplay of forces that occur during deposition and drying of the dendrimer ink, as well as unavoidable edge effects due to the size and shape of the AFM tip. The 3-D images shown in Figures 8.3e and Figure 8.3f indicate that the upper edges of the line patterns exhibited a slight height variance, which tended to decrease with the thickness of the

patterns for all substrates examined. Although rinsing with water after deposition smeared the patterns, very stable patterns could be obtained if the substrates were air-dried for an hour or cured in an oven at 120°C for an hour. This high stability is attributed to the crosslinking reaction depicted in Figures 8.4 and 8.5. The reaction is reported (Dvornic, de leuze Jallouli et al. 1999; Dvornic, Li et al. 2002) to proceed through two steps: (i) water hydrolysis of methoxysilyl (Si-OCH₃) end-groups to yield the corresponding silanols, Si-OH, and (ii) subsequent condensation of these silanols to form siloxane (Si-O-Si) interdendrimer bridges. The second reaction is self catalyzed by the basic PAMAM interiors and is easily accomplished either by direct exposure of methoxysilyl-functionalized PAMAMOS-DMOMS dendrimer precursors to atmospheric moisture, or by controlled addition of water either in the form of vapor (e.g., in a humidity chamber), or blended as liquid into a dendrimer solution. Since the process is a chain reaction in which the water consumed in the hydrolysis step is regenerated in the condensation step, less than the stoichiometric amount of water is needed.

Dip-inking produced thinner and relatively non-uniform (i.e., poorly covered and aggregated) features, while spin-inking produced thicker and more uniform features. This effect is attributed to spin coating giving a thicker layer of dendrimer ink than dip coating. An untreated stamp had a water advancing contact angle of 102° before plasma treatment and 6° after plasma treatment, indicating that the plasma treatment rendered the stamp surface hydrophilic. Coating the plasma-treated stamps with hydrophobic PAMAMOS dendrimer ink increased the surface hydrophobicity, and hence the contact angle. Spin-coated stamps had a higher contact angle (60°) than those dip-coated (around 45°), suggesting that the roughness, thickness and morphology of the thin films formed in

both cases are different. Because the thickness of the dendrimer ink layer can be controlled by adjusting the spin rate, spin coating should allow the properties of the patterned surface to be more finely controlled than dip coating.

Due to the very regular size and globular shape of the dendrimers and their controlled amphiphilicity and cross-linkable nature, the micropatterned arrays of PAMAMOS films offer advantages over other macromolecular materials in the fabrication of the 3-D bioconjugate surfaces and biomimetic interfaces for applications including producing biochips for proteomics, pharmaceutical screening processes, and addressing fundamental questions in cell adhesion (Blawas and Reichert 1998; Kane 1999; Mac Beath and Schreiber 2000; Yang, Mendelsohn et al. 2003; Berg, Yang et al. 2004; Kim, Doh et al. 2004). The cage-like structure and controllable porosity of dendrimers, coupled with the unique ability of PAMAMOS dendrimers to form highly cross-linked structures, makes the structures developed in this paper well suited to encapsulate molecular mediators and cofactors for redox enzymes used in bioelectronic applications (Willner and Katz 2000). Moreover, these versatile dendrimer arrays could serve as templates for nanoparticles growth or electroless metallization in development of nano metal reactors on micropatterned films (Balough, de leuze Jallouli et al. 1999; Dvornic and Owen 2002). Further characterization of patterned surfaces and in situ chemical reactions of these films is currently underway for electronic devices and sensor applications.

8.5 CONCLUSIONS

This paper reports the first micropatterned deposition of stable, nanostructured, amphiphilic and cross-linkable PAMAMOS-DMOMS dendrimer multilayers onto silicon wafers, glass surfaces, and polyelectrolyte multilayers. Using optical microscopy, fluorescence microscopy, AFM, and contact-angle analysis, the effects of dendrimer ink concentration, contact time, and inking method, on the thickness, uniformity and stability of the resulting patterns were studied. In the spin-self-assembly process, pattern average thickness increased with increasing dendrimer ink concentration at constant spin speed. Interdendrimer crosslinking via siloxane condensation allowed the 3-D amphiphilic and multilayered structures to remain stable for several days, even after washing if they were kept in air for an hour or heat treated at 120 °C in an oven. The resulting highly cross-linked networks have the ability to encapsulate nanoparticles and to serve as molecular templates for chemical and physical modifications in opto-electronic and biomimetic interface applications.

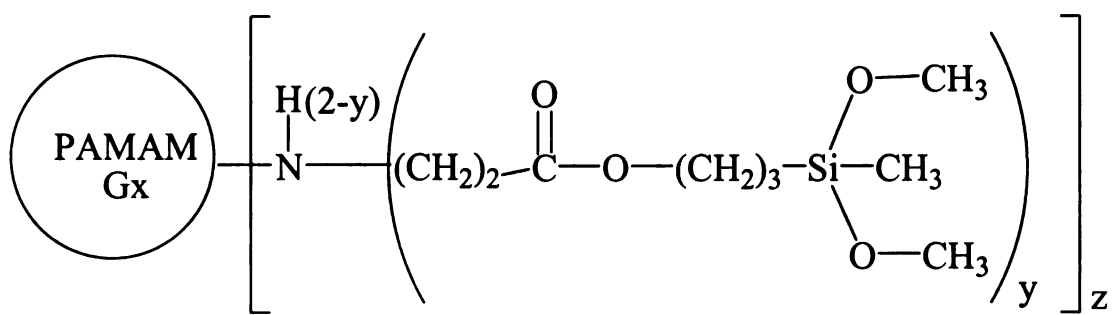


Figure 8.1: Schematic representation of PAMAMOS-DMOMS dendrimer.

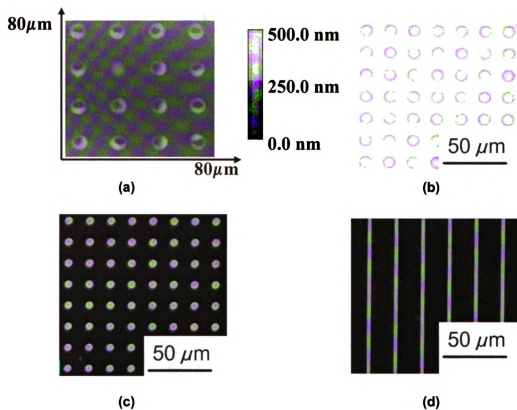


Figure 8.2: (a) An example of an AFM image showing unstable circular patterns on a glass slide obtained from a 0.5% PAMAMOS dendrimer solution. (b-d) Visualization of PAMAMOS dendrimer patterns on various substrates. (b) Optical micrograph of the circular patterns on a glass substrate (c) Fluorescence image of the circular pattern on a glass substrate; (d) Fluorescence image of the line pattern on a SPS surface.

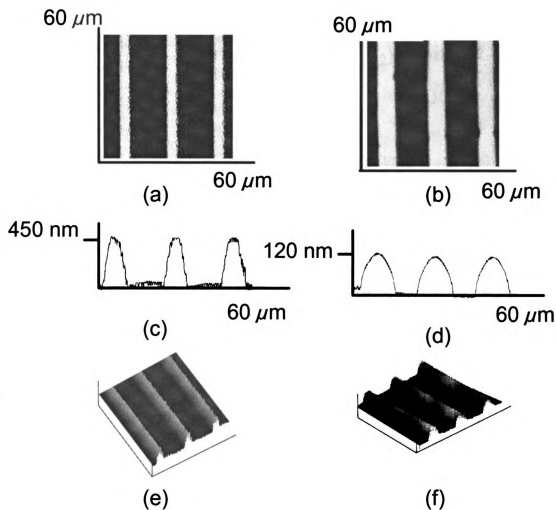


Figure 8.3: AFM images of cross-linked PAMAMOS dendrimer patterns. (a) Patterned glass substrate stamped by 1wt.-% dendrimer solution in methanol for a contact time of 5 min; (b) Patterned silicon wafer stamped by a 1wt.-% dendrimer solution in methanol for a contact time of 25 min; (c) Pattern height on glass substrate; (d) Pattern height on silicon wafer; (e) 3-D image of the patterned glass substrate; (f) 3-D image of the patterned silicon wafer.

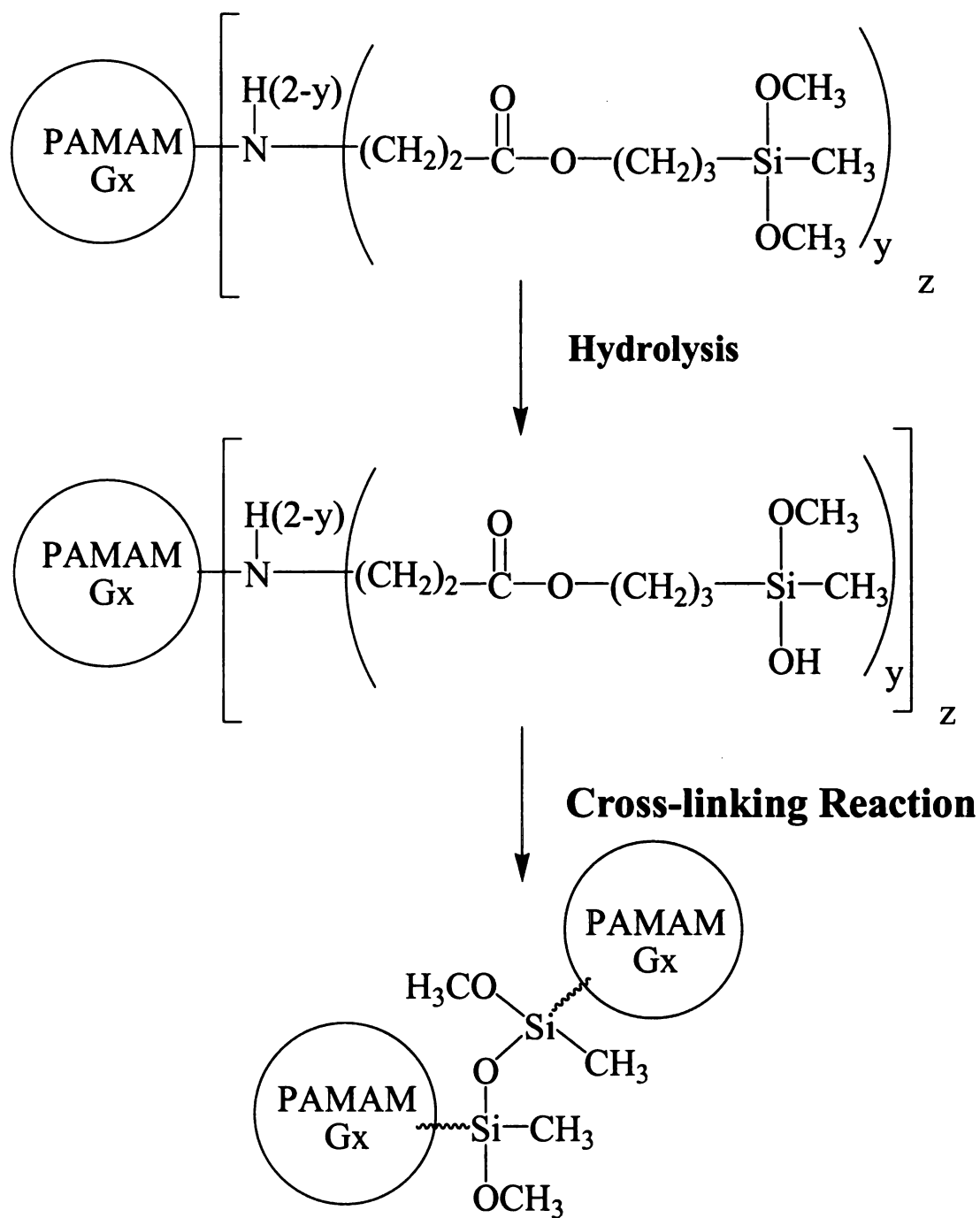


Figure 8.4: Crosslinking of PAMAMOS-DMOMS dendrimers into a covalently bonded network structure.

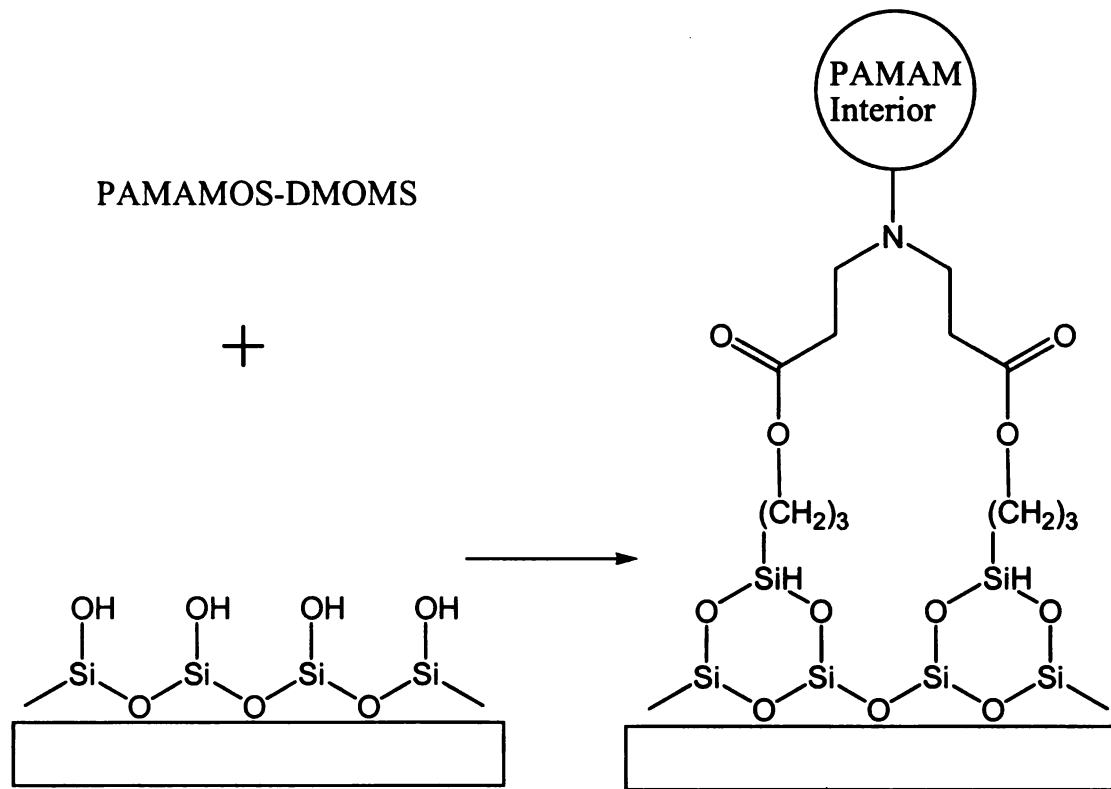


Figure 8.5: Covalent bonding of PAMAMOS-DMOMS dendrimers to glass surfaces having silanol surface groups.

Table 8-1: Effects of concentration and contact time on the stability and uniformity of patterns on different substrates

Glass Slides					Silicon Wafers	SPS Surface
Dendrimer Solution Concentration* (wt %)	Contact Time (min)					
	1	3	5	10	30	60
0.1 %	Poor coverage with aggregation	Fair coverage with some aggregation	Good coverage with some aggregation	Good coverage with diffusion and aggregation	Fair coverage with some aggregation	Fair coverage with some aggregation
0.5	Fair coverage with some aggregation	Fair coverage with very little aggregation	Good coverage	Good coverage with diffusion	Good coverage	Good coverage
1.0	Fair coverage with very little aggregation	Good coverage	Good coverage	Good coverage with diffusion	Good coverage	Good coverage

* Concentration less than 0.1 wt % resulted in negligible and unstable pattern transfers

9 REFERENCES

- Abel, A. P., M. G. Weller, et al. (1996). "Fiber-optic evanescent wave biosensor for the detection of oligonucleotides." Analytical Chemistry **68**(17): 2905-2912.
- Ahn, Y. B., L. A. Beaudette, et al. (2001). "Survival of a GFP-labeled polychlorinated biphenyl degrading psychrotolerant *Pseudomonas* spp. in 4 and 22 degrees C soil microcosms." Microbial Ecology **42**(4): 614-623.
- Albrecht, O., D. S. Johnston, et al. (1982). "Stable Biomembrane Surfaces Formed by Phospholipid Polymers." Biochimica Et Biophysica Acta **687**(2): 165-169.
- Allen, T. G. J. (1997). "The 'sniffer-patch' technique for detection of neurotransmitter release." Trends in Neurosciences **20**(5): 192-197.
- Alzagat, A. A. and I. Alli (2002). "Protein-lipid interactions in food systems: a review." International Journal of Food Sciences and Nutrition **53**(3): 249-260.
- Ariga, K. and Y. Okahata (1989). "Polymerized monolayers of single-chain , double-chain, and triple chain silane amphiphiles and permeation control through the monolayer-immobilized porous glass plate in an aqueous-solution." Journal of the American Chemical Society **111**: 5618-5622.
- Asaka, K., A. Ottova, et al. (1999). "Mediated electron transfer across supported bilayer lipid membrane (s-BLM)." Thin Solid Films **354**(1-2): 201-207.
- Atkins, J. and P. Glynn (2000). "Membrane Association of and Critical Residues in the Catalytic Domain of Human Neuropathy Target Esterase." The Journal of Biological Chemistry **275**(32): 24477-24483.
- Balachandra, A. M., J. H. Dai, et al. (2002). "Enhancing the anion-transport selectivity of multilayer polyelectrolyte membranes by templating with Cu^{2+} ." Macromolecules **35**(8): 3171-3178.
- Balzani, V., P. Ceroni, et al. (2003). Luminescent dendrimers. Recent advances. Dendrimers V: Functional and Hyperbranched Building Blocks, Photophysical Properties, Applications in Materials and Life Sciences. **228**: 159-191.

- Barak, L. S., S. S. G. Ferguson, et al. (1997). "A beta-arrestin green fluorescent protein biosensor for detecting G protein-coupled receptor activation." Journal of Biological Chemistry **272**(44): 27497-27500.
- Bartlett, P. N. and R. G. Whitaker (1987). "Electrochemical Immobilization of enzymes. 1. Theory." Journal of Electroanalytical Chemistry **224**: 27-35.
- Baselt, D. R., G. U. Lee, et al. (1998). "A biosensor based on magnetoresistance technology." Biosensors & Bioelectronics **13**(7-8): 731-739.
- Bauer, C. G., A. V. Eremenko, et al. (1996). "Zeptomole-detecting biosensor for alkaline phosphatase in an electrochemical immunoassay for 2,4-dichlorophenoxyacetic acid." Analytical Chemistry **68**(15): 2453-2458.
- Berg, M. C., S. Y. Yang, et al. (2004). "Controlling mammalian cell interactions on patterned polyelectrolyte multilayer surfaces." Langmuir **20**(4): 1362-1368.
- Boas, U. and P. M. H. Heegaard (2004). "Dendrimers in drug research." Chemical Society Reviews **33**(1): 43-63.
- Boxer, S. G. (2000). "Molecular transport and organization in supported lipid membranes." Current Opinion in Chemical Biology **4**(6): 704-709.
- Bruening, M. L., J. J. Harris, et al. (2001). "Ultrathin nanofiltration membranes prepared by layer-by-layer deposition of polyelectrolytes on porous supports." Abstracts of Papers of the American Chemical Society **222**: U388-U388.
- Burdette, D. S. and J. G. Zeikus (1994). "Purification of acetaldehyde dehydrogenase and alcohol dehydrogenases from *Thermoanaerobacter ethanolicus* 39E and characterization of the secondary-alcohol dehydrogenase (2 degrees Adh) as a bifunctional alcohol dehydrogenase--acetyl-CoA reductive thioesterase." Biochemical Journal **302**: 163-170.
- Burestedt, E., A. Narvaez, et al. (1996). "Rate-Limiting Steps of Tyrosinase-Modified Electrodes for the Detection of Catechol." Analytical Chemistry **68**(9): 1605-1611.

- Cassier, T., A. Sinner, et al. (1999). "Homogeneity, electrical resistivity and lateral diffusion of lipid bilayers coupled to polyelectrolyte multilayers." Colloids and Biointerfaces **15**: 215-225.
- Coche-Guerente, L., P. Labbe, et al. (1999). "Amplification of amperometric biosensor responses by electrochemical substrate recycling Part I. Theoretical treatment of the catechol-polyphenol oxidase system " Journal of Electroanalytical Chemistry **470**: 53-60.
- Coche-Guerente, L., P. Labbe, et al. (2001). "Amplification of amperometric biosensor responses by electrochemical substrate recycling. 3. Theoretical and experimental study of the phenol-polyphenol oxidase system immobilized in Laponite hydrogels and layer-by-layer self-assembled structures." Analytical Chemistry **73**(14): 3206-3218.
- Cornell, B. A., G. Krishna, et al. (2001). "Tethered-bilayer lipid membranes as a support for membrane-active peptides." Biochemical Society Transactions **29**: 613-617.
- Dai, J. H., A. M. Balachandra, et al. (2002). "Controlling ion transport through multilayer polyelectrolyte membranes by derivatization with photolabile functional groups." Macromolecules **35**(8): 3164-3170.
- Dai, J. H., A. W. Jensen, et al. (2001). "Controlling the permeability of multilayered polyelectrolyte films through derivatization, cross-linking, and hydrolysis." Langmuir **17**(3): 931-937.
- Dall'Orto, V. C., C. Danilowicz, et al. (1999). "Comparison between three amperometric sensors for phenol determination in olive oil samples." Analytical Letters **32**(10): 1981-1990.
- Darvesh, S., D. A. Hopkins, et al. (2003). "Neurobiology of butyrylcholinesterase." Nature Reviews Neuroscience **4**(2): 131-138.
- Davis, L., J. J. Britten, et al. (1997). "Cholinesterase - Its significance in anaesthetic practice." Anaesthesia **52**(3): 244-260.
- Decher, G. (1997). "Fuzzy nanoassemblies: Toward layered polymeric multicomposites." Science **5330**: 1232-1237.

- Decher, G. and J. D. Hong (1991). "Buildup of ultrathin multilayer films by a self-assembly process.2. consecutive adsorption of anionic and cationic bipolar amphiphiles and polyelectrolytes on charged surfaces." Berichte Der Bunsen-Gesellschaft-Physical Chemistry Chemical Physics **95**: 1430-1434.
- Desprez, V. and P. Labbe (1996). "A kinetic model for the electroenzymatic processes involved in polyphenol-oxidase-based amperometric catechol sensors." Journal of Electroanalytical Chemistry **415**(1-2): 191-195.
- DiazGarcia, M. E. and M. J. ValenciaGonzalez (1995). "Enzyme catalysis in organic solvents: A promising field for optical biosensing." Talanta **42**(11): 1763-1773.
- Ducey, M. W. and M. E. Meyerhoff (1998). "Microporous Gold Electrodes as Combined Biosensor/Electrochemical Detectors in Flowing Streams." Electroanalysis **10**(3): 157-162.
- Dvornic, P. R. and M. J. Owen (2002). ACS symposium series 838, American Chemical Society: 236-259.
- Dvornic, P. R. and D. A. Tomalia (1996). "Recent advances in dendritic polymers " Current Opinion in Colloid and Interface Science **1**: 221-235.
- Dzyadevych, S. V., A. P. Soldatkin, et al. (2002). "Assessment of the toxicity of methyl parathion and its photodegradation products in water samples using conductometric enzyme biosensors." Analytica Chimica Acta **459**(1): 33-41.
- Favero, G., A. D'Annibale, et al. (2002). "Membrane supported bilayer lipid membranes array: preparation, stability and ion-channel insertion." Analytica Chimica Acta **460**(1): 23-34.
- Feldman, K., G. Hahner, et al. (1999). "Probing resistance to protein adsorption of oligo(ethylene glycol)-terminated self-assembled monolayers by scanning force microscopy." Journal of the American Chemical Society **121**(43): 10134-10141.
- Flueraru, C., S. Schrader, et al. (2000). MCLC S&T, Section B: Nonlinear Optics **25**(1-4): 247-252.
- Fodor, S. P. A., J. L. Read, et al. (1991). "Light-Directed, Spatially Addressable Parallel Chemical Synthesis." Science **251**(4995): 767-773.

- Forshaw, P. J., J. Atkins, et al. (2001). "The catalytic domain of human neuropathy target esterase mediates an organophosphate-sensitive ionic conductance across liposome membranes." Journal of Neurochemistry **79**(2): 400-406.
- Forzani, E. S., V. M. Solis, et al. (2000). "Electrochemical behavior of polyphenol oxidase immobilized in self-assembled structures layer by layer with cationic polyallylamine." Analytical Chemistry **72**(21): 5300-5307.
- Forzani, E. S., M. L. Teijelo, et al. (2003). "Effect of the polycation nature on the structure of layer-by-layer electrostatically self-assembled multilayers of polyphenol oxidase." Biomacromolecules **4**(4): 869-879.
- Fou, A. C. and M. F. Rubner (1995). "Molecular-level processing of conjugated polymers. 2. layer-by-layer manipulation of in-situ polymerized p-type doped conducting polymers " Macromolecules **28**: 7115-7120.
- Freire, R. S., N. Duran, et al. (2002). "Electrochemical biosensor-based devices for continuous phenols monitoring in environmental matrices." Journal of the Brazilian Chemical Society **13**(4): 456-462.
- Frens, G. (1973). "Controlled nucleation for regulation of particle-size in monodisperse gold suspensions " Nature-Physical Science **241**: 20-22.
- Gajraj, A. and R. Y. Ofoli (2000). "Quantitative technique for investigating macromolecular adsorption and interactions at the liquid-liquid interface." Langmuir **16**(9): 4279-4285.
- Gerard, M., A. Chaubey, et al. (2002). "Application of conducting polymers to biosensors." Biosensors & Bioelectronics **17**(5): 345-359.
- Ghosh, S. and A. K. Banthia (2004). "Fluorophore-labeled polyamidoamine (PAMAM) dendritic architectures: Synthesis and fluorescence sensing properties." Supramolecular Chemistry **16**(7): 487-494.
- Glass, G. B. J. (1966). "Introduction - Gastric Proteins and Mucoproteins." American journal of digestive diseases **11**(2): 79-&.
- Glynn, P. (1999). "Neuropathy target esterase." Biochemical Journal **344**: 625-631.

- Gotschy, W., K. Vonmetz, et al. (1996). Applied Physics B: Lasers and Optics **B63(4)**: 381-384.
- Grabar, K. C., P. C. Smith, et al. (1996). "Kinetic control of interparticle spacing in Au colloid-based surfaces: Rational nanometer-scale architecture " Journal of the American Chemical Society **118**: 1148-1153.
- Graneli, A., J. Rydstrom, et al. (2003). "Formation of supported lipid bilayer membranes on SiO₂ from proteoliposomes containing transmembrane proteins." Langmuir **19(3)**: 842-850.
- Groves, J. T. and S. G. Boxer (2002). "Micropattern formation in supported lipid membranes." Accounts of Chemical Research **35(3)**: 149-157.
- Groves, J. T., S. G. Boxer, et al. (1998). "Electric field-induced critical demixing in lipid bilayer membranes." Proceedings of the National Academy of Sciences of the United States of America **95(3)**: 935-938.
- Groves, J. T., N. Ulman, et al. (1997). "Micropatterning fluid lipid bilayers on solid supports." Science **275(5300)**: 651-653.
- Guan, F., M. A. Chen, et al. (2005). "Fabrication of patterned gold microstructure by selective electroless plating." Applied Surface Science **240(1-4)**: 24-27.
- Harris, J. M. (1992). Poly(ethylene glycol) chemistry : biotechnical and biomedical applications. New York, Plenum Press.
- Herz, F. and E. Kaplan (1973). "Review - Human Erythrocyte Acetylcholinesterase." Pediatric research **7(4)**: 204-214.
- Heysel, S., H. Vogel, et al. (1995). "Covalent Attachment of Functionalized Lipid Bilayers to Planar Wave-Guides for Measuring Protein-Binding to Biomimetic Membranes." Protein Science **4(12)**: 2532-2544.
- Hovis, J. S. and S. G. Boxer (2000). "Patterning barriers to lateral diffusion in supported lipid bilayer membranes by blotting and stamping." Langmuir **16(3)**: 894-897.

- Hsieh, B. H., J. F. Deng, et al. (2001). "Acetylcholinesterase inhibition and the extrapyramidal syndrome: A review of the neurotoxicity of organophosphate." Neurotoxicology **22**(4): 423-427.
- Jiang, X. and P. T. Hammond (2000). "Selective deposition in layer-by-layer assembly: Functional graft copolymers as molecular templates " Langmuir **16**: 8501-8509.
- Jiang, X., H. Zheng, et al. (2002). "Polymer-on-polymer stamping: Universal approaches to chemically patterned surfaces " Langmuir **18**: 2607-2615.
- Johnson, J. M., T. Ha, et al. (2002). "Early steps of supported bilayer formation probed by single vesicle fluorescence assays." Biophysical Journal **83**(6): 3371-3379.
- Kalb, E., S. Frey, et al. (1992). "Formation of Supported Planar Bilayers by Fusion of Vesicles to Supported Phospholipid Monolayers." Biochimica Et Biophysica Acta **1103**(2): 307-316.
- Kam, L. and S. G. Boxer (2001). "Cell adhesion to protein-micropatterned-supported lipid bilayer membranes." Journal of Biomedical Materials Research **55**(4): 487-495.
- Karam, J. and J. A. Nicell (1997). "Potential applications of enzymes in waste treatment." Journal of Chemical Technology and Biotechnology **69**(2): 141-153.
- Karlsson, R. and A. Falt (1997). "Experimental design for kinetic analysis of protein-protein interactions with surface plasmon resonance biosensors." Journal of Immunological Methods **200**(1-2): 121-133.
- Kayyali, U. S., T. B. Moore, et al. (1991). "Neurotoxic Esterase (Nte) Assay - Optimized Conditions Based on Detergent-Induced Shifts in the Phenol/4-Aminoantipyrine Chromophore Spectrum." Journal of Analytical Toxicology **15**(2): 86-89.
- Keller, C. A. and B. Kasemo (1998). "Surface specific kinetics of lipid vesicle adsorption measured with a quartz crystal microbalance." Biophysical Journal **75**(3): 1397-1402.
- Kidambi, S., C. Chan, et al. (2004). "Selective depositions on polyelectrolyte multilayers: Self-assembled monolayers of m-dPEG acid as molecular template " Journal of the American Chemical Society **126**: 4697-4703.

- Kim, E. and Y. W. Xia, G. M. (1995). "Polymer microstructures formed by molding in capillaries." Nature **376**: 6541.
- Kim , Y. D., C. B. Park, et al. (2001). "Stable sol-gel microstructured and microfluidic networks for protein patterning." Biotechnology and Bioengineering **73(5)**: 331.
- Kohli, N., P. Dvornic, et al. (2004). "Nanostructured Cross-linkable Micropatterns via Amphiphilic Dendrimer Stamping." Macromolecular Rapid Communications **25(9)**: 935-941.
- Kohli, N., P. R. Dvornic, et al. (2004). "Nanostructured crosslinkable micropatterns by amphiphilic dendrimer stamping." Macromolecular Rapid Communications **25(9)**: 935-941.
- Kohli, N., B. L. Hassler, et al. (2006). "Tethered lipid bilayers on electrolessly deposited gold for bioelectronic applications." Biomacromolecules **7**: 3327-3335.
- Kohli, N., S. Vaidya, et al. (2006). "Arrays of lipid bilayers and liposomes on patterned polyelectrolyte templates." Journal of Colloid and Interface Science **301**: 461-469.
- Kohli, N., R. M. Worden, et al. (2005). "Intact transfer of layered, bionanocomposite arrays by microcontact printing." Chem. Commun. **3**: 316-318.
- Kreuzer, H. J., R. L. C. Wang, et al. (2003). "Hydroxide ion adsorption on self-assembled monolayers " Journal of the American Chemical Society **125(27)**: 8384-8389.
- Krishna, G., J. Schulte, et al. (2001). "Tethered bilayer membranes containing ionic reservoirs: The interfacial capacitance." Langmuir **17(16)**: 4858-4866.
- Kropp, T. J., P. Glynn, et al. (2004). "The mipafox-inhibited catalytic domain of human neuropathy target esterase ages by reversible proton loss." Biochemistry **43(12)**: 3716-3722.
- Krysinski, P., A. Zebrowska, et al. (2001). "Tethered mono- and bilayer lipid membranes on Au and Hg." Langmuir **17(13)**: 3852-3857.
- Kugler, R. and W. Knoll (2002). "Polyelectrolyte-supported lipid membranes." Bioelectrochemistry **56(1-2)**: 175-178.

- Kulkarni, P., M. Karve, et al. (1998). "Metalloenzyme biosensors: Part 1 - Amperometric tyrosinase biosensor for phenols using composite biopolymer matrix." Indian Journal of Chemistry I 37(1): 7-10.
- Kumar, A., H. A. Biebuyck, et al. (1994). "Patterning self-assembled monolayers- Applications in materials science." Langmuir 10: 1498-1511.
- Kumar, A. and G. M. Whitesides (1993). "Patterning self-assembled monolayers-
- Kung, L. A., J. T. Groves, et al. (2000). "Printing via photolithography on micropartitioned fluid lipid membranes." Advanced Materials 12(10): 731-+.
- Kung, L. A., L. Kam, et al. (2000). "Patterning hybrid surfaces of proteins and supported lipid bilayers." Langmuir 16(17): 6773-6776.
- Lakowicz, J. R. (1983). Principles of fluorescence spectroscopy. New York, Plenum Press.
- Lee, I., P. T. Hammond, et al. (2003). "Selective electroless nickel plating of particle arrays on polyelectrolyte multilayers." Chemistry of Materials 15: 4583-4589.
- Lee, I., H. Zheng, et al. (2002). "Controlled cluster size in patterned particle arrays via directed adsorption on confined surfaces." Advanced Materials 14: 572-577.
- Lejus, C., Y. Blanloeil, et al. (1998). "Cholinesterases." Annales Francaises D Anesthesie et de Reanimation 17(9): 1122-1135.
- Li, Y., D. Dinsdale, et al. (2003). "Protein domains, catalytic activity, and subcellular distribution of neuropathy target esterase in mammalian cells." Journal of Biological Chemistry 278(10): 8820-8825.
- Luo, G. B., T. T. Liu, et al. (2001). "Investigation of polymer-cushioned phospholipid bilayers in the solid phase by atomic force microscopy." Langmuir 17(13): 4074-4080.
- Lvov, Y., K. Ariga, et al. (1995). "Assembly of multicomponent protein films by means of electrostatic layer-by-layer adsorption." Journal of the American Chemical Society 117: 6117-6123.

- Ma, C., M. P. Srinivasan, et al. (2003). "Supported lipid bilayers lifted from the substrate by layer-by-layer polyion cushions on self-assembled monolayers." Colloids and Surfaces B-Biointerfaces **28**(4): 319-329.
- MacBeath, G. and S. L. Schreiber (2000). "Printing proteins as microarrays for high-throughput function determination " Science **289**: 1760.
- Makhaeva, G. F., L. V. Sigolaeva, et al. (2003). "Biosensor detection of neuropathy target esterase in whole blood as a biomarker of exposure to neuropathic organophosphorus compounds." Journal of Toxicology and Environmental Health-Part A **66**(7): 599-610.
- Marsh, D., L. I. Horvath, et al. (2002). "Interaction of membrane-spanning proteins with peripheral and lipid-anchored membrane proteins: perspectives from protein-lipid interactions (Review)." Molecular Membrane Biology **19**(4): 247-255.
- Michel, R., J. W. Lussi, et al. (2002). "Selective molecular assembly patterning: A new approach to micro- and nanochemical patterning of surfaces for biological applications " Langmuir **18**(8): 3281-3287.
- Millard, C. B. and C. A. Broomfield (1995). "Anticholinesterases - Medical Applications of Neurochemical Principles." Journal of Neurochemistry **64**(5): 1909-1918.
- Miller, M. D. and M. L. Bruening (2004). "Controlling the nanofiltration properties of multilayer polyelectrolyte membranes through variation of film composition." Langmuir **20**(26): 11545-11551.
- Moncelli, M. R., L. Becucci, et al. (2004). "Tethered bilayer lipid membranes self-assembled on mercury electrodes." Bioelectrochemistry **63**(1-2): 161-167.
- Moya, S., W. Richter, et al. (2003). "Freeze-fracture electron microscopy of lipid membranes on colloidal polyelectrolyte multilayer coated supports." Biomacromolecules **4**: 808-814.
- Munro, J. C. and C. W. Frank (2004). "Adsorption of lipid-functionalized poly(ethylene glycol) to gold surfaces as a cushion for polymer-supported lipid bilayers." Langmuir **20**(8): 3339-3349.

- Muramatsu, H., J. M. Dicks, et al. (1987). "Piezoelectric Crystal Biosensor Modified with Protein-a for Determination of Immunoglobulins." Analytical Chemistry **59**(23): 2760-2763.
- Naumann, C. A., O. Prucker, et al. (2002). "The polymer-supported phospholipid bilayer: Tethering as a new approach to substrate-membrane stabilization." Biomacromolecules **3**(1): 27-35.
- Naumann, R., S. M. Schiller, et al. (2003). "Tethered lipid Bilayers on ultraflat gold surfaces." Langmuir **19**(13): 5435-5443.
- Naumann, R., E. K. Schmidt, et al. (1999). "The peptide-tethered lipid membrane as a biomimetic system to incorporate cytochrome c oxidase in a functionally active form." Biosensors & Bioelectronics **14**(7): 651-662.
- Naumann, R., D. Walz, et al. (2003). "Kinetics of valinomycin-mediated K⁺ ion transport through tethered bilayer lipid membranes." Journal of Electroanalytical Chemistry **550**: 241-252.
- Nikolelis, D. P., T. Hianik, et al. (1999). "Biosensors based on thin lipid films and liposomes." Electroanalysis **11**(1): 7-15.
- Nollert, P., H. Kiefer, et al. (1995). "Lipid Vesicle Adsorption Versus Formation of Planar Bilayers on Solid-Surfaces." Biophysical Journal **69**(4): 1447-1455.
- Ohlsson, P. A., T. Tjarnhage, et al. (1995). "Liposome and Proteoliposome Fusion onto Solid Substrates, Studied Using Atomic-Force Microscopy, Quartz-Crystal Microbalance and Surface-Plasmon Resonance - Biological-Activities of Incorporated Components." Bioelectrochemistry and Bioenergetics **38**(1): 137-148.
- Park, J. and P. T. Hammond (2004). "Multilayer transfer printing for polyelectrolyte multilayer patterning: Direct transfer of layer-by-layer assembled micropatterned thin films " Advanced Materials **16**: 520-524.
- Perez-Salas, U. A., K. M. Faucher, et al. (2003). "Characterization of a biomimetic polymeric lipid bilayer by phase sensitive neutron reflectometry." Langmuir **19**(19): 7688-7694.

- Plant, A. L. (1999). "Supported hybrid bilayer membranes as rugged cell membrane mimics." Langmuir **15**(15): 5128-5135.
- Prodromidis, M. I. and M. I. Karayannis (2002). "Enzyme based amperometric Biosensors for food analysis." Electroanalysis **14**(4): 241-261.
- Proux-Delrouyre, V., C. Elie, et al. (2002). "Formation of tethered and streptavidin-supported lipid bilayers on a microporous electrode for the reconstitution of membranes of large surface area." Langmuir **18**(8): 3263-3272.
- Raguse, B., V. Braach-Maksvytis, et al. (1998). "Tethered lipid bilayer membranes: Formation and ionic reservoir characterization." Langmuir **14**(3): 648-659.
- Rainier, S., M. Bui, et al. Neuropathy target esterase gene mutations cause motor neuron disease, American Society of Human Genetics, Annual Meeting, Salt lake city, Utah, 2005
- Rajesh, W. Takashima, et al. (2004). "Amperometric phenol biosensor based on covalent immobilization of tyrosinase onto an electrochemically prepared novel copolymer poly (N-3-aminopropyl pyrrole-co-pyrrole) film." Sensors and Actuators B-Chemical **102**(2): 271-277.
- Ramanathan, K. and B. Danielsson (2001). "Principles and applications of thermal biosensors." Biosensors & Bioelectronics **16**(6): 417-423.
- Robeson, J. L. (1995). Application of total internal reflection fluorescence to probe surface diffusion and orientation of adsorbed proteins. Chemical Engineering. Pittsburgh, Carnegie Mellon University: 183.
- Ross, E. E., B. Bondurant, et al. (2001). "Formation of self-assembled, air-stable lipid bilayer membranes on solid supports." Langmuir **17**(8): 2305-2307.
- Saccani, J., S. Castano, et al. (2003). "A phospholipid bilayer supported under a polymerized Langmuir film." Biophysical Journal **85**(6): 3781-3787.
- Sackmann, E. (1996). "Supported membranes: Scientific and practical applications." Science **271**(5245): 43-48.

- Sackmann, E. and M. Tanaka (2000). "Supported membranes on soft polymer cushions: fabrication, characterization and applications." Trends in Biotechnology **18**(2): 58-64.
- Saini, S., G. F. Hall, et al. (1991). "Organic-Phase Enzyme Electrodes." Analytica Chimica Acta **249**(1): 1-15.
- Sanders, C. R. and K. Oxenoid (2000). "Customizing model membranes and samples for NMR spectroscopic studies of complex membrane proteins." Biochimica Et Biophysica Acta-Biomembranes **1508**(1-2): 129-145.
- Sigolaeva, L. V., A. Makower, et al. (2001). "Bioelectrochemical analysis of neuropathy target esterase activity in blood." Analytical Biochemistry **290**(1): 1-9.
- Sinner, E. K. and W. Knoll (2001). "Functional tethered membranes." Current Opinion in Chemical Biology **5**(6): 705-711.
- Sohling, U. and A. J. Schouten (1996). "Investigation of the adsorption of dioleoyl-L-alpha-phosphatidic acid mono- and bilayers from vesicle solution onto polyethylenimine-covered substrates." Langmuir **12**(16): 3912-3919.
- Sokolovskaya, L. G., L. V. Sigolaeva, et al. (2005). "Improved electrochemical analysis of neuropathy target esterase activity by a tyrosinase carbon paste electrode modified by 1-methoxyphenazine methosulfate." Biotechnology Letters **27**: 1211-1218.
- Solna, R., S. Sapelnikova, et al. (2005). "Multienzyme electrochemical array sensor for determination of phenols and pesticides." Talanta **65**(2): 349-357.
- Solna, R. and P. Skladal (2005). "Amperometric flow-injection determination of phenolic compounds using a biosensor with immobilized laccase, peroxidase and tyrosinase." Electroanalysis **17**(23): 2137-2146.
- St. John, P. M. and H. G. Craighead (1996). "Microcontact printing and pattern transfer using trichlorosilanes on oxide substrates " Applied Physics Letters **68**: 1022-1024.
- Stanca, S. E., I. C. Popescu, et al. (2003). "Biosensors for phenol derivatives using biochemical signal amplification." Talanta **61**(4): 501-507.

- Stanton, B. W., J. J. Harris, et al. (2003). "Ultrathin, multilayered polyelectrolyte films as nanofiltration membranes." Langmuir **19**(17): 7038-7042.
- Starr, T. E. and N. L. Thompson (2002). "Fluorescence pattern photobleaching recovery for samples with multi-component diffusion." Biophysical Chemistry **97**(1): 29-44.
- Stelzle, M., G. Weissmuller, et al. (1993). "On the Application of Supported Bilayers as Receptive Layers for Biosensors with Electrical Detection." Journal of Physical Chemistry **97**(12): 2974-2981.
- Stora, T., J. H. Lakey, et al. (1999). "Ion-channel gating in transmembrane receptor proteins: Functional activity in tethered lipid membranes." Angewandte Chemie-International Edition **38**(3): 389-392.
- Supriya, L. and R. O. Claus (2004). "Solution-based assembly of conductive gold film on flexible polymer substrates." Langmuir **20**(20): 8870-8876.
- Tavare, J. M., L. M. Fletcher, et al. (2001). "Review - Using green fluorescent protein to study intracellular signalling." Journal of Endocrinology **170**(2): 297-306.
- Terrettaz, S., M. Mayer, et al. (2003). "Highly electrically insulating tethered lipid bilayers for probing the function of ion channel proteins." Langmuir **19**(14): 5567-5569.
- Thompson, C. M. and R. J. Richardson (2004). Anticholinesterase Insecticides. Pesticide Toxicology and International Regulation. T. C. Marrs and B. Ballantyne. Chichester, John Wiley & Sons Limited: 89-127.
- Tien, H. T., R. H. Barish, et al. (1998). "Supported bilayer lipid membranes as ion and molecular probes." Analytical Sciences **14**(1): 3-18.
- Tien, H. T. and A. L. Ottova (1998). "Supported planar lipid bilayers (s-BLMs) as electrochemical biosensors." Electrochimica Acta **43**(23): 3587-3610.
- Tien, H. T. and A. L. Ottova (2000). Membrane Biophysics as viewed from experimental bilayer lipid membranes. Amsterdam; New York, Elsevier.

- Tomalia, D. A. and P. R. Dvornic (1996). In Polymeric Materials Encyclopedia, Salamone, J.C., Ed., CRC Press:Boca Raton 3: 1814-1830.
- Tomalia, D. A., A. M. Naylor, et al. (1990). "Starbust dendrimers-Molecular level control of size, shape, surface-chemistry, topology, and flexibility from atoms to macroscopic matter." Angewandte Chemie-International Edition 102: 119-157.
- Townshend, A. (1995). Encyclopedia of Analytical Science. London, Academic Press.
- Tristram-Nagle, S., H. I. Petrache, et al. (1998). "Effect of substrate roughness on D spacing supports theoretical resolution of vapor pressure paradox." Biophysical Journal 74(2): A203-A203.
- Trojanowicz, M. (2001). "Miniaturized biochemical sensing devices based on planar bilayer lipid membranes." Fresenius Journal of Analytical Chemistry 371(2): 246-260.
- Uchiyama, S., Y. Hasebe, et al. (1993). "Enzyme-Based Catechol Sensor Based on the Cyclic Reaction between Catechol and 1,2-Benzoquinone, Using L-Ascorbate and Tyrosinase." Analytica Chimica Acta 276(2): 341-345.
- van Tienhoven, M., J. Atkins, et al. (2002). "Human neuropathy target esterase catalyzes hydrolysis of membrane lipids." Journal of Biological Chemistry 277(23): 20942-20948.
- VandenDriessche, T. (2005). "Gene therapy flexes muscle - A European Society of Gene Therapy commentary on progress in gene therapy for Duchenne muscular dystrophy and amyotrophic lateral sclerosis." Journal of Gene Medicine 7(9): 1255-1256.
- Vinson, V. J. (2006). "Proteins at work - Introduction." Science 312(5771): 211-211.
- Vo-Dinh, T. and B. Cullum (2000). "Biosensors and biochips: advances in biological and medical diagnostics." Fresenius Journal of Analytical Chemistry 366(6-7): 540-551.
- Vogel, A. I. (1998). Textbook of Quantitative Chemical Analysis. Essex, UK, Longman.

- Wagner, M. L. and L. K. Tamm (2000). "Tethered polymer-supported planar lipid bilayers for reconstitution of integral membrane proteins: Silane-polyethyleneglycol-lipid as a cushion and covalent linker." Biophysical Journal **79**(3): 1400-1414.
- Wang, J., J. M. Lu, et al. (2000). "Lab-on-a-Cable for electrochemical monitoring of phenolic contaminants." Analytical Chemistry **72**(11): 2659-2663.
- Wiegand, G., N. Arribas-Layton, et al. (2002). "Electrical properties of supported lipid bilayer membranes." Journal of Physical Chemistry B **106**(16): 4245-4254.
- Willner, I. and E. Katz (2000). "Integration of layered redox proteins and conductive supports for bioelectronic applications." Angewandte Chemie-International Edition **39**(7): 1180-1218.
- Wright, L. L., A. G. Palmer, et al. (1988). "Inhomogeneous Translational Diffusion of Monoclonal-Antibodies on Phospholipid Langmuir-Blodgett Films." Biophysical Journal **54**(3): 463-470.
- Xia, Y., E. Kim, et al. (1996). "Microcontact printing of alkanethiols on copper and its application in microfabrication " Chem. Mater. **8**: 601-603.
- Yang, S. Y. and M. F. Rubner (2002). "Micropatterning of polymer thin films with pH-sensitive and cross-linkable hydrogen-bonded polyelectrolyte multilayers." Journal of the American Chemical Society **124**(10): 2100-2101.
- Yang, X. M., D. A. Tryk, et al. (1996). "Surface enhanced Raman imaging of a patterned self-assembled monolayer formed by microcontact printing on a silver film " Applied Physics Letters **69**: 4020-4022.
- Yin, P., C. J. Burns, et al. (2003). "A tethered bilayer sensor containing alamethicin channels and its detection of amiloride based inhibitors." Biosensors & Bioelectronics **18**(4): 389-397.
- Yoo, D., S. S. Shiratori, et al. (1998). "Controlling bilayer composition and surface wettability of sequentially adsorbed multilayers of weak polyelectrolytes." Macromolecules **31**(13): 4309-4318.

- Zebrowska, A., P. Krysinski, et al. (2002). "Electrochemical studies of blocking properties of solid supported tethered lipid membranes on gold." Bioelectrochemistry **56**(1-2): 179-184.
- Zhang, G. J., T. Tanii, et al. (2004). "Patterning of DNA nanostructures on silicon surface by electron beam lithography of self-assembled monolayer " Chemical Communications **7**: 786-787.
- Zhang, L., R. Vidu, et al. (2002). "Electrochemical and surface properties of solid-supported, mobile phospholipid bilayers on a polyion/alkylthiol layer pair used for detection of antimicrobial peptide insertion." Langmuir **18**(4): 1318-1331.
- Zhang, L. Q., C. A. Booth, et al. (2000). "Phosphatidylserine/cholesterol bilayers supported on a polycation/alkylthiol layer pair." Journal of Colloid and Interface Science **228**(1): 82-89.
- Zhang, L. Q., M. L. Longo, et al. (2000). "Mobile phospholipid bilayers on a polyion/alkylthiol layer pair." Langmuir **16**(11): 5093-5099.
- Zheng, H., I. Lee, et al. (2002). "Two component particle arrays on patterned polyelectrolyte multilayer templates " Advanced Materials **14**(8): 569-572.

MICHIGAN STATE UNIVERSITY LIBRARIES



3 1293 02845 9042